Spin polarized transport in magnetic layered structures : 1/f noise and tunnel junctions

Please check the document version of this publication:

• A submitted manuscript is the version of the article upon submission and before peer-review. There can be important differences between the submitted version and the official published version of record. People interested in the research are advised to contact the author for the final version of the publication, or visit the DOI to the publisher's website.
• The final author version and the galley proof are versions of the publication after peer review.
• The final published version features the final layout of the paper including the volume, issue and page numbers.

[Link to publication](#)

SPIN POLARIZED TRANSPORT IN

MAGNETIC LAYERED STRUCTURES

1/f noise and tunnel junctions

sense
current

R.J.M. VAN DE VEERDONK

Spin polarized transport in magnetic layered structures

1/f noise and tunnel junctions

PROEFSCHRIFT

door

René Johannes Marinus van de Veerdonk

geboren te Eindhoven

Dit proefschrift is goedgekeurd door de promotoren:

prof.dr.ir. W. J. M. de Jonge
en
prof.dr. R. Coehoorn

Contents

Chapter 1

General Introduction

By analogy with the developments in semiconductor physics, the considerable progress in metallic magnetic thin film deposition techniques of nanoscale magnetic layered structures has led to a number of fascinating discoveries both fundamentally and technologically appealing. This has fueled a booming and widespread interest in the magnetism and specifically the magneto-transport properties of these materials, as witnessed during the last decade. The triggering event was the unexpected discovery by Carcia et al. [1] of a perpendicular easy axis of magnetization in a stack of thin alternating non-magnetic Pt and magnetic Co layers. The next major breakthrough was the discovery in 1986 by Grünberg et al. [2] that the magnetic interaction between two thin ferromagnetic Fe films separated by a thin (thickness $t \sim 1$ nm) nonmagnetic Cr layer could be made to change from ferromagnetic to antiferromagnetic depending on the exact thickness of the nonmagnetic layer.

Shortly after the latter report, it was realized that exciting new magneto-transport phenomena were to be expected in multilayers of Fe and Cr, in which the Cr layer thickness was tuned such that the magnetic interaction was antiferromagnetic. Indeed, the Giant Magnetoresistance (GMR) effect was discovered two years later by Baibich et al. [3] and Binasch et al. [4] in this type of metallic magnetic multilayers. The effect was named 'Giant' after the order of magnitude larger magnetic field induced decrease of the electrical resistance for the multilayer (of the order of 100%) compared the largest Anisotropic Magnetoresistance (AMR) effect known for bulk ferromagnetic materials (of the order of a few percent). It was recognized early on that this newly discovered magnetoresistance effect had large application potential, and numerous companies and university research groups all over the world have been working in this field of research ever since. It is illustrative in this respect that, within 10 years after the GMR effect has been discovered, and driven by the never-ending quest for miniaturization to obtain and handle higher storage densities of information, commercial devices based on this new technology are available on the market (for example, high-end hard-disk read-heads, magnetic field sensors, and magnetic memory chips).

Although the discovery of the GMR effect in magnetic metallic multilayers can be considered as a triggering event in the recent history of magneto-transport studies, the

effect was neither the first nor the last magnetoresistive effect to be discovered. As early as 1857, Thomson (later Lord Kelvin) [5] discovered that the resistance of ferromagnetic metals depends on the orientation of the magnetization of the sample relative to the direction of the measuring current. This effect has been named the Anisotropic Magnetoresistance (AMR) effect and originates from the spin-orbit interaction, see Fig. 1.1(b). An excellent review of the experimental work and understanding of the AMR effect has been provided by McGuire and Potter [6], who also briefly discuss the ordinary magnetoresistance effect. The largest reported relative change in resistance at room temperature, caused by the AMR effect, for the series of *3d* transition metals and their alloys, is about 6.6% for the alloy $Ni_{70}Fe_{30}$ [6]. The magnetic field range in which the AMR effect occurs, is governed by the field needed to change the direction of the magnetic moment of the material. For some magnetic alloys, such as permalloy ($Ni_{80}Fe_{20}$), this field can be as small as 0.3–0.5 kA/m, i.e., only one order of magnitude larger than the earth magnetic field. The field range and the magnitude of the AMR effect have proven to be sufficient to be applied for magnetic recording purposes, where information is stored in a magnetic medium and is read-out by detecting the escaping magnetic flux. It should be noted that due to the weaker technological constraints and the robustness against, for instance, atomic diffusion processes at high temperatures, AMR materials may remain to be an interesting alternative to the more sensitive, but also less robust magnetoresistive materials discussed below.

Apart from the AMR effect in ferromagnetic metals, magnetoresistive effects of different origin have been reported for both bulk and thin film materials. The already mentioned ordinary magnetoresistance effect is relatively large in some semiconductor materials, and is applied in some commercial magnetic field sensors [7]. It originates from the effect of the Lorentz force due to the magnetic field on the electron trajectories in the sensor material, see Fig. 1.1(a).

A particularly interesting second example is the so-called 'colossal' magnetoresistance (CMR) effect in the family of doped manganate perovskites, for which the material $La_{1/3}Ca_{2/3}MnO_3$ is the prototypical example [8–11], and the close related pyrochlore $Tl_2Mn_2O_7$ [12–14]. The CMR effect can be very large, changes in the electrical resistance of several orders of magnitude are fairly common. The CMR effects is the result of a magnetic field driven metal-insulator transition at the magnetic ordering temperature of the manganate perovskite, which implies that the effect is only seen in the temperature range in the vicinity of the Curie temperature of these materials and always requires magnetic fields in the range of several Teslas. Due to these properties the applicability of these materials as such for sensitive magnetic field sensors is fairly limited.

The giant magnetoresistance arises for metallic devices in which magnetic and nonmagnetic materials are combined, as for instance in the Fe/Cr multilayers mentioned earlier. The resistance depends on the relative orientation of two or more magnetic entities, see Fig. 1.1(c). The magnetoresistance originates from the different scattering rates (the scattering rate is proportional to the resistivity) for majority and minority spin electrons, either in the bulk of a ferromagnetic layer or at the ferromagnet/normal metal interface. As an example, consider the electron transport through a trilayer containing two magnetic layers, separated by a nonmagnetic layer. In an extreme case, a majority
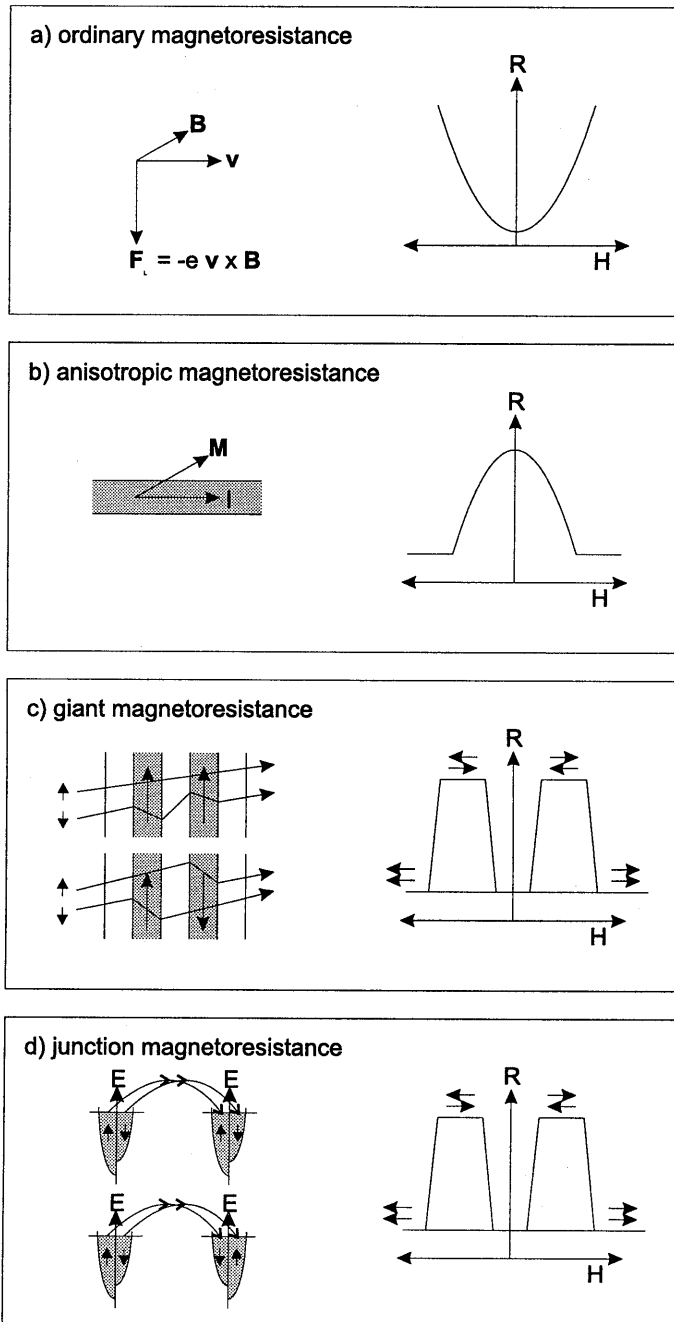
Figure 1.1: Schematic overview of several magnetoresistance mechanisms, see text for explanation.

spin electron traverses a magnetic layer without scattering (i.e., a low resistance), while a minority spin electron scatters many times (i.e., a high resistance). When both magnetic layers have their magnetizations aligned parallel, the majority spin electrons will traverse the whole system freely and the resistance of the whole system for the majority spin electrons is low. The minority spin electrons, however, undergo scattering events in both magnetic layers, and their total resistance is high. Consider next the situation in which the magnetization direction of one of the magnetic layers is reversed. The roles of majority and minority spin electrons in that layer are now also reversed. Electrons which are majority spin electrons in one layer, are minority spin electrons in the other layer. Electrons in both spin-channels will therefore undergo an equal (relatively high) rate of scattering. As a consequence, the resistance of the whole device will increase. This GMR effect is not limited to metallic magnetic multilayers alone. Any system in which separate magnetic entities exist and are able to change the relative orientation of the magnetic moments shows the effect. The only requirement is the distance between the magnetic entities, which should be within the mean-free-path of the conduction electrons.

Well before the discovery of the GMR effect, it was known that the tunneling current between two metallic magnetic layers separated by a very thin *insulating* barrier (called a magnetic tunnel junction, MTJ) depends on the relative orientation of the magnetization in the adjacent magnetic layers in much the same way as found for the GMR effect, see Fig. 1.1(d). This magneto-tunneling effect has been named junction magnetoresistance (JMR), sometimes also called tunnel magnetoresistance (TMR). Julliere performed pioneering experiments on such junctions already in the seventies [15]. Until recently, however, only a relatively modest number of studies were reported. Partly this was caused by the technologically demanding fabrication process, which makes it extremely difficult to realize robust and reliable junctions. Additionally, also the fact that the reported magnetic transport effects were small ($\Delta R/R$ at most a few percent) did not trigger considerable interest in view of alternative possibilities for sensor applications. Recently, however, a few groups [16–20], including our own, succeeded in preparing tunnel junctions with high magnetoresistance at room temperature and low magnetic switching fields. For device geometries which are considered for potential applications, the JMR effect in magnetic tunnel junctions is larger than the GMR in layered magnetic metals. This makes these junctions rather promising candidates for the use as magnetic sensors and non-volatile memory elements.

It should be stressed at this point that the JMR effect, which is due to ballistic (i.e., non-diffusive) spin-dependent transport, has to be distinguished from the giant magnetoresistance (GMR) effect in layered magnetic metals, where the spin-dependent scattering probability (i.e., diffusive transport) of the carriers is the major physical origin. One significant difference from a device point of view is the geometry. Where the JMR effect is an intrinsically perpendicular effect, in that the sense current must flow perpendicular to the film plane (so-called CPP-geometry), the GMR effect is usually applied with the sense current in the film plane (CIP-geometry).

1.1   This Thesis

In this thesis, a selection of the work performed over the past years is presented, covering several aspects of magneto-transport properties in different magnetic layered structures. The systems under study varied from single magnetic metallic layers to multilayers containing both metals and nonmetals, from homogeneous thin films to structured device geometries, using a range of materials, such as magnetic and nonmagnetic metals, insulators, conducting oxides, and superconductors. The thesis has been divided into two Parts, each focusing on a different magneto-transport phenomenon. Part I discusses the electronic noise of test structures of AMR and GMR based magnetoresistive elements optimized for use as magnetic field sensor in read-heads for, e.g., tape recording. In Part II the focus is on the transport properties of magnetic tunnel junctions, which is presently regarded as a possible long term successor of the devices studied in Part I.

In Part I, Chapter 2, electronic noise in magnetic devices is discussed, with the emphasis on noise with a magnetic origin. Most attention in previous research had been focussed on optimizing the magnetoresistance effect to obtain a more sensitive magnetic field sensor. Here, two of the proposed optimized devices geometries have been investigated for their electronic noise behavior. The first is a traditional device consisting of a single magnetic layer, where the magnetoresistance is caused by the AMR effect. The second is a metallic multilayer consisting of a pinned and a free (i.e., not pinned) soft-magnetic layer separated by a nonmagnetic metallic spacer layer. The magnetoresistance of the latter device is a superposition of the AMR effect found in the magnetic layers and the much larger GMR effect resulting from the relative magnetization reorientation in the trilayer structure. The noise has been measured in the low frequency range (1 Hz $\leq f \leq 100$ kHz) and can be separated in a frequency independent (also called white) contribution, which dominates at the higher frequencies, and a magnetic field dependent $1/f$ (also called pink) contribution, which dominates at low frequencies. A model is proposed to account for the variation of the $1/f$ contribution as a function of the applied magnetic field.

In Part II research on magnetic tunnel junctions is discussed. A wide range of topics has been covered. Chapter 3 gives an overview of the field. In the Chapter 4, various experimental results on a good FM-I-FM junction are presented, and the importance of the interface properties is established.

The next chapters focus each on a specific research topic. Chapter 5 discusses a model calculation on the well known problem of the interpretation of experimental results which arises when the value of the resistance of the device becomes comparable to the resistance of the connections to the measuring equipment. Chapter 6 discusses the temperature dependence of the junction magnetoresistance effect. It is found that the results can not be interpreted based on a so-called elastic tunnel conductance contribution alone, thermally or bias voltage activated additional conductance contributions need to be included. Two distinctly different models proposed in the literature are discussed and both are found to yield a good description of the experimental results. Inelastic conduction mechanisms in the tunnel junctions are studied using Inelastic Electron Tunneling Spectroscopy (IETS) measurements, which is the subject of Chapter 7. Chapter 8

presents results of transport measurements of a series of devices with the aim to study the influence of the duration of the oxygen glow discharge time, used for preparing the oxide barrier layers, on the magneto-transport properties. The effect of the development of quantum well states in layers of nonmagnetic metals added at the interface of the barrier layer is the subject of Chapter 9. And finally, in Chapter 10, results will be presented of direct measurements of the tunneling electron spin polarization, using the well established spin polarized tunneling technique. In the concluding Chapter 11, the results will be shortly reviewed and a personal view on future developments will be presented.

Regarding the structure of this thesis, the reader should be aware that several of the Chapters have been published in or submitted to the scientific literature, with or without minor changes. The advantage is that these Chapters can be read independently. On the other hand, some redundancy occured as a result of the inclusion of similar information in several Chapters.

Part I

1/*f* Noise in Magnetoresistive Elements

Chapter 2

1/f Noise in Anisotropic and Giant Magnetoresistive Elements

Abstract:*

Microfabricated magnetoresistive elements based on either the anisotropic or the giant magnetoresistance effect were tested for their frequency dependent resistance noise behavior at room temperature in a dc magnetic field, using a dc sense current. Thermal resistance noise was the dominant noise source above about 10 kHz. At low frequencies the resistance noise was found to be dominated by a 1/f contribution that depends on the applied magnetic field. The 1/f noise is relatively low and field independent when the element is in a saturated state and contains a relatively large and field dependent excess contribution when the magnetic field is in the sensitive field range of the element. The 1/f noise level observed in saturation is comparable to the 1/f noise level found in nonmagnetic metals; the excess noise has a magnetic origin. The variation of the excess noise level with the applied dc magnetic field can be explained qualitatively using a simple model based on thermal excitations of the magnetization direction.

2.1   Introduction

Magnetoresistive elements (MREs) are being applied in magnetic recording read-heads and in sensor applications including position, velocity, acceleration, and angle detectors. Presently, these devices are based on the anisotropic magnetoresistance (AMR) effect [6], which is the resistance change due to the rotation of the magnetization of a single magnetic layer with respect to the sense current. The relative resistance change in an applied magnetic field (the AMR-ratio $\Delta R_{max}/R_0$, where ΔR_{max} and R_0 are the maximum resistance change and the minimum resistance, respectively) is about 2% in magnetically soft permalloy ($Ni_{80}Fe_{20}$, for which below the notation Py is used) films, which are most commonly applied in high sensitivity sensors. Due to ongoing miniaturization there is a drive for more sensitive MREs, which are able to measure smaller magnetic fields or less flux (e.g. from a smaller bit on a magnetic information carrier). One of the options for improvement is the use of the giant magnetoresistance (GMR) effect [3, 4], which is the resistance change due to changing the relative orientation of the magnetization of at least two stacked magnetic layers. One of the most promising structures showing the GMR effect is the so-called spin-valve structure consisting of two magnetic layers (typically Py) separated by a nonmagnetic layer (typically Cu) [21]. One of the magnetic layers has a fixed magnetization direction due to exchange biasing with an adjacent antiferromagnetic layer (typically $Fe_{50}Mn_{50}$), while the other magnetic layer is free to rotate in a small applied magnetic field. The relative resistance change (GMR-ratio) of such a spin-valve structure can be several times larger than the AMR effect for the individual magnetic layers, whereas in unpatterned films the switching takes place within approximately the same magnetic field range [22].

To assess the applicability of GMR sensor elements the GMR-ratio and the switching field range are not the only relevant parameters. Equally important is the signal to noise ratio (see, e.g. Ref. [23]). One contribution to the sensor noise is thermal resistance noise (also called Johnson or Nyquist noise), which is always present in resistive devices and is caused by thermal smearing of the distribution function of electrons near the Fermi-level. This noise source contributes a constant background to the voltage spectral density in the frequency range considered equal to $S_V = 4kTR$ (in units of V^2/Hz), where k is the Boltzmann constant, T is the temperature, and R is the total resistance of the sensor.

A second noise source is Barkhausen noise, which arises from sudden and irreversible domain wall motion. This noise source can be suppressed by stabilizing a single magnetic domain state and by promoting a coherent rotation process of the magnetization during switching. This can be achieved by providing an easy axis of magnetization perpendicular to the applied magnetic field, by using a specific sensor design (such as the "picture frame" geometry) [24], or by applying a small stabilizing magnetic field (externally or from the applied sense current, such as in the "barber pole" geometry) [25].

This Chapter focusses on a third noise source, namely 1/f noise (also called flicker noise) [26–28]. This contribution to the sensor noise is a potential limiting factor for applications of MREs as low frequency magnetic field sensors, or when sensors are miniaturized to allow for higher spatial resolution. Recently, a number of studies have

been performed on the $1/f$ noise behavior of magnetic multilayers [29–35]. In these studies the amplitude of the $1/f$ noise was observed to be significantly enhanced with respect to nonmagnetic metals. This has been attributed to the complex domain structure in the studied magnetic multilayers. The lack of information on the micromagnetic structure prevented, however, a more detailed understanding.

We feel that single magnetic domain test structures in which the magnetization rotates coherently in an applied field are much better suited for the investigation of the relation between magnetism and $1/f$ noise. The magnetic state of these structures is well characterized and can be modified in a controlled way. This provides an additional knob that is accessable experimentally and that allows to change parameters reproducibly and continuously using a single device. This is in contrast to nonmagnetic materials where only the temperature can be varied.

In this Chapter we present a comparative study of $1/f$ noise in AMR-based and GMR-based MREs. The investigated GMR-based MREs are exchange biased spin-valve structures, containing only a single magnetically sensitive layer. These elements are microfabricated in the "picture frame" geometry, which makes it possible to prepare a magnetic structure such that it is essentially in a single magnetic domain state [36]. It has been shown that the switching of the free layer occurs as a coherent magnetization rotation process, although the edges of the elements saturate in higher magnetic fields than the center [37].

We find that also for these single domain structures there is a strong, magnetic field dependent contribution to the $1/f$ noise in the sensitive field range. The results are interpreted in terms of thermal excitations of the magnetization direction and explained qualitatively using a simple model based on a Stoner–Wohlfart description of the total energy.

2.2 Experiment

The MREs used in this study are deposited on nonmagnetic polycrystalline ceramic substrates (an Al–TiC mixture called "Alsimag"). A layer of 30 nm Py is used for the AMR-based MRE. The GMR-based MRE consists of the multilayer 8 nm Py/2.8 nm Cu/6 nm Py/10 nm $Fe_{50}Mn_{50}$. Both MREs are grown on a buffer layer of 3.5 nm Ta and have a capping layer of 10 nm Ta. Deposition was performed by dc magnetron sputtering in a multitarget ultrahigh vacuum (UHV)-sputtering apparatus in a magnetic field in order to induce uniaxial magnetocrystalline anisotropy. The magnetic field H_I of $\sim$15 kA/m is applied along the direction that after patterning is parallel to the long axis of the element (longitudinal direction). After deposition the films are microfabricated in a picture frame geometry using optical lithography and Ar ion milling [36] (see Fig. 2.1). In this geometry the magnetic layers form an almost closed yoke in order to essentially eliminate domain wall formation in the sensitive part (active area) of the MRE.

A 100-nm-thick gold metallization layer is used to make low resistive connections to the active area of the microfabricated (multi)-layer. The active area is 10-μm-wide and varies in length l between 10 and 70 μm. The metallization layer connects on both

sides to a single contact pad, which is used as both voltage and current lead. This adds a contact resistance from the metallization connections to the resistance of the active area of the MRE. The metallization connections also contribute to the noise by increasing the thermal noise and adding 1/f contact noise. Despite these disadvantages the two terminal geometry has been chosen over a four terminal geometry in order to resemble more closely the designs used for read-head applications. The influence of the geometry on the experimental results was verified, see below, and was found to be minor and easily distinguishable. AMR-based MREs have been fabricated both with [Fig. 2.1(a)] and without [Fig. 2.1(b)] a slanted pattern of 100-nm-thick gold stripes, a so-called barber pole metallization [25], on top of the active part of the MRE. The barber pole metallization is commonly used to linearize the response around zero applied magnetic field and will be discussed in more detail below. The AMR-based MREs without barber pole have been microfabricated with varying length of the active area on a single substrate, which makes it possible to determine the contact resistance (noise).

After processing, the GMR-based MREs were heated to 140 °C and subsequently cooled in an applied magnetic field H_t along the short axis of the MRE (the transverse direction). This procedure rotates the exchange biasing direction of the top (or "pinned") magnetic layer [36]. The growth induced uniaxial magnetocrystalline anisotropy promotes hysteresis free rotation of the other ("free") magnetic layer in an applied transverse magnetic field [22].

The measurements have been performed in mumetal shielded boxes using the setup as shown in Fig. 2.2. A static magnetic field $H = (H_l, H_t)$ can be applied in the film plane using two orthogonal sets of Helmholtz coils with a maximum field strength of about 4 kA/m each. The current for these coils is generated by mains powered supplies (Kepco BOP36-12). The sense current I_s through the MRE is provided by a battery unit and can be varied by changing the series resistor R_s. The voltage is measured by two pairs of voltage leads and is preamplified by two battery powered ultra low-noise ac voltage amplifiers with a gain of 1000 (EG&G Brookdeal 5004) before they are transferred to the analyzer. The analyzer [HP3562A dynamic signal analyser (DSA)] was used in cross-correlation mode to minimize the spurious noise contributions of the voltage lead connections and the preamplifiers. The voltage spectral density $S_V(f, H)$ has been measured for frequencies f between 10 Hz and 100 kHz. The relative error in the presented noise levels is within ±10%.

2.3   Experimental results

An example of a spectrum for a GMR-based MRE is given in Fig. 2.3(a). In Fig. 2.3(a) the 1/f contribution to the spectrum is apparent in the low frequency range while at higher frequencies the noise is dominated by thermal noise (in the example the crossover frequency is ∼8 kHz). The thermal noise level was never observed to deviate significantly from the expected $4kTR$ level. The results presented below will focus on the amplitude of the 1/f component in the spectra.

The voltage spectral density for 1/f noise can be described phenomenologically by the Hooge relation [38]:
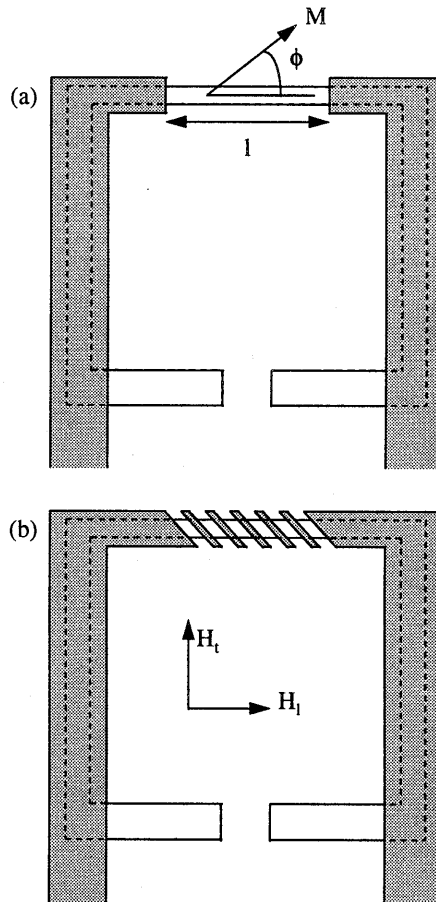
Figure 2.1: Schematic representation of the geometries used for (a) the AMR-based and GMR-based MREs and (b) the AMR-based MREs with additional barber pole metallization. The $170 \times 150 \ \mu m^2$ magnetic yoke form (not shaded, also called picture frame) consists of a single magnetic layer for the AMR-based MREs and of a multilayer for the GMR-based MREs. The active area of the element is determined by the distance l between the two outermost metallization contacts (shaded). ϕ is the angle between the magnetization M and the long axis of the element. The magnetic fields H_t and H_l can be applied in the transverse and longitudinal direction with respect to the long axis of the element, respectively. The AMR-based MRE with barber pole (b) has slanted 4-μm-wide metallization stripes, spaced 7.5 μm apart (measured in the long axis direction) and at an angle of 45° with the long axis.
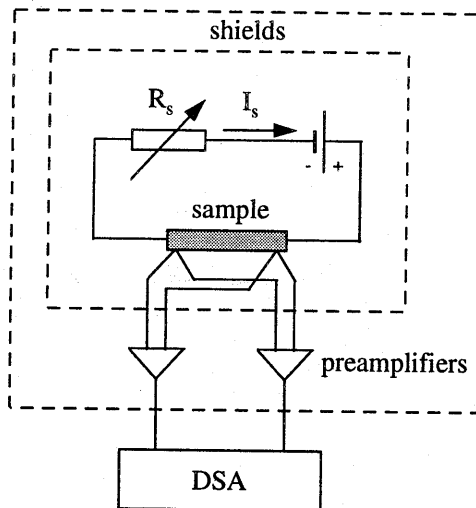
Figure 2.2: Experimental setup as used for the noise measurements; all sensitive parts are placed in two mumetal shielded boxes. After preamplification, two independent signals are fed to the DSA. The Helmholtz coils (not shown) used to generate the magnetic fields are located inside the inner box.
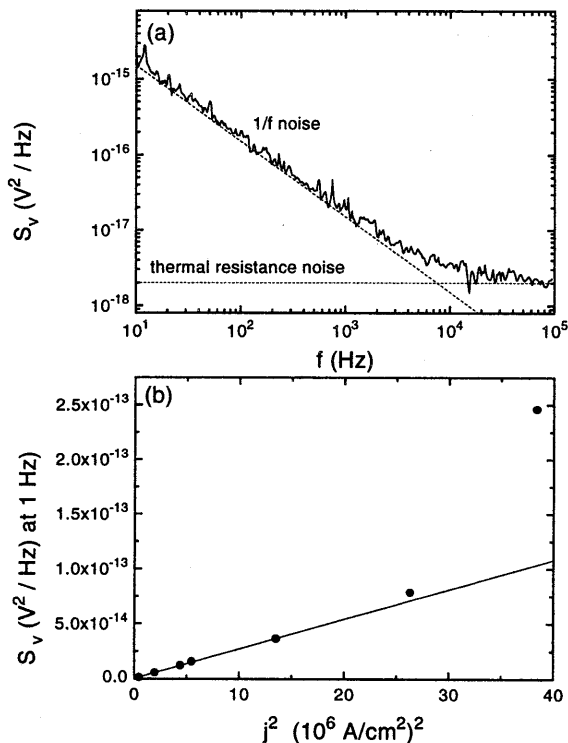
Figure 2.3: (a) Example of a voltage spectral density spectrum for a GMR-based MRE with an active area length $l = 70$ μm in an applied transverse magnetic field $H_t = 0.50$ kA/m and for a dc sense current $I_s = 2.36$ mA, corresponding to a film averaged sense current density $j = 1.4 \times 10^{10}$ A/m^2. Thermal noise and $1/f$ noise contributions are indicated by dashed lines. (b) The voltage spectral density extrapolated to 1 Hz vs the square of the applied film averaged sense current density without applied magnetic fields follows a j^2 behavior (solid line) upto a current density $j_c \approx 5 \times 10^{10}$ A/m^2.

$$S_V(f,\ \boldsymbol{H}) = \frac{\alpha(\boldsymbol{H})}{Nf^\gamma} V_{\text{dc}}^2, \qquad\qquad (2.1)$$

where the exponent γ is of order one and the total number of conduction electrons in the sample N is taken equal to the number of atoms in the active area of the MRE. The dimensionless normalizing constant α is called the Hooge constant which for magnetic materials depends on the magnetic state which in turn depends on the applied magnetic field. The exponent γ was also found to have a significant dependence on the applied magnetic field, which we will not discuss in this article, and ranged between 0.85 and 1.20. We will use the voltage spectral density extrapolated to 1 Hz as a measure for the $1/f$ noise. Since S_V depends on the volume and resistance of the MRE as well as the

applied sense current, only α values can be used to compare the intrinsic 1/f noise levels between different MREs. The buffer and cap layers are disregarded in the analysis of noise data because of the high resistivity of Ta.

According to the Hooge relation Eq. (2.1), S_V should be proportional to I_s^2 for constant applied magnetic field. In Fig. 2.3(b) the voltage spectral density at 1 Hz is shown to increase linearly with the square of the applied dc sense current density upto a critical film averaged current density $j_c \approx 5 \times 10^{10}$ A/m^2. For higher current densities the 1/f noise is higher than expected from the Hooge relation Eq. (2.1). All experiments reported in this article have been conducted at current densities below j_c. For comparison, in our laboratory a sense current of 10 mA is the standard operating condition for all MREs. This corresponds to a current density of 6×10^{10} A/m^2) in Fig. 2.3(b) which is slightly above j_c.

The volume scaling predicted by the Hooge relation Eq. (2.1) has to be used with caution for a magnetic element due to the influence of the geometry on its magnetic properties. When the magnetic properties are changed (e.g., by varying the thickness or the width of the stripe) this will have an additional effect on the noise, mainly via the α parameter. Only the length of the active area can be varied without changing the magnetic properties. This can be done by changing the layout of the nonmagnetic metallization layer. We will use this below to estimate the contact noise contribution.

We note that for metallic thin film elements the analysis of the 1/f noise in terms of the Hooge relation Eq. (2.1) is principle incorrect due to the nonuniform current density across the film thickness. First, this is due to the effect of the film boundaries (see, e.g., Refs. [39] and [40]). In multilayers an additional nonuniformity is caused by the different resistivities for the various materials and the scattering of electrons at the interfaces between them. Nevertheless, we will use Eq. (2.1) below as a first step towards a more complete analysis of the experimental results because we are dealing with systems for which the values of α are different by more than one order of magnitude.

2.3.1   AMR-based MRE without barber pole

The first system studied is an AMR-based MRE consisting of a 30-nm-thick Py thin film without barber pole metallization. The geometry is a narrow magnetic stripe with the sense current flowing in the longitudinal direction, see Fig. 2.1(a). The easy magnetization axis is along the length of the stripe and its magnetization rotates coherently in an applied transverse magnetic field H_t. The resistance is highest for the magnetization aligned parallel to the current and lowest for a perpendicular alignment. This particular geometry is well suited for initial measurements because of the high degree of symmetry both electronically and magnetically.

2.3.1.1   Contact resistance and contact noise

First the contact resistance and contact noise were determined from resistance and noise measurements without applied magnetic fields. In Fig. 2.4(a), the total MRE resistance is depicted as a function of the length of the active area. The data points extrapolate

linearly towards an intercept of $19.3 \pm 0.4\Omega$, which is the contact resistance. All resistance measurements reported in this article are taken from MREs with an active area length of 70 μm and have not been corrected for this nonmagnetoresistive contact resistance, although it has been taken into account in the quantitative analysis of the noise. As a result of the contact resistance, all the reported MR-ratios will be lower than their intrinsic values.

The $1/f$ contact noise contribution has been determined by measuring S_V as a function of the dc sense current using a number of similar MREs with different lengths of the active area. To compare the $1/f$ noise between these MREs the slope of the linear part of the measured voltage spectral density at 1 Hz as a function of j^2 has been used [this is the resistance spectral density at 1 Hz $S_R = \alpha R^2/N \propto l$, also see Fig. 2.3(b)]. In Fig. 2.4(b), S_R has been plotted versus the active area length. It can be fitted with a linear curve with an intercept of $(1 \pm 2) \times 10^{-12}\Omega^2$/Hz due to $1/f$ contact noise. For the MREs with $l = 70$ μm the $1/f$ contact noise (if any) contributes negligibly to the overall $1/f$ noise level, and has therefore been discarded in the remainder of the Chapter.

2.3.1.2 Magnetoresistance

The resistance of the MRE is shown in Fig. 2.5(a) as a function of an applied transverse magnetic field H_t. The smooth, hysteresis free curve indicates coherent rotation of the magnetization from the longitudinal direction in zero field to the transverse direction at high fields. For a uniformly rotating magnetization a parabolic behavior of the resistance versus field is expected with the saturation field H_s equal to the sum of the demagnetizing field H_d and the anisotropy field H_a. The demagnetizing field can be approximated by $H_d \approx M_s t/w = 2.6$ kA/m (M_s is the saturation magnetic moment and t/w the thickness to width ratio of the magnetic layer) and $H_a \approx 0.4$ kA/m for Py, which yields $H_s \approx 3.0$ kA/m (dashed lines in Fig. 2.5). For low H_t the expected parabolic behavior is observed.

The rounding of the resistance curve near H_s reflects that the edges of the stripe saturate at higher fields than the middle of the stripe. An additional rounding comes from microscopic lateral variations of the magnetization direction [41], called ripple, which are most prominent near the saturation field [37,42]. Both the nonuniform rotation process and the ripple cause the maximum slope of the resistance curve to be reached at fields slightly below H_s. Even in the maximum available field, full saturation cannot be reached for the whole stripe in this geometry.

2.3.1.3 Noise

The dependence of S_V at 1 Hz on H_t is shown in Fig. 2.5(b); similar results have been obtained for a number of these MREs. Peaks are present at two fields close to where the maximum slope in the magnetoresistance curve is obtained. The peak values for the voltage spectral density are not equal. This is probably due to a small alignment error in the transverse magnetic field direction, which leads to an asymmetry in the measured S_V versus H_t curve. From the Hooge relation Eq. (2.1), values for the Hooge constant are found between $\alpha_{min} = 2.8 \times 10^{-3}$ and $\alpha_{max} = 1.7 \times 10^{-2}$ (i.e., $\sim 6 \times \alpha_{min}$). The min-
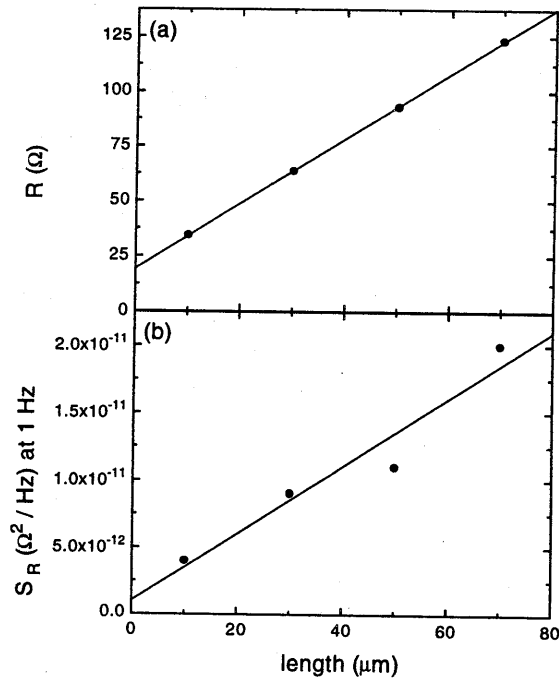
Figure 2.4: Influence of the length of the active area of an AMR-based MRE without barber pole metallization on (a) the resistance and (b) the scaled 1/f noise level at 1 Hz without applied fields. The lines are linear fits to the data.
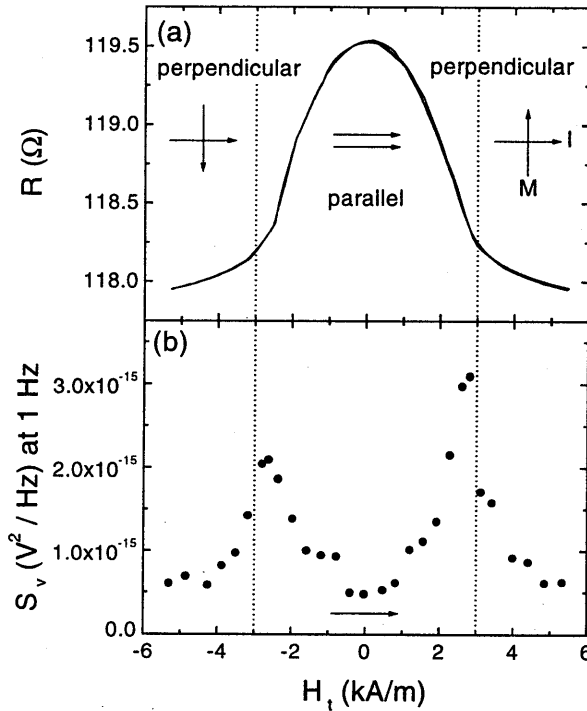
Figure 2.5: Transverse magnetic field dependence of (a) the resistance and (b) the voltage spectral density at 1 Hz for an AMR-based MRE without barber pole metallization. The MR-ratio for this MRE is 1.3% in the available field range. The noise spectra have been measured with a dc sense current $I_s = 5.74$ mA, corresponding to a film averaged sense current density $j = 1.9 \times 10^{10}$ A/m^2. The dashed lines indicate the estimated saturation fields $\pm H_s$ for this geometry. The data given in (b) are taken with increasing H_t, as indicated by the arrow.

imum value corresponds well to values commonly found for nonmagnetic metals [27]. The observed field dependence of the excess voltage spectral density can obviously not be explained by the resistance change, via the V_{dc}^2 term in the Hooge relation Eq. (2.1), as this would be a much smaller effect with a different field dependence. Thus the observed field dependence seems to clearly have a magnetic origin.

2.3.2 AMR-based MRE with barber pole

The second MRE design studied is also based on the AMR effect but its output has been linearized around zero field using the barber pole geometry [25]. On top of the active area a well conducting metallization layer is microfabricated in the form of a pattern of parallel stripes with the stripe axis rotated from the longitudinal direction [in the present case by 45°, see also Fig. 2.1(b)]. This effectively rotates the current direction in the

magnetic layer between the metallization stripes. However, the analysis of the magnetic response is complex due to the influence of the magnetic field generated by the sense current flowing in the metallization stripes. In addition, the metallization stripes cause a nonuniform current density which complicates the analysis of the magnetoresistance and 1/f noise.

2.3.2.1 Magnetoresistance

The magnetoresistive response for this MRE to an applied transverse magnetic field H_t is shown in Fig. 2.6(a). The smooth, essentially hysteresis free curve again indicates a coherent rotation of the magnetization direction. A small longitudinal magnetic field $H_l = 80$ A/m has in this case been applied to assure the same direction of this rotation for all applied sense currents and was sufficiently small to have negligible other effects on the measured results. As expected, the resistance varies linearly with H_t around zero field. For increasing transverse fields, a maximum or minimum in the resistance is reached when the magnetization direction is aligned along or perpendicular to the current direction in between the barber pole stripes, respectively. Increasing the transverse field further will decrease the resistance towards the zero field value for fields above the saturation field since the magnetization will again be at an angle of 45° with the current in between the barber pole stripes. The estimated saturation field is identical to H_s for the AMR-based MRE without barber pole and is indicated by dashed lines in Fig. 2.6. There is some rounding of the curve due to edge and ripple effects as discussed above and some asymmetry that probably arises from a small alignment error. Also in this MRE-type full saturation can not be reached in the maximum available magnetic field.

2.3.2.2 Noise

In Fig. 2.6(b) the H_t dependence of S_V at 1 Hz is presented. The result is representative for a number of measured MREs. Peaks are observed close to the three magnetic fields where the slope of the magnetoresistance curve shows a local maximum. The α values found for this MRE vary between $\alpha_{min} = 4.4 \times 10^{-2}$ and $\alpha_{max} = 2.4 \times 10^{-1}$ (i.e., $\sim 5.5 \times \alpha_{min}$), which are over an order of magnitude higher than for the AMR-based MRE without barber pole metallization. To obtain these α values, the total volume of the magnetic layer in the active area was used. Also, the same contact resistance as for the AMR-based MRE without barber pole was assumed, although the geometry of the contact metallization was different. The contact resistance and contact noise were not measured directly. As the α values depend quadratically on the resistance of the element and the assumed contact resistance is about half the total resistance, this could change the α values by at most a factor of four. Irrespective of these uncertainties, the magnitude of the excess noise level and its field dependence point also here to a magnetic origin.

The higher α values compared to the values found for the AMR-based MRE without barber pole might be explained, at least partly, in the following way: The metallization layer reduces the effective volume of the sample by creating "shorts" at the places where it overlaps the magnetic layer, thus effectively reducing the volume of the mag-
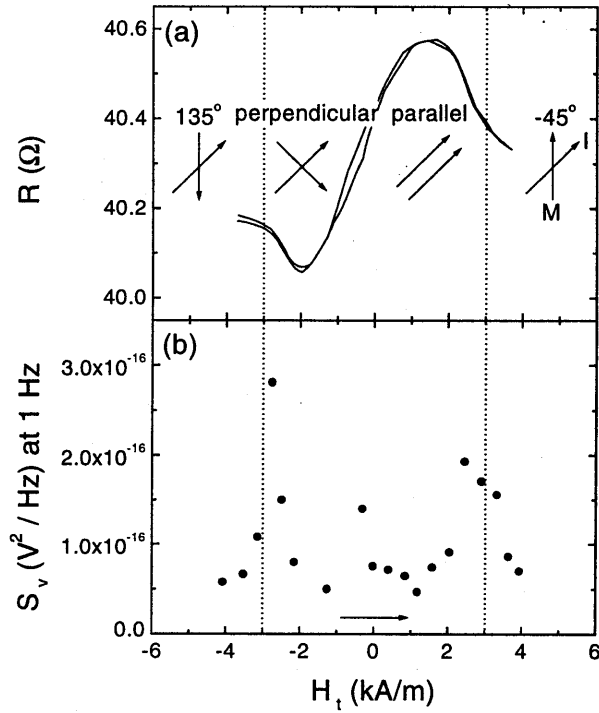
Figure 2.6: Transverse magnetic field dependence of (a) the resistance and (b) the voltage spectral density at 1 Hz for an AMR-based MRE with barber pole metalliza-tion. The MR-ratio for this MRE is 1.3%. The noise spectra have been measured with a dc sense current $I_s = 2.16$ mA, corresponding to a film averaged sense cur-rent density $j = 7.2 \times 10^9$ A/m^2 (not corrected for current distribution effects due to the metallization layer) and an applied longitudinal magnetic field $H_l = 80$ A/m. The dashed lines indicate the estimated saturation fields $\pm H_s$ for this geometry. The data given in (b) are taken with increasing H_t, as indicated by the arrow.

netic layer by some (unknown) factor depending on the current distribution within the element. Therefore, the active volume is overestimated, which in turn will increase the value of α obtained from Eq. (2.1). Insufficient information is presently available on the current distribution and contact resistance (noise) to make a quantitative correction for these effects.

2.3.3   GMR-based MRE

The last MRE design investigated is based on the GMR effect. Use is made of an ex-change biased spin-valve type element. The resistance is low when the magnetizations of the pinned and the free layer are aligned parallel and high for the antiparallel align-ment. The AMR effect associated with the rotation of the free layer with respect to the

current direction also contributes to the magnetoresistance.

2.3.3.1   Magnetoresistance

Fig. 2.7(a) shows the magnetoresistive response to an applied transverse magnetic field H_t. The smooth curve indicates a predominantly coherent rotation process, although some hysteresis is still present. For a uniformly rotating magnetization a linear variation of the resistance with the transverse field is expected due to the GMR effect. A parabolic variation due to the AMR effect in the rotating free layer is superimposed on the GMR effect. The resistance saturates to a low (high) resistance state when the applied transverse field is increased above the saturation field and the magnetization of the free layer is aligned (anti)-parallel to that of the pinned layer. This expected behavior is indeed observed.

There is some rounding near the saturation fields, which is, however, less pronounced than in the AMR-based MREs. The estimated demagnetizing field for the free layer $H_d \approx 0.7$ kA/m is smaller than in the previously discussed MREs due to the thinner magnetic layer. Added to the induced anisotropy field of $H_a \approx 0.4$ kA/m this leads to an estimated saturation field of $H_s \approx 1.1$ kA/m, which corresponds fairly well with the half-width of the magnetoresistance curve. We note that a shift in the magnetic field range may occur due to the magnetic coupling between the two magnetic layers (Néel and exchange coupling across the nonmagnetic layer and magnetostatic interactions due to the stray field from the pinned layer). Combined with the parabolic distortion of the magnetoresistance curve due to the AMR effect this may shift the center of the field range of highest sensitivity away from zero field.

2.3.3.2   Noise

In Fig. 2.7(b) the corresponding H_t dependence of S_V at 1 Hz is displayed for one of the measured MREs. Similar to the results of the AMR-based MREs a large peak is observed close to the field where the maximum slope of the magnetoresistance curve is obtained, in this case at $H_t \approx 0.6$ kA/m. A shoulder is observed extending to the negative saturation field and a smaller shoulder to higher fields which is, however, not observed in all (nominally equal) MREs. From the Hooge relation Eq. (2.1) values for the Hooge constant between $\alpha_{min} = 6.7 \times 10^{-3}$ and $\alpha_{max} = 2.8 \times 10^{-1}$ (i.e., $\sim 42 \times \alpha_{min}$) are found, while the shoulder has $\alpha_{shoulder} = 8.2 \times 10^{-2}$ (i.e., $\sim 12 \times \alpha_{min}$). These α values are obtained using the total volume of the multilayer and assuming the same contact resistance as for the AMR-based MRE without barber pole.

Here, α_{min} is more than twice the value obtained for the AMR-based MRE without barber pole. This might be caused by a nonhomogeneous current density (on which α depends quadratically) in the direction normal to the film plane, caused by the different conductivity of Py and Cu. As a result the active volume and thereby α would be overestimated. Also the interfaces might give rise to additional 1/f noise. We note that the ratio between the maximum (or shoulder) and minimum noise level is much higher than for the AMR-based MREs discussed above. Again, the field dependence and the amplitude of the excess noise point to a magnetic origin.
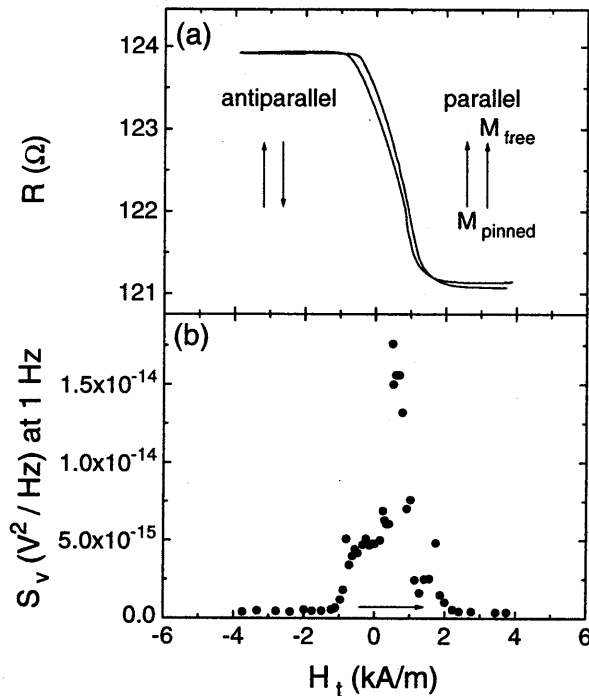
Figure 2.7: Transverse magnetic field dependence of (a) the resistance and (b) the voltage spectral density at 1 Hz for a GMR-based MRE. The MR-ratio for this MRE is 2.4%. The noise spectra have been measured with a dc sense current $I_s = 2.36$ mA, corresponding to a film averaged sense current density $j = 1.4 \times 10^{10}$ A/m^2. The data given in (b) are taken with increasing H_t, as indicated by the arrow.

2.4 Modeling

As has been shown above, the excess $1/f$ noise level depends strongly on the magnetic field. The origin of this excess noise may in principle be external, if it arises from noise sources in the experimental setup, as well as intrinsic. As will be shown in Section 2.4.1 noise from external sources cannot explain the experimental results presented in the previous section. In Section 2.4.2 a model will be presented for the excess $1/f$ noise that is intrinsic to the sensor element.

2.4.1 Field fluctuations

For our experimental setup we expect that the dominant nonintrinsic source of field dependent $1/f$ noise is a fluctuating applied magnetic field, due to $1/f$ noise in the current through the Helmholtz coils. Field fluctuations give rise to resistance noise via the

dependence of the resistance on the magnetic field:

$$S_R(f, H_t) = \left(\frac{\partial R}{\partial H_t'} \bigg|_{H_t' = H_t} \right)^2 \times S_{H_t}(f), \qquad (2.2)$$

where $S_R(f, H_t)$ is the resistance spectral density and $S_{H_t}(f)$ the spectral density of the applied magnetic field. The influence of the field noise is estimated from the spectral density in the current through the Helmholtz coils and is for the most noisy configuration found to be $S_{H_t} \approx 2.5 \times 10^{-6}$ (A/m)^2/Hz at 10 Hz, decreasing as 1/f to lower values at higher frequencies. The estimated maximum resistance noise corresponding to this level is at least one order of magnitude lower as compared to the measured 1/f noise levels. Also, no cross-correlation was found between the fluctuations in the resistance of the MRE and the fluctuations of the current through the Helmholtz coils. Therefore, field fluctuations may be discarded as an explanation for the observed field dependence of the resistance noise.

2.4.2   Thermal excitations

A qualitative understanding of the measured field dependence of the excess 1/f noise levels can be obtained from a model based on thermal excitation of the magnetic moment direction at a given nonzero temperature. The magnetic fluctuations are translated into resistance fluctuations via the dependence of the resistance on the angle of the magnetization.

In this Section we calculate the effect of thermal excitations on the variances of the magnetization angle and the resistance. To obtain the variance of voltage, the variance of the resistance has to be multiplied by the dc sense current squared. These variances are equal to the frequency integrated corresponding spectral density. The frequency dependence is not calculated directly. However, it is well known that thermal excitations lead to 1/f noise when a sufficiently broad range of relaxation times is available around the investigated frequency range [27]. Indeed, ferromagnetic relaxation mechanisms have been measured with time constants in the μs range to the Ms range, see, e.g., Refs. [43] and [44]. Since the explanation of the frequency dependence of the noise is analogous to that for nonmagnetic materials [27] we focus completely on the magnetic field dependence of the noise which is specific for magnetic materials. To study the magnetic field dependence it is sufficient to consider the integrated noise spectrum, i.e., the variance.

In this Section, we will restrict the calculations to a single magnetic layer with a uniform magnetization direction, i.e., a single magnetic domain with infinite intralayer exchange energy. The magnetic behavior of this domain is described within a Stoner-Wohlfahrt model which has been used extensively to describe the equilibrium properties of MREs, see, e.g., Ref. [45]. The total magnetic energy E of the system is expressed as the sum of all relevant interaction energies and depends on the direction of the magnetization vector which is assumed to remain in the film plane. The variances of the magnetization angle and the resistance are calculated using Boltzmann statistics.

Within this description, the expectation value $\langle A \rangle$ of a quantity A at finite temperatures is given by:

$$\langle A \rangle = \frac{1}{Z} \int_0^{2\pi} d\phi \; A(\phi) \exp\left[-E(\phi)/kT\right], \tag{2.3a}$$

$$Z = \int_0^{2\pi} d\phi \; \exp\left[-E(\phi)/kT\right], \tag{2.3b}$$

where ϕ is the angle between the magnetization and the longitudinal axis, see Fig. 2.1. The variance of the quantity A is defined as $\sigma_A^2 = \langle A^2 \rangle - \langle A \rangle^2$. To lowest order in temperature, the variance σ_ϕ^2 of the magnetization angle around the equilibrium value ϕ_0 (which we assume to be nondegenerate) can be obtained by applying the stationairy phase approximation to Eq. (2.3), which yields:

$$\sigma_\phi^2 = kT \left(\left. \frac{\partial^2 E}{\partial \phi^2} \right|_{\phi = \phi_0} \right)^{-1}. \tag{2.4}$$

This result is very similar to the expression for the variance in ϕ due to ripple caused by lateral variations in the anisotropy direction, since both effects follow from a similar energy minimalization procedure (see, e.g., Ref. [46] for an overview of ripple theory). The difference is that the latter results in lateral (static) variations of the magnetization direction, which show up in microscopy images [37, 42] and in global magnetization measurements [41], while the former results in variations in the time domain.

For small angle fluctuations, the variance σ_R^2 of the resistance is proportional to the variance σ_ϕ^2 of the magnetization angle:

$$\sigma_R^2 = \left(\left. \frac{\partial R}{\partial \phi} \right|_{\phi = \phi_0} \right)^2 \times \sigma_\phi^2$$

$$= kT \left(\left. \frac{\partial R}{\partial \phi} \right|_{\phi = \phi_0} \right)^2 \times \left(\left. \frac{\partial^2 E}{\partial \phi^2} \right|_{\phi = \phi_0} \right)^{-1}. \tag{2.5}$$

Below, the transfer factor $(\partial R/\partial \phi|_{\phi=\phi_0})^2$ between σ_R^2 and σ_ϕ^2 is abbreviated as η^2.

This result has an intuitive interpretation: the magnetization direction fluctuates in around the energy minimum with a variance inversely proportional to the curvature at the minimum [see Fig. 2.8(b)]. The curvature at the minimum is a measure for the magnetic stability of the element, a deeper minimum meaning a more stable magnetization direction. The angle fluctuations result in resistance fluctuations via the magnetoresistance effect.

2.4.3 Application to model systems

In this Section the results will be presented of calculations for a number of model systems that correspond to the systems investigated experimentally. We model all systems
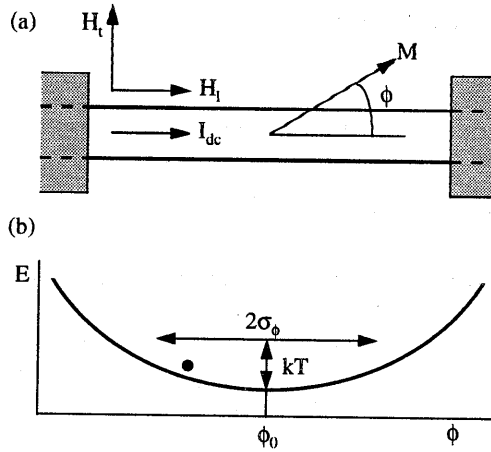
Figure 2.8: Schematic overview of (a) the simplified model system and (b) the energy diagram. The magnetization direction ϕ fluctuates around the minimum energy value ϕ_0 due to thermal excitations.

by a single magnetic entity in the form of an infinite stripe of width w and thickness t and a uniform magnetization with an angle ϕ with respect to the long axis of the stripe [see Fig. 2.8(a)]. The magnetic energy density $E(\phi)$ of each system can be written as the sum of the Zeeman, anisotropy and demagnetization energy densities:

$$E(\phi) = -\mu_0 M_s \left(H_t \sin \phi + H_l \cos \phi \right)$$
$$- K \cos^2 \phi - \frac{1}{2} \mu_0 M_s H_d \cos^2 \phi, \tag{2.6}$$

where M_s is the saturation magnetization, K the in-plane (induced) uniaxial anisotropy constant, and $H_{t(l)}$ the applied transverse (longitudinal) magnetic field. The demagnetization field is approximated by $H_d \approx M_s t/w$. Within this model H_d does not depend on the transverse coordinate due to the assumed uniform magnetization direction. The energy terms that occur for GMR-based systems due to interlayer and magnetostatic coupling between the free and pinned layer are neglected. Still assuming a homogeneous magnetization in the free layer, these terms only give rise to a shift along the magnetic field axis.

Without longitudinal field, the magnetization will saturate at the saturation field H_s:

$$H_s = \frac{2K}{\mu_0 M_s} + H_d. \tag{2.7}$$

By using this field to normalize the applied magnetic field strengths a relatively simple expression is obtained for the normalized energy density $e(\phi)$ (normalized quantities are denoted by lowercase characters):

$$e(\phi) = \frac{E(\phi)}{\mu_0 M_s H_s}$$

$$= -\frac{1}{2}\cos^2\phi - h_t \sin\phi - h_l \cos\phi, \qquad (2.8)$$

where $h_t = H_t/H_s$ and $h_l = H_l/H_s$. The dependencies of the resistance on the angle ϕ have been modeled by:

$$r_{\mathrm{AMR}}(\phi) = \frac{R_{\mathrm{AMR}}(\phi) - R_0}{\Delta R_{\mathrm{AMR}}} = \cos^2\phi, \qquad (2.9a)$$

$$r_{\mathrm{BP}}(\phi) = \frac{R_{\mathrm{BP}}(\phi) - R_0}{\Delta R_{\mathrm{AMR}}} = \cos^2\left(\phi - \frac{\pi}{4}\right), \qquad (2.9b)$$

$$r_{\mathrm{GMR}}(\phi) = \frac{R_{\mathrm{GMR}}(\phi) - R_0}{\Delta R_{\mathrm{GMR}}} = \frac{1}{2}\left(1 - \sin\phi\right), \qquad (2.9c)$$

in which R_0 is the minimum resistance and ΔR_{AMR} and ΔR_{GMR} are the maximum resistance changes for AMR and GMR, respectively.

Using these expressions, the field dependence of the variance of the resistance is calculated for the three MRE types investigated and a comparison with the experimentally determined $1/f$ noise level is made. First, the case without longitudinal magnetic field will be described. Later, the dependence on this field will also be discussed, as well as the influence of a small AMR contribution to the noise of a GMR-based MRE.

2.4.3.1 Without longitudinal field

In Fig. 2.9 the results of the model calculations are presented for the three different MRE configurations [only AMR in figures 2.9(a)–2.9(e), AMR using the barber pole geometry in figures 2.9(f)–2.9(j) and only GMR in figures 2.9(k)–2.9(o)] for applied transverse magnetic field only, i.e. $h_l = 0$. The top two rows of Fig. 2.9 represent the variation upon applying a transverse magnetic field of the equilibrium magnetization direction $\sin\phi_0$ [figures 2.9(a), 2.9(f), and 2.9(k)] and the equilibrium resistance $r(\phi_0)$ [figures 2.9(b), 2.9(g), and 2.9(l)]. These are calculated from the equilibrium angle ϕ_0 that follows from Eq. (2.8), and substitution in Eq. (2.9). The field variations of the variances of the magnetization angle σ_ϕ^2 [third row, figures 2.9(c), 2.9(h), and 2.9(m)] and the resistance σ_r^2 [bottom row, figures 2.9(e), 2.9(j), and 2.9(o)] are obtained from Eq. (2.4) and Eq. (2.5), respectively. The transfer factor $\eta^2 = (\partial R/\partial\phi|_{\phi=\phi_0})^2$ between these quantities is shown in the fourth row [figures 2.9(d), 2.9(i), and 2.9(n)].

The variation of the magnetization upon applying a transverse magnetic field is the same for all three measuring geometries since all magnetic entities are assumed to be identical. As can be seen in figures 2.9(a), 2.9(f), and 2.9(k), for $|h_t| < 1$ the transverse magnetization component $M_s \sin\phi_0$ increases linearly with transverse applied field. This is the well known hard-axis magnetization curve for magnetic systems in which the (effective) uniaxial anisotropy is dominant. For $|h_t| \geq 1$ the magnetization direction is along the field direction.

The magnetization direction is relatively stable at small applied fields and again in high applied fields, as may be seen from the variance σ_ϕ^2 of the magnetization angle [fig-
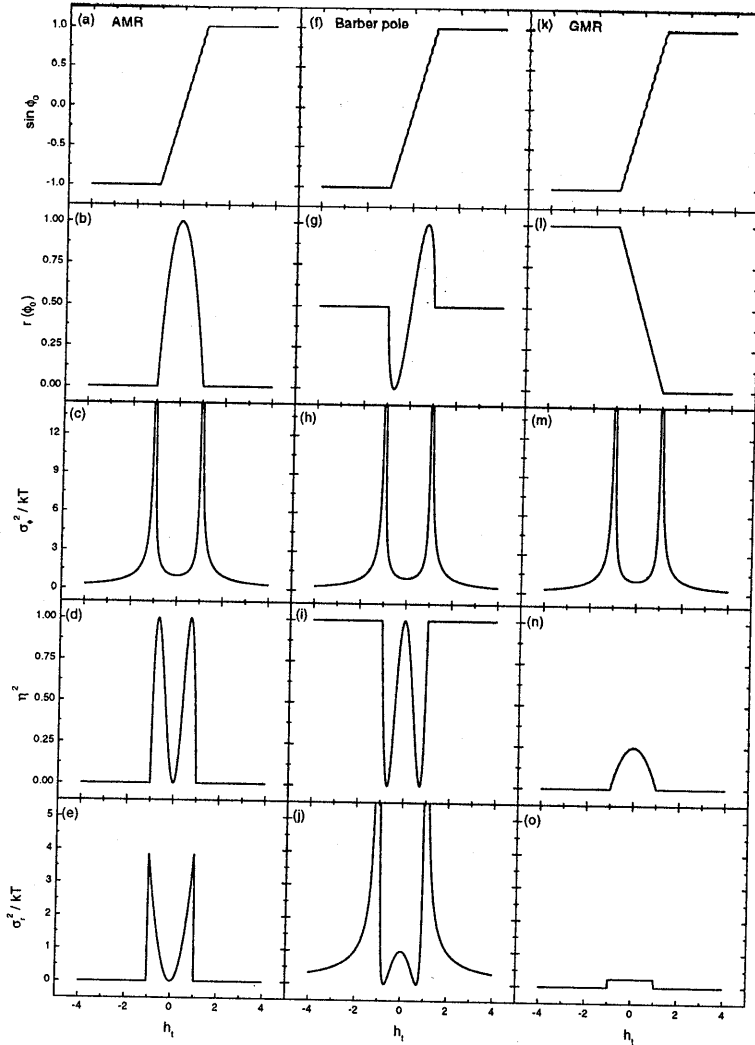
Figure 2.9: Results of the model calculations for MREs based on (a)–(e) the AMR effect, (f)–(j) the AMR effect linearized using the barber pole geometry, and (k)–(o) the GMR effect. Only a transverse magnetic field is applied (i.e., $h_l = 0$).

ures 2.9(c), 2.9(h), and 2.9(m)]. At the saturation field ($|h_t| = 1$), however, σ_ϕ^2 diverges, a characteristic result which is also present in Hoffmann's linear ripple theory [46] and is qualitatively confirmed by microscopy [37, 42] and magnetization [41] data.

The field dependence of the resistance noise for the AMR-based MRE may be understood from figures 2.9(a)–2.9(e). The resistance change [Fig. 2.9(b)] upon applying a transverse magnetic field shows the characteristic parabolic behavior for $|h_t| < 1$

and saturates to the low resistance state at higher fields. The variance σ_ϕ^2 of the magnetization angle [Fig. 2.9(c)] diverges as the saturation field is approached, but this is compensated by a vanishing transfer factor η^2 [Fig. 2.9(d)]. The result is a finite variance σ_r^2 of the resistance at $|h_t| = 1$ [Fig. 2.9(e)]. For $|h_t| < 1$ the variance of the resistance increases quadratically with the field, i.e., $\sigma_r^2/kT = 4h_t^2$. For higher fields σ_r^2 is zero.

The results for the AMR-based MRE with the barber pole geometry are presented in the figures 2.9(f)–2.9(j). For this MRE, the divergence of the variance σ_ϕ^2 of the magnetization angle [Fig. 2.9(h)] is not compensated by a vanishing transfer factor η^2 [Fig. 2.9(i)] at $|h_t| = 1$, and therefore the variance σ_r^2 of the resistance [Fig. 2.9(j)] diverges, too. The low field part ($|h_t| \ll 1$) may be approximated by $\sigma_r^2/kT \approx (h_t - 1)(h_t + 1)$. The transfer factor η^2 [Fig. 2.9(i)] is nonzero above saturation ($|h_t| > 1$), and therefore this MRE does have a nonzero variance of the resistance $\sigma_r^2/kT = (|h_t| - 1)^{-1}$ in the saturated state, unlike the other two MREs.

Figures 2.9(k)–2.9(o) show the results of the model calculations for the GMR-based MRE. For these calculations, it is assumed that only the free layer is able to fluctuate, i.e., the pinned layer is held fixed rigidly with the magnetic moment aligned along the positive h_t direction or, i.e., the pinning to the antiferromagnet is assumed to be sufficiently strong. As discussed above, no magnetic interactions have been assumed between both magnetic layers. For this MRE type, the transfer factor η^2 [Fig. 2.9(n)] compensates the divergence at $|h_t| = 1$ of the variation σ_ϕ^2 of the magnetization angle [Fig. 2.9(m)]. Like for the AMR-based MRE, this leads to a finite variance σ_r^2 of the resistance at $|h_t| = 1$ [Fig. 2.9(o)]. Within this model, the variance of the resistance $\sigma_r^2/kT = \frac{1}{4}$ for $|h_t| < 1$. Because the transfer factor vanishes above saturation also σ_r^2 disappears for $|h_t| > 1$.

Both AMR-based MREs show a qualitative similarity between field dependence of the calculated variance of the resistance and the experimentally observed $1/f$ noise level at 1 Hz. The AMR-based MRE without barber pole indeed shows the double peak structure [Fig. 2.5(b)], where (as discussed in Sec. 2.3) the difference in the two observed peak heights may be explained by a misalignment of the applied magnetic field. The width of the peaks may be explained by demagnetization or ripple effects. Also for the AMR-based MRE with barber pole the theory reproduces the three experimentally observed peaks [Fig. 2.6(b)], two large peaks at the saturation fields and a smaller peak at zero field. For the GMR-based MRE the agreement between experiment and theory is less satisfactory. The experiment shows a huge peak [Fig. 2.7(b)] where the calculations predict a plateau. It will be shown below that by taking a small superimposed AMR effect into account theory will yield a better prediction.

It is noted that within the present model the field dependence of the noise contributions due to thermal excitations and due to field fluctuations are identical for fields $|h_t| \leq 1$, if the amplitude of the field fluctuations is independent of the applied field, if no longitudinal magnetic field is applied, and if only a $\cos^2\phi$ anisotropy term is present. When $h_l \neq 0$ or when the anisotropy also contains other terms, both contributions show a different dependence on the applied transverse magnetic field.
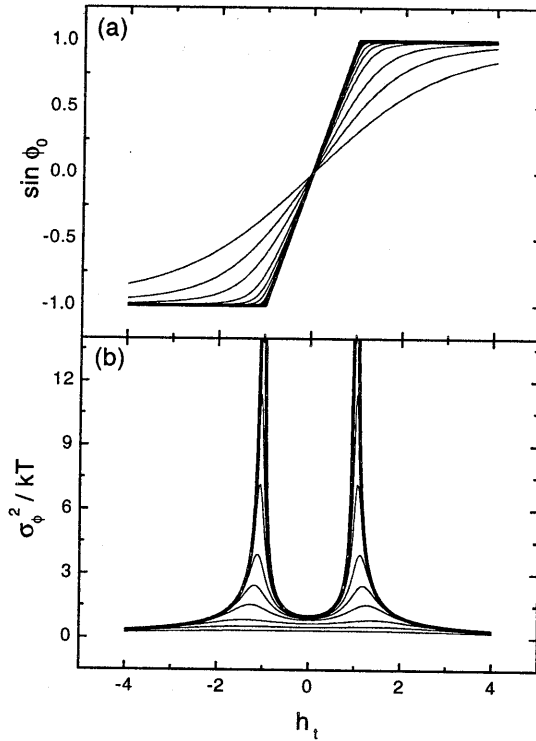
Figure 2.10: The calculated effect of a longitudinal magnetic field on (a) the magnetic response and (b) the variance of the magnetization angle of a single magnetic film in an applied transverse field. The different curves are for $h_l = 0$ (thick) and $h_l = 0.01, 0.02, 0.05, 0.1, 0.2, 0.5, 1$, and 2 (thin), increasing h_l values correspond to (a) a decreasing slope of the $\sin \phi_0$ curve and (b) a decreasing σ_ϕ^2.
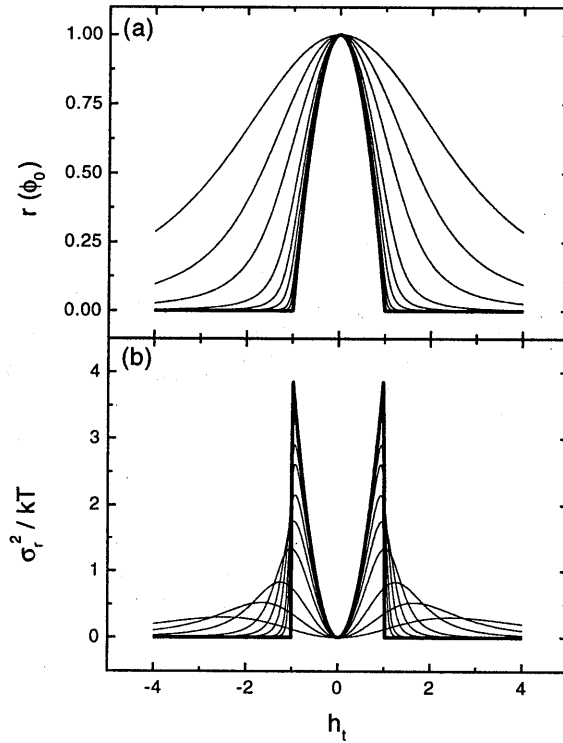
Figure 2.11: The calculated effect of an applied longitudinal magnetic field on (a) the MR curve and (b) the variance of the resistance due to thermal excitations of the magnetization direction, for an AMR-based MRE. The different curves are for $h_l = 0$ (thick) and $h_l = 0.01, 0.02, 0.05, 0.1, 0.2, 0.5, 1$, and 2 (thin), increasing h_l values corresponding to (a) a broadening of the MR curve and (b) a decreasing σ_r^2 at $|h_t| = 1$ (b).
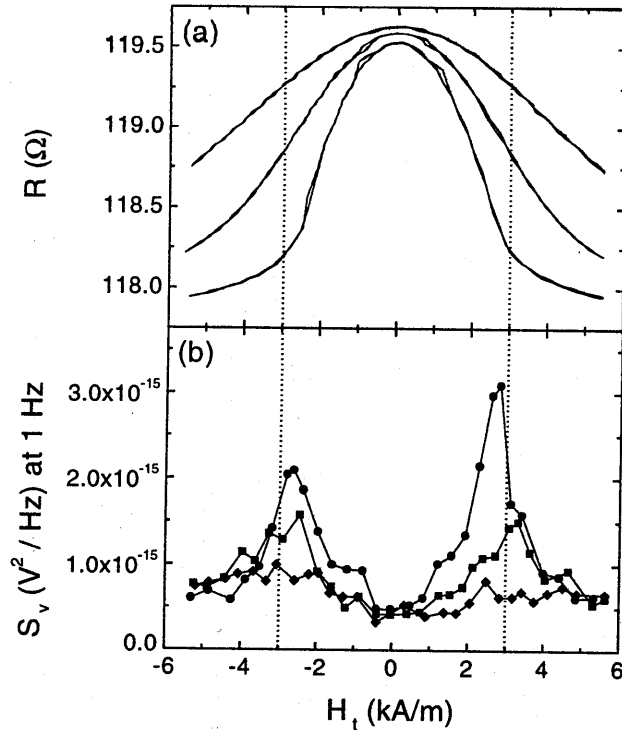
Figure 2.12: Experimental observation of the effect of an applied longitudinal magnetic field on (a) the MR curve and (b) the voltage spectral density at 1 Hz for an AMR-based MRE. The applied longitudinal fields are $H_l = 0$ (circles), 0.4 (squares), and 1.6 (diamonds) kA/m, corresponding to $h_l = 0, 0.13$, and 0.51, respectively. The dashed lines indicate the estimated saturation fields $\pm H_s$ for this geometry.

2.4.3.2   With longitudinal field

In certain applications a longitudinal field is applied to an MRE, e.g., when domain wall formation should be prevented or when a specific rotation direction is desired. In some cases the longitudinal field is not applied externally, but is already present due to geometrical effects. For example, the current distribution in the metallization layer of the barber pole geometry will generate a field with a longitudinal component.

The application of a longitudinal field can also be used as a tool to obtain additional insight in the origin of the excess 1/f noise. The noise level depends on the magnetic state of the system, which can be changed by the application of a longitudinal field. This can be used as an additional test for the model presented above. In Fig. 2.10 the calculated effect of a longitudinal field on the magnetic properties of a single magnetic layer is shown. The magnetic response [Fig. 2.10(a)] is smeared out, reflecting the smoother reversal of the magnetic moment upon applying a transverse magnetic field. As a result

the variance σ_ϕ^2 of the magnetization angle [Fig. 2.10(b)] reduces in amplitude in the whole field range and the divergences at $|h_t| = 1$ disappear.

A similar broadening is observed in the calculated magnetoresistance curve of an AMR-based MRE, as shown in Fig. 2.11(a) for increasing applied longitudinal magnetic fields. This means that the MRE sensitivity (slope of the magnetoresistance curve) decreases. As can be seen in Fig. 2.11(b), also the variance σ_r^2 of the resistance decreases, especially around $|h_t| = 1$. Another observation is the shift of the maximum in σ_r^2 to higher transverse fields for increasing longitudinal fields.

Qualitatively, these trends are also observed in the experiment as shown in Fig. 2.12. The resistance curve [Fig. 2.12(a)] becomes broader as the longitudinal field is increased and S_V at 1 Hz decreases significantly [Fig. 2.12(b)]. The shift in the peak position is not resolved experimentally.

The same trends are predicted for the AMR-based MRE with barber pole metallization, as is shown in Fig. 2.13. The resistance curve broadens [Fig. 2.13(a)], the maximal variance of the resistance decreases and the field at which the maximum is obtained shifts to higher values [Fig. 2.13(b)]. Also for the GMR-based MRE a broadening of the resistance [Fig. 2.14(a)] and the variance of the resistance [Fig. 2.14(b)] is predicted.

2.4.3.3   Combined GMR and AMR

In the experimental GMR-based MRE, in addition to the GMR effect also an AMR effect is present due to the rotation of the free magnetic layer. This AMR effect, although small compared to the GMR effect, will also have an influence on the noise. Therefore, model calculations have been performed in which both the GMR and the AMR effect are present. The resistance is modelled by:

$$r_{\text{AMR+GMR}}(\phi) = \frac{1}{2}\,(1 - \sin\phi) + \delta\cos^2\phi, \qquad (2.10)$$

where δ now represents the amplitude of the AMR effect relative to the GMR effect. Using this formula, the resistance and noise have been plotted in Fig. 2.15 for $\delta = 0.1$. Fig. 2.15(a) shows that as a result of the additional AMR effect the magnetoresistance curve is nonlinear. The field dependence of the variance of the resistance due to thermal excitations of the magnetization as shown in Fig. 2.15(b) is found to be not simply the addition of the contributions due to GMR and AMR. The values at $h_t = \pm 1$ are found to be strongly different and the variance of the resistance (as well as the sensitivity) is expected to be lower than for a pure GMR-based MRE for $h_t < 0$. The field dependence of the variance of the resistance can be looked upon as an asymmetric single peak, with a maximum at, or somewhat below $h_t = 1$ for small applied longitudinal fields, decreasing gradually down to the negative saturation field. This asymmetric field dependence is roughly as observed in the experiment [Fig. 2.7(b)]. It should be noted that the amount of asymmetry of the noise is very sensitive to the ratio between the GMR and AMR effect.
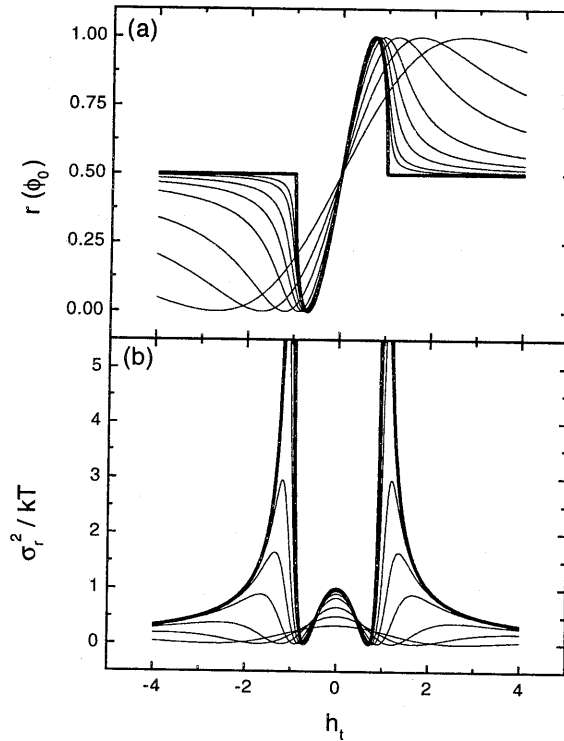
Figure 2.13: The calculated effect of an applied longitudinal magnetic field on (a) the MR curve and (b) the variance of the resistance due to thermal excitations of the magnetization direction, for an AMR-based MRE with barber pole metallization. The different curves are for $h_l = 0$ (thick) and $h_l = 0.01, 0.02, 0.05, 0.1, 0.2, 0.5, 1,$ and 2 (thin), increasing h_l values corresponding to (a) a broadening of the MR curve and (b) a decreasing σ_r^2 at $h_t = 0$ (b).
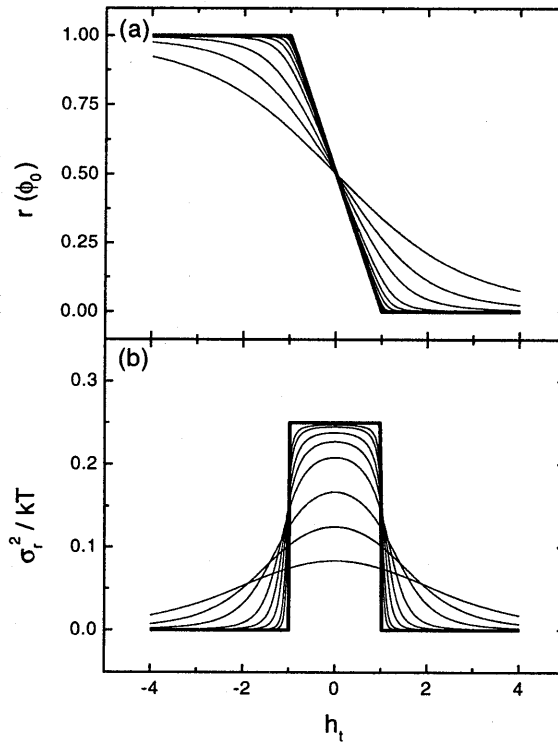
Figure 2.14: The calculated effect of an applied longitudinal magnetic field on (a) the MR curve and (b) the variance of the resistance due to thermal excitations of the magnetization direction, for a GMR-based MRE. The different curves are for $h_l = 0$ (thick) and $h_l = 0.01, 0.02, 0.05, 0.1, 0.2, 0.5, 1$, and 2 (thin), increasing h_l values corresponding to (a) a broadening of the MR curve and (b) a decreasing σ_r^2 at $|h_t| \leq 1$ (b).
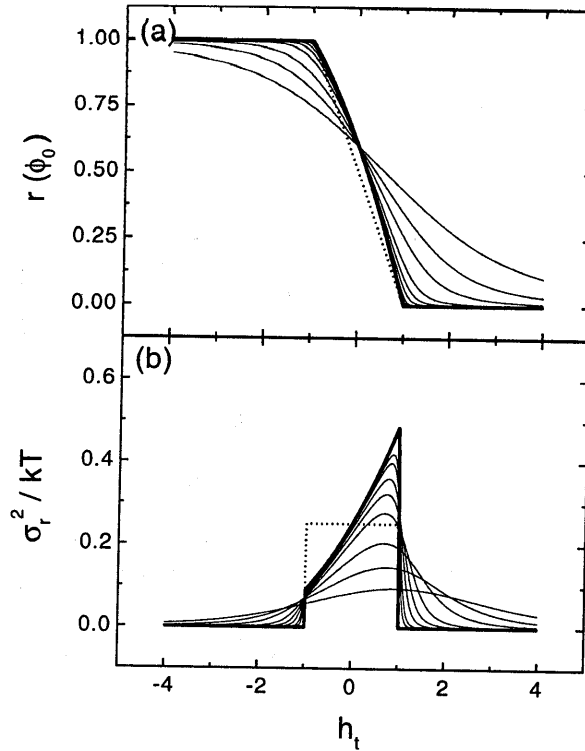
Figure 2.15: The calculated effect of an applied longitudinal magnetic field on (a) the MR curve and (b) the variance of the resistance due to thermal excitations of the magnetization direction, for an MRE in which both GMR and AMR are present ($\delta = 0.1$). The different curves are for $h_l = 0$ (thick) and $h_l = 0.01, 0.02, 0.05,$ $0.1, 0.2, 0.5, 1,$ and 2 (thin), increasing h_l values corresponding to (a) a broadening of the MR curve and (b) a decreasing σ_r^2 at $|h_t| \leq 1$. The dashed lines are the results for only GMR (i.e., $\delta = 0$) without applied longitudinal field (i.e., $h_l = 0$).

2.5 Discussion and Conclusions

In this article we have presented results of resistance noise measurements on microfabricated magnetoresistive elements based on either the AMR or the GMR effect. These MREs are designed to behave as a single magnetic domain, i.e., domain walls are excluded from the active area of the element. The resistance noise spectra are obtained for frequencies between 10 Hz and 100 kHz under dc sensor operation at room temperature. Thermal resistance noise was the dominant noise source above about 10 kHz. At low frequencies the resistance noise is found to be dominated by a magnetic field dependent 1/f contribution. The 1/f noise is low in high applied magnetic fields and increases by a factor of ~six (AMR-based elements) to ~40 (GMR-based elements) in the most sensitive region of the magnetoresistance curve. The low value is comparable

to the $1/f$ noise level which is also found for nonmagnetic metals. The difference between the relative increase in noise level between the AMR- and GMR-based elements can be understood from the larger magnetoresistance effect, the reduced thickness of the layers, and the lower saturation fields for the GMR-based MRE.

The field dependence of the excess $1/f$ contribution could be qualitatively understood from a simple Stoner–Wohlfahrt type model. The model calculates to lowest order in T the variance of the resistance of a thermally excited magnetic moment. The fluctuations of the magnetic moment direction result in resistance fluctuations via the magnetoresistance effect.

The agreement between the model calculations and the experiment is satisfactory for the investigated AMR-based MREs, while for the GMR-based MREs only a rough agreement could be obtained. More detailed measurements of the dependence of the resistance noise on both the applied longitudinal and transverse magnetic fields are needed to test the model. Future improvements of the model should include effects which have been neglected in this article, such as the influences of demagnetization effects, which cause a nonuniform magnetization profile, local anisotropy variations, which cause ripple, coupling between the two magnetic layers, and the coupling between the pinned magnetic layer and the antiferromagnetic layer.

Part II

Magnetic Tunnel Junctions

Chapter 3

Introduction to Magnetic Tunnel Junctions

Tunnel junctions consist of two electrodes, with an insulating separation layer separating the two, usually refered to a the "barrier" layer, see Fig. 3.1. When the insulating layer is very thin (order of 1 nm), electrons can "tunnel" through this forbidden region as a consequence of the wave-like nature of electrons, and can only be described in terms of quantum mechanics.

The tunnel current shows a superlinear dependence on the applied bias voltage V. From the form of the current-voltage curve, valuable information can be obtained about the barrier shape. Using the WKB approximation, Simmons [47] derived an often used analytical formula for the the current density J (expressed in A/cm^2) for junctions with a symmetric potential barrier shape, see Fig. 3.2,

$$
J(V) = \frac{6.17 \times 10^{10}}{t_{\text{bar}}^2} \left[\left(\overline{\phi} - V/2 \right) \exp\left(-1.025 \sqrt{\overline{\phi} - V/2}\, t_{\text{bar}} \right) \right.
$$
$$
\left. - \left(\overline{\phi} + V/2 \right) \exp\left(-1.025 \sqrt{\overline{\phi} + V/2}\, t_{\text{bar}} \right) \right],
$$

(3.1)

where $\overline{\phi}$ (expressed in V) denotes the average barrier height, measured from the Fermi level of the electrodes, t_{bar} (expressed in Ångstroms) denotes the barrier width. When two different electrodes are present, the barrier shape decomes asymmetric. This leads to deviation to Eq. (3.1), which has been described by Brinkman [48] within the same formalism,

$$
J(V) = G_0 \left[V - C_2 \frac{t_{\text{bar}} \Delta \phi}{\overline{\phi}^{3/2}} V^2 + C_3 \frac{t_{\text{bar}}^2}{\overline{\phi}} V^3 \right],
$$

(3.2)
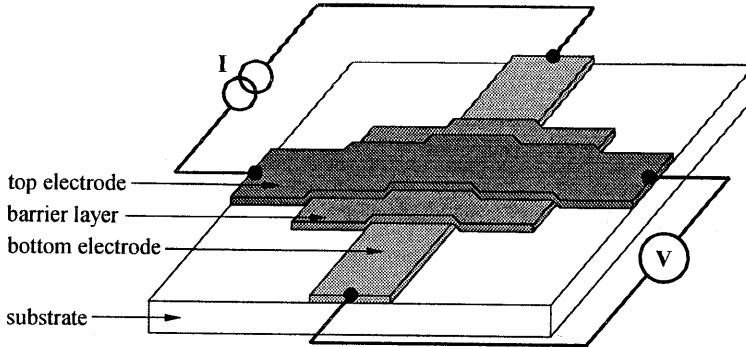
Figure 3.1: Basic tunnel junction layout, with corresponding connection for transport measurements.
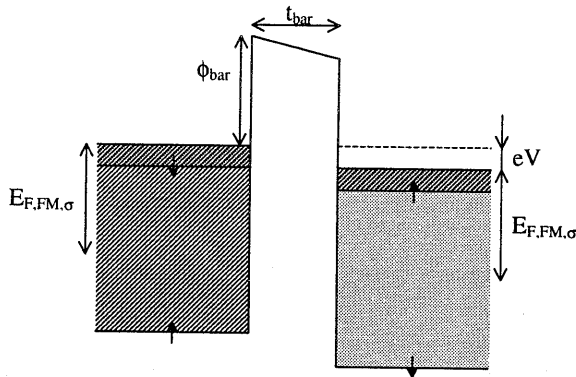
Figure 3.2: Schematic representation of the potential energy shape of a symmetric tunnel junction, in the antiparallel alignment.

where now $\overline{\phi} = (\phi_{\text{left}} + \phi_{\text{right}})/2$, the asymmetry parameter $\Delta\phi = \phi_{\text{left}} - \phi_{\text{right}}$, and

$$G_0 = C_1 \frac{\sqrt{\overline{\phi}}}{t_{\text{bar}}} \exp\left(-1.025\sqrt{\overline{\phi}}\, t_{\text{bar}}\right),\tag{3.3}$$

where the prefactors are given by $C_1 = 3.16 \times 10^{10}\,\text{m}^{-1}\text{V}^{-1.5}$, $C_2 = 0.0854\,\text{m}^{-1}\text{V}^{-1.5}$, and $C_3 = 0.0984\,\text{m}^{-2}\text{V}^{-2}$. It should be noted that due to the approximations made, both Equations do not contain information about the density of electron states of either electrode.

Since the discovery in the fifties that in superconductor based tunnel junctions the tunnel current shows a dependency on the density of electron states, speculations have been made about junctions with the superconductors replaced by ferromagnets. In ferromagnets, the density of states of electrons is spin-split due to the exchange interaction and a magnetic moment results from the difference in the number of majority and
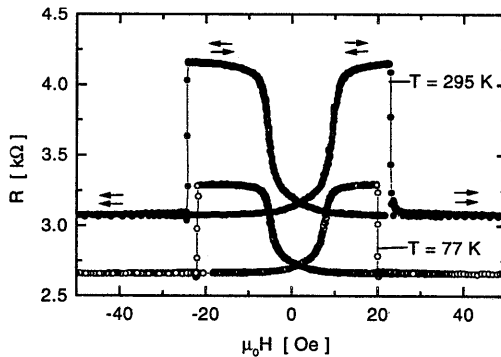
Figure 3.3: Typical resistance versus applied magnetic field curves for a $Co/Al_2O_3/Ni_{80}Fe_{20}$ junction at two temperatures. Arrows indicate the alignment of the magnetic moments of the two ferromagnetic layers.

minority electrons. It also results in a spin-asymmetry (polarization) in the electron density of states near the Fermi energy. When the current would also be related to the density of states in junctions containing magnetic metals instead of superconductors, this should directly lead to a spin-polarized tunnel current. Indeed, in the early seventies Tedrow and Meservey [49] showed that the tunnel current in a superconductor-isolator-ferromagnet junction was spin-polarized and that the tunnel process in itself was spin-conserving.

The first pioneering experiments on a ferromagnet-insulator-ferromagnet tunnel junction were presented by Julliere in 1975 [15]. At low temperatures, he found a 14% magnetoresistance effect, i.e., a change in resistance when a magnetic field is applied, in a Fe-Ge-Co junction which was oxidized after depositing Ge. The results could be accounted for with a simple model based on evidence gathered from the experiments with superconductor based junctions. The tunnel conductance ($G = I/V = 1/R$) is given by the product $G \propto N_1 N_2$ of two factors, one for each electrode, representing, within the most simplified approach, the effective density of states at the Fermi level. For ferromagnetic electrodes, the factor N_i depends on the electron spin σ. Since the spin is conserved during the tunnel process, the total conductance is the sum of two independent spin contributions: $G = G_\uparrow + G_\downarrow$.

For a ferromagnet-insulator-ferromagnet junction, two extreme situations can be distinguished, as can be seen in Fig. 3.3. In the first situation, the magnetic moments of both electrodes are aligned parallel (P). Both electrodes will have majority electrons of the same spin, and therefore $G_{P,\uparrow} = N_{1,maj} N_{2,maj}$ and $G_{P,\downarrow} = N_{1,min} N_{2,min}$. In the second case, the magnetic moments of both electrodes are aligned antiparallel (AP), for example by reversing the magnetic moment of ferromagnet 2 under the influence of an externally applied magnetic field. In that case, the majority (and minority) electrons of both ferromagnets have opposite spins. The tunnel conductances will in this case be given by $G_{AP,\uparrow} = N_{1,maj} \times N_{2,min}$ and $G_{AP,\downarrow} = N_{1,min} \times N_{2,maj}$, i.e., different from the situation with parallel aligned magnetic moments.

The junction magnetoresistance (JMR), sometimes also called tunnel magnetoresistance (TMR), can now be defined as the ratio of the difference in conductance ($\Delta G = G_P - G_{AP}$) and the conductance in either one of the magnetic alignments (G_P or G_{AP}), each normalization resulting in a different value for the JMR. This definition can also be written in terms of the tunnel resistances R_{AP} and R_{AP}, respectively. Unfortunately, both normalizations are widely used in the literature and which definition is used is not always clearly stated. Even in this thesis both definitions have been used, due to historical reasons. To avoid further confusion, the JMR is always denoted as in its definition, thus either $\Delta R/R_P$ or $\Delta R/R_{AP}$. Using Julliere's model [15,50], the magnetoresistance, in terms of the tunnel resistances, is given by:

$$\frac{\Delta R}{R_P} = \frac{2P_1 P_2}{1 - P_1 P_2}, \qquad \text{or} \tag{3.4}$$

$$\frac{\Delta R}{R_{AP}} = \frac{2P_1 P_2}{1 + P_1 P_2}, \tag{3.5}$$

where

$$P_i = \frac{N_{i,\text{maj}} - N_{i,\text{min}}}{N_{i,\text{maj}} + N_{i,\text{min}}} \qquad (i = 1, 2) \tag{3.6}$$

is called the tunneling electron spin-polarization of the ferromagnets. One can easily verify from the equation that the JMR can vary over a wide range. For a vanishing polarization of one of the electrodes the magnetoresistance disappears, while for a full polarization of the tunneling electrons of both electrodes ($P_1 = P_2 = 1$) the effect will become infinitely large in Eq. (3.4), corresponding to a value of 1 (or 100%) in Eq. (3.5).

This simple model is successfully used to interpret the experiments, although the interpretation of the polarization term as a direct measure of the difference in the electron density of states at the Fermi level is still under debate. In recent calculations on JMR [51] a second, often ignored, contribution to the polarization has been put forward, which is due to the matching of the electron wave functions at the ferromagnet-insulator interface. To account for this complicating effect, the polarization in Eq. (3.4) is often referred to as an effective polarization P_{eff} and can experimentally be obtained from tunneling experiments with a superconductor as counter-electrode [49], as will be discussed in Chapter 10. One of the main focus points of the present and future research is related to the manipulation of this (spin dependent) interface matching term.

Since the pioneering (and never repeated) experiment of Julliere little progress has been made until the mid-nineties, when independent reports by Miyazaki et al. [17] and Moodera et al. [16] showed magnetoresistance ratios of about 20% at room temperature. The main obstacle was of technological nature: the fabrication of a good tunnel barrier. The requirements for this layer are severe. For example, the barrier thickness must be in the range of 2 nm or less, since the tunneling probability depends exponentially on the barrier thickness. Due to this exponential dependence, thickness variations should be limited, such as to prevent dielectric breakdown of the device due to current concentration at a single thin spot. Pinholes, i.e., spots of direct metallic

contact between both ferromagnets, are obviously fatal. Furthermore, the quality of the interfaces between barrier and ferromagnets determines the magnitude of the magnetoresistance effect. A dirty interface reduces the effect and may, e.g., result from less ideal (non-UHV) vacuum conditions between deposition of the ferromagnet and the barrier in order to change target material or mechanical masks. Finally, the barrier should be free of defect states, which could result in leakage current and thereby obscure the magnetoresistance effect.

Recently, a fabrication process has been developed by Moodera [16] which is rather successful. An Al_2O_3 barrier layer is deposited in a two step process. In the first step a thin metallic Al film is deposited. A metal is evaporated because metal-on-metal wetting is generally much better than insulator-on-metal wetting. A smooth, homogeneous, and completely covering Al layer is obtained by evaporation on cold substrates (cooled to reduce surface mobility) or by sputter-deposition (the higher deposition rate and random angle under which the atoms hit the surface reduce the need to cool the substrate). In the second step the metallic Al layer is oxidized in a reactive oxygen plasma to form Al_2O_3. Using this process, or variations thereupon, several groups have now been able to fabricate ferromagnet-insulator-ferromagnet tunnel junctions with magnetoresistance effects of over 40% at room temperature.

3.1   Preparation

A number of processes have been designed over the years to prepare a tunnel barrier between two metallic electrodes. One of the earliest reports of successful preparation of tunnel junctions was by Giaever and Megerle in 1961 [52], who prepared Al-oxide-metal junctions by the formation of a natural Al_2O_3 layer in an oxygen gas of atmospheric or reduced pressures. Proof of tunnel characteristics was given in the form of the bandgap of Al and several other superconducting materials. Although the method worked, a number of disadvantages were found for this oxidation scheme, e.g., irreproducible junction resistances. Shortly after, more reliable and cleaner methods were developed, among which plasma oxidation seemed very successful. The first results for plasma oxidized junctions were reported by Shapiro in 1963 [53] for Al-oxide-Sn junctions. However, the details of the fabrication process were unclear. Also in 1963, Miles and Smith [54] presented the first extensive results for plasma oxidized junctions.

The tunnel junctions for which the results are reported in this Thesis are also prepared by an *in-situ* dc plasma glow-discharge. A detailed description of this technique, and the preparation of tunnel magnetic tunnel junctions in general, can be found in [55]. It should be mentioned here, that there is no general recipe for the preparation of a good tunnel junction. Especially for glow-discharge prepared barriers, the optimum conditions vary widely from system to system and should be optimized for each glow-discharge configuration. The configuration used to prepare the junctions discussed here (located in the group of Dr. J. S. Moodera at the Massachusetts Institute of Technology) is home-built into a glass bell-jar vacuum system with a background pressure in the low 10^{-8} torr range after bake-out. An about 5 mm thick pure Al rod of approximate dimensions of 25 by 150 mm is used as a negative electrode, and is kept at a voltage of
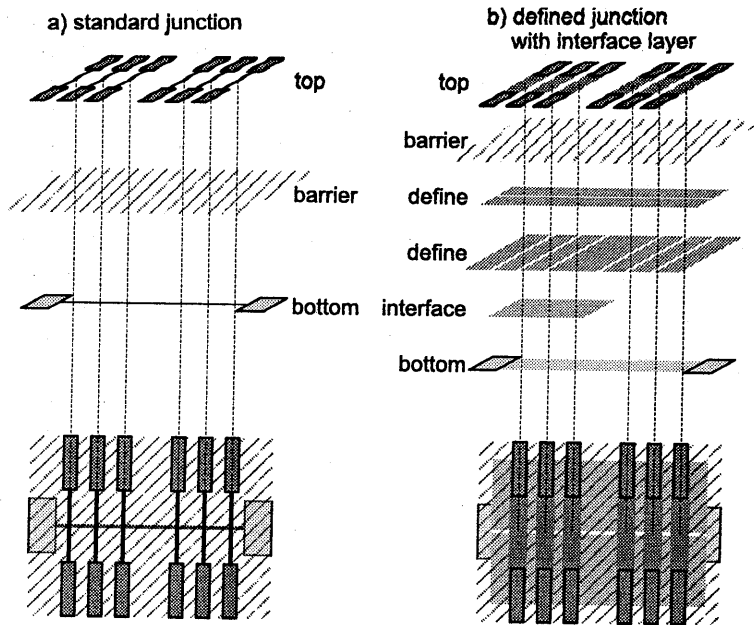
Figure 3.4: Examples of two processes to fabricate tunnel junctions, each showing one set of six junctions. The sequence of deposited materials starts with 'bottom,' and ends with 'top,' with top-views of the complete structures in the lowest panel. On a 2 × 2 inch substrate, 12 such sets can be prepared, using a total of 5 different masks (and without mask) and a sectored disk. (a) For a regular magnetic tunnel junction, with two magnetic electrodes separated by a insulating barrier (needing only two masks), and (b) for a tunnel junction with an additional interface layer and use of insulating defining masks (needing all five masks). The defining masks are used in combination with broad (~1 mm) electrode strips to avoid mask alignment problems. Through the defining masks, two relatively thick (4-8 nm) Al_2O_3 layers are deposited, covering the sides of the electrode strips, leaving a junction area comparable to the regular junctions uncovered. The areas enclosed by solid lines are used as contact pads.

about -1.8 kV with respect to two shields at a distance of about 30 mm above and below the rod. The direct line of sight between the sample substrate and the Al rod is blocked by a metallic shield mounted electrically floating with respect to the other parts. The function of this shield is to prevent the high energy ions generated near the negative electrode to damage the sample. The Al rod is mounted asymmetrically with respect to the sample holder, which results in a corresponding asymmetry in the glow-discharge conditions over the substrate. However, within each set of 6 junctions the preparation condition have been found to reproduce within about 10%, and the variation between the sets is gradual. Before each oxidation, the bell-jar is flushed several times with oxygen in order to flush the oxygen line. Before oxidation, an oxygen pressure of

$9 - 10 \times 10^{-3}$ Pa is established, after which the valve is closed. During oxidation, the oxygen pressure is manually maintained at the same pressure by adding additional oxygen when necessary. To oxidize 1.2 nm of Al, an optimal oxidation time has been established of about 110 sec. The current drawn by the plasma is about 330 mA.

One or two samples with an area of two by two square inch can be processed in a single day, each sample containing 12 sets of 6 junctions each, organized in 3 rows of 4 sets each. The stacking of the materials making up a junction can be varied over the substrate, where usually at least six nominally identical junctions are prepared for each junction. The substrates of choice are standard Corning glass slides, cleaned in a soap solution and degreased in alcohol vapor. Before the growth of the base layers, the substrates are cleaned *in-situ* by a oxygen glow discharge. The materials can thermally evaporated from three e-guns (typically Co), and a total of five resistive sources (typically W-boats are used for $Ni_{80}Fe_{20}$ and W-filaments for Al). During deposition, the thickness is monitored using a quartz crystal monitor. To improve surface flatness, the substrate can be cooled by a press-contact with a liquid nitrogen cooled Cu block (cold finger). The approximate temperature of the substrate during cooled deposition is 90 K.

The junctions are structured *in-situ* using metal contact masks, five of which can be used in the system in one run without breaking vacuum. A rotating sectored disk with open area rations of 1:2:3 can be used to vary the layer thickness across the substrate in three steps, each aligned with one row of four sets of junctions. With this flexible masking system, many variations can be produced on a single substrate, such that the preparation conditions are as equal as possible and the results may be directly compared. In Fig. 3.4 two variations of used tunnel junction geometries and their basic building blocks have been depicted. In Fig. 3.4(a) the process is shown for a regular junction, consisting of a bottom electrode, barrier layer, and a top electrode (adhesion and protection layers below and top have been omitted for clarity). Fig. 3.4(b) show the more complex process used to fabricate the junctions used in Chapter 9 with an additional layer at the interface between an electrode (in this case bottom). To avoid mask alignment problems, use is made of wider electrodes, which are subsequently partially covered using two crossed insulating defining layers, leave a junction area comparable to the regular junctions.

A cross-section HR-TEM image is shown in Fig. 3.5, showing the resulting growth of a typical layered stack with a Co bottom layer and a $Ni_{80}Fe_{20}$ top electrode. A 0.6 nm Cu interface layer is not visible due to the bad contrast between Co and Cu. As can been seen, the metallic electrodes are polycrystalline, with no apparent preferential growth direction. The Al_2O_3 layer, on the other hand, seems to be amorphous and rather good homogeneity.

3.2   Prospects for applications

The characteristics of magnetic tunnel junctions can be summarized briefly as a large electronic response to changes in the relative orientation of the magnetization directions, a relatively large resistance, and an intrinsic perpendicular device geometry. This combination of characteristics has attracted much interest from industry, where now two
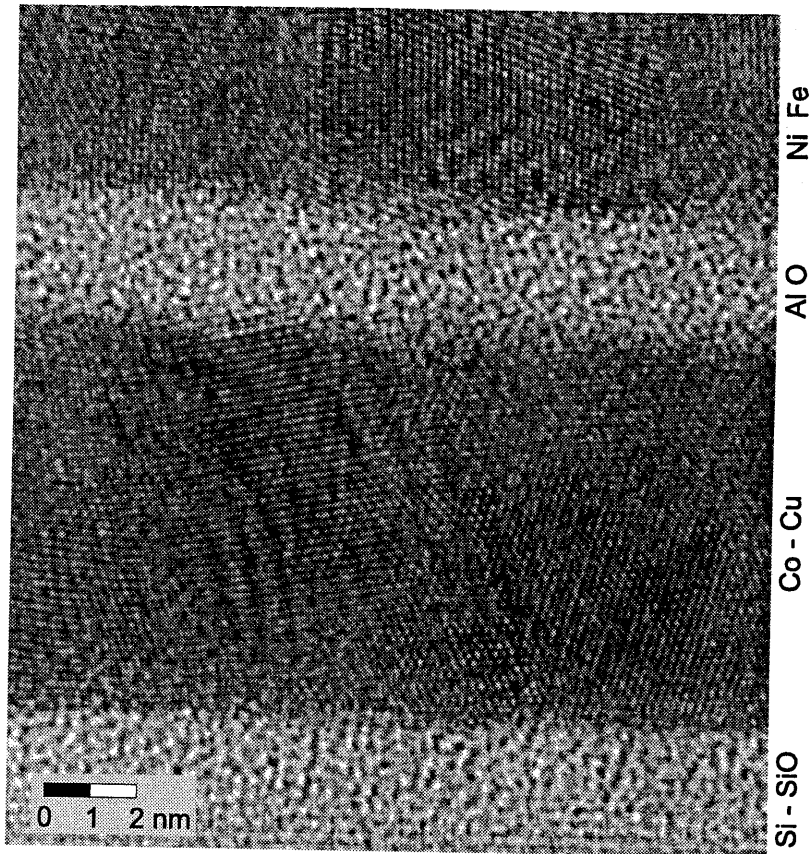
Figure 3.5: Cross-section high resolution transmission electron microscope (HR-TEM) photograph of a typical tunnel junction structure grown on a naturally oxidized and oxygen glow discharge cleaned Si(100) substrate (bottom). The structure buildup is 1 nm Si / 8 nm Co / 0.6 nm Cu / 1.4 nm Al (oxidized 100 seconds) / 10 nm $Ni_{80}Fe_{20}$ / 1.2 nm Al. The (dark) metallic Co/Cu (bottom) and $Ni_{80}Fe_{20}$ (top) layers grow in polycrystalline form without preferred orientation, while the (light) Al_2O_3 barrier layer seems to be amorphous. [Courtesy of A. Petford-Long and X. Portier, Univ. of Oxford, UK]

specific applications are actively being pursued. The first application is an extension of the classical metallic spin-valve GMR sensor presently used for magnetic hard-disk read-out. The larger magnetoresistance effect will make it possible to read smaller bits, and its larger resistance makes it easier to distinguish the resistance of the read-out element from the series resistance of the contact leads, which become increasingly more important as device sizes decrease. The principle design of a read-head based on a magnetic tunnel junction is depicted in Fig. 3.6.

The second application actively pursued is the magnetic random access memory,
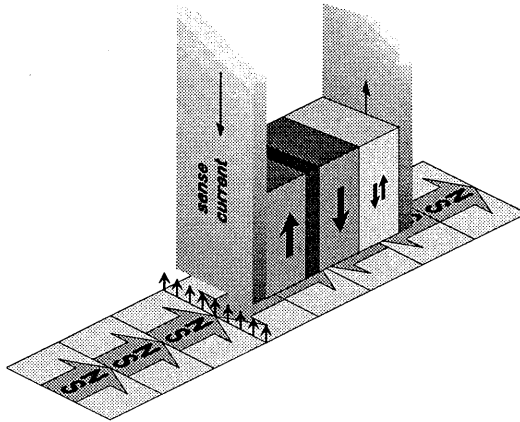
Figure 3.6: Example of an application of a magnetic tunnel junction for magnetic recording applications. The magnetization of one of the magnetic layers is 'pinned' by direct contact to an antiferromagnetic layer (indicated with ↑↓), while the magnetization of the other magnetic layer is 'free.' The magnetization of the free layer rotates to follow the magnetic flux emanating from the magnetic media. This rotation is monitored by measuring the resistance of the element, and is later converted to binary information.
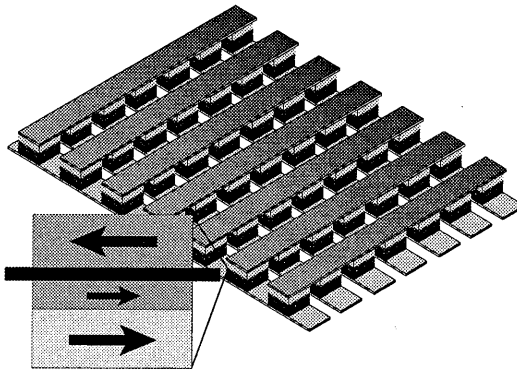
Figure 3.7: One possible design of a magnetic random access memory (MRAM) device, as proposed by IBM. Two perpendicular grids of lines make it possible to select an individual storage bit, located at each crossing. Each bit consists of a single magnetic tunnel junction. Such a junction can be optimized such that it can store information by setting the relative orientation of the magnetizations. For example, a parallel magnetization denotes a "1" and an anti-parallel orientation denotes a "0." The information will be contained after read-out and power shut-down, and may thus be called non-volatile. A diode is connected in series with each junction for the purpose of being able to uniquely sense the resistance of a single element.

for which one of the possible designs is shown in Fig. 3.7. The advantage of magnetic tunnel junctions over GMR or AMR based MRAM designs is in part located in the intrinsic perpendicular device geometry. This makes it possible to use a very high packing density. In comparison with DRAM and SRAM semiconductor memory cells, the advantages of the MRAM have to sought in the non-volatile operation, low power consumption, and radiation hardness of the magnetic tunnel devices.

Chapter 4

Interface Magnetism and Spin-Wave Scattering in Ferromagnet-Insulator-Ferromagnet Tunnel Junctions

Abstract:[*]

Careful tunneling studies in high quality $Co/Al_2O_3/Ni_{80}Fe_{20}$ junctions show a junction magnetoresistance (JMR) of 20.2% and 27.1% at 295 and 77 K, respectively, where the latter is in agreement with Julliere's model. The temperature dependence of the JMR can be explained by the temperature dependence of the interface magnetization. The decrease of the JMR with increasing bias voltage is intrinsic to ferromagnetic junctions. The strong disagreement with recent theories in the low bias voltage region can be attributed to magnetic excitations in these junctions, as seen in inelastic tunneling measurements.

4.1   Introduction

The spin-dependent tunneling between two ferromagnetic (FM) films across an insulator (I), successfully shown recently [16], has application potential in digital storage and magnetic sensor technologies [16, 18, 19, 56]. The magnitude of the junction magnetoresistance (JMR) at low temperatures nearly agrees with Julliere's simple model predictions [15]. This model is based on the difference in the density of states (DOS) for the two spin directions at E_F of the itinerant electrons in the FM [57], and earlier results of spin polarized tunneling between a FM and a superconductor [58].

The JMR exhibits both a temperature (T) and a bias voltage (V_{dc}) dependence [16]. These effects are surprisingly significant and depend on the quality of the junctions; the lower the JMR, the larger the temperature and the dc bias dependence. Earlier, others have reported a few percent JMR at liquid helium temperatures, whereas at room temperature it was only (0-2)%. Likewise, junctions showed a factor of 10 drop in JMR when V_{dc} was increased from 0 to 0.5 V [16, 59]. There are also cases where no JMR is observed at any temperature despite having a good tunnel barrier.

Recently, theories have been proposed [51, 60–65] to extend and make Julliere's model rigorous, in order to explain FM-I-FM tunneling and also some of the above observations. So far, they have not been very satisfactory. For example, a decrease in JMR with increasing bias voltage has been predicted [62, 63], but slower at low values of V_{dc} than seen experimentally.

In this Chapter, we present experimental observations that show the intrinsic behavior of the ferromagnetic tunnel junctions. Our dynamic conductance (G) and inelastic electron tunneling spectroscopy (IETS) results show unique features that provide an experimental basis for a theoretical understanding of both the temperature and the bias voltage dependence of the JMR.

4.2   Experimental

The tunnel junctions were prepared by cryogenic evaporation through shadow masks and glow discharge oxidation, as described in previous publications [16]. Out of the 72 junctions that were prepared, there were 12 junctions with $Co_{50}Fe_{50}$ or $Ni_{80}Fe_{20}$ as the top electrode for each barrier thickness (Al film thickness ranging from 0.4 to 1.8 nm). The bottom electrode was Co for all junctions. The measured junction resistances (R_J) were in the range of 1 to 30 kV depending on the junction type. The junctions showed a resistance increase of less than 20% upon cooling from room temperature down to 77 K and negligible below that, comparable to $Al/Al_2O_3/Al$ reference junctions. The junctions were temperature cyclable and stable in ambient atmospheres even after six months, displaying the same characteristics. The JMR (defined as the resistance change in a magnetic field relative to the peak value) ranged between (14-20)% at 295 K and (24-27)% at 77 K. The best junctions (showing the highest JMR at room temperature) were $Co/Al_2O_3/Ni_{80}Fe_{20}$ with 0.8 nm of Al [66]. Several of these junctions showed a room temperature JMR of 20%. One of these best junctions was selected for detailed studies and its characteristics will be discussed in the remainder of this Chapter. Similar
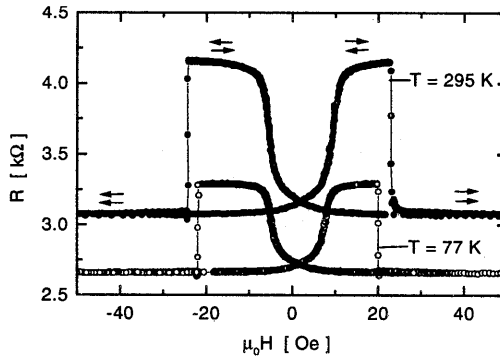
Figure 4.1: Resistance vs applied magnetic field for a $Co/Al_2O_3/Ni_{80}Fe_{20}$ junction at room temperature and 77 K showing JMR values $\Delta R/R_{AP} = 20.2\%$ and 27.1%, respectively. This measurement was done using an LR-700 ac resistance bridge with an excitation ac current at 100 nA. Arrows indicate the magnetization configuration of the two ferromagnetic layers according to Julliere's model [15,16].

features were seen for other good junctions as well.

4.3   Results

The current-voltage (I-V) characteristics for the junctions were measured from room temperature down to 1 K, both for parallel and antiparallel orientations (see the section on magnetoresistance). Tunnel current was higher for the parallel than for the antiparallel orientation at all temperatures, up to 0.8 V. The I-V data were fitted to Brinkman's formula [48]. The fitted average barrier height at 295 K (1 K) for parallel orientation was 3.34 (3.59) eV, in excellent agreement with that of similarly prepared $Al/Al_2O_3/Al$ reference junctions. The corresponding barrier asymmetry and thicknesses were 0.32 (1.24) eV and 1.22 (1.19) nm, respectively. A 0.8-nm-thick Al film, as used in the barrier formation, is expected to increase to a thickness of about 1.1 nm after oxidation [67]. The fitted barrier thickness is within 10% of the expected value, thus showing good barrier uniformity. This is further substantiated by atomic force microscope observation of Al_2O_3 covered Co films, showing an rms roughness of less than 0.5 nm. All of these qualities indicate that the optimum barrier with relatively clean FM interfaces is achieved. (Note that the tunneling current depends not only on the barrier properties, but also on the DOS of the electrodes and inelastic tunneling processes [68], which are not explicit in the tunneling theories. Hence, the barrier heights and the thicknesses given above are the "effective" values.)

The junction magnetoresistance curves at room temperature and 77 K are plotted in Fig. 4.1. They show hysteresis and a peak at low fields for either sign of the applied field. The peaks and valleys correspond to antiparallel and parallel orientations of the magnetizations (M) of the two FM electrodes, respectively [15]. The peak occurs in between the coercive fields of $Ni_{80}Fe_{20}$ (~5 Oe) and Co (~25 Oe) films. Nearly
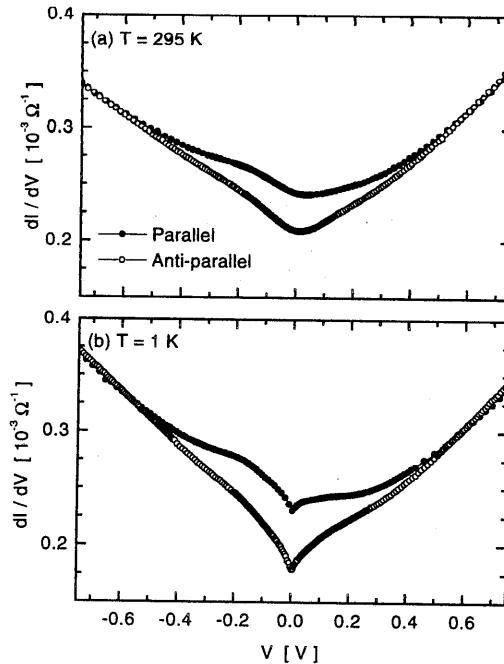
Figure 4.2: Dynamic conductance at two temperatures as a function of dc bias for parallel and antiparallel orientation of magnetizations for the same junction as in Fig. 4.1.

flat peaks indicate good antiparallel alignment of M, with the peak width increasing slightly with decreasing temperature. The JMR obtained from these data are 20.2% and 27.1% at room temperature and 77 K, respectively. Cooling the junction from 77 K down to 1 K caused only a marginal increase in R_J and the JMR stayed at 27.3%. The same trend was seen in all junctions, irrespective of the type of FM used.

Dynamic conductances measured at room temperature and 1 K for parallel (upper curve) and antiparallel (bottom curve) M configurations of the electrodes are shown in Fig. 4.2. The curves are asymmetric with respect to zero dc bias, the parallel configuration showing more asymmetry. G increases by less than a factor of 2 between 0 and 0.75 V, indicating a high barrier. Features can also be seen in these curves between 0 and 200 mV, more apparent in the parallel case. The curves sharpened near zero bias as T decreased, more for the antiparallel orientation. This behavior is similar to the zero bias anomaly usually seen with transition metal electrodes or with impurities in the barrier [68, 69]. However, in the present experiments, there were no changes in G between 4.2 and 1 K, unlike in the case with impurities or states in the tunnel barrier.

Fig. 4.3 shows the zero field IETS spectra, i.e., the derivative of G, measured at 295, 77, and 1 K in zero field. There was little difference in these curves when measured in an applied magnetic field up to 300 Oe. Looking at the room temperature data, one can see a broad peak (dip) at about ± 100 mV, slightly better defined upon cooling down
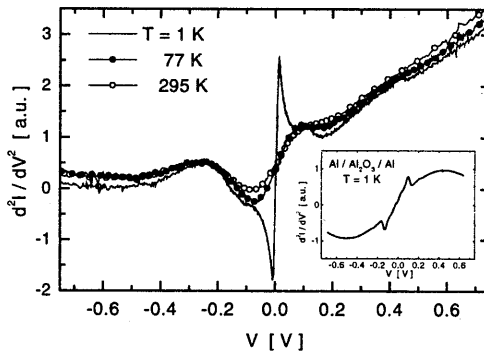
Figure 4.3: IETS spectra at three temperatures for the same junction as in Fig. 4.1, measured at $H = 0$. Similar spectra are seen for junctions where one electrode is a FM and the other electrode is Al. The inset shows an IETS spectrum of an Al/Al$_2$O$_3$/Al reference junction for comparison. Note that the features for all Al junctions were only seen at liquid He temperatures.

to 77 K. At 4.2 K, in addition to this peak, a sharp feature appears at 17 mV, with no change occurring between 4.2 and 1 K. Finally, a small peak at 450 mV is sometimes observed. These spectroscopic features were seen in other junctions where one of the films was ferromagnetic, such as Al/Al$_2$O$_3$/Co, as one can expect.

For comparison, the IETS spectrum for a Al/Al$_2$O$_3$/Al reference junction taken at 1 K is shown in an inset in Fig. 4.3. The peak at ~110 mV in the IETS spectra for Al/Al$_2$O$_3$/Al junctions, seen only at liquid helium temperatures, has been identified by others as due to an Al–O stretching mode [19]. The small peak sometimes visible at 450 mV has been attributed to a surface O–H$^-$ stretching mode [19]. In the IETS spectra for ferromagnetic junctions, the peak at 450 meV due to the surface O–H$^-$ stretching mode is barely visible at low temperatures. The broad peak around 100 mV is not the same as in reference junctions, in that it is also seen at room temperature. Hence, this peak is not due to the Al–O stretching mode alone. Tsui *et al.* [70] have observed a magnon peak in IETS spectra of NiO at 107 meV. Therefore, part of the peak seen in Fig. 4.3 at about 100 mV and also the sharp peak at 17 mV can be interpreted as due to magnons generated in the FM electrodes.

The bias voltage dependencies of the JMR at 295, 77, and 1 K are shown in Fig. 4.4 for both polarities of V_{dc} (defined with respect to the Co electrode). A slight dependence on the polarity is observed. As previously reported by us [16], and by others [18,19,59], the JMR decreased monotonically as V_{dc} increases, in the present case by 60% at 0.5 V. Earlier, the corresponding drop in JMR was at least a factor of 10 for "unoptimized" junctions [16,59]. Present good junctions show great improvement. The normalized data shown in Fig. 4.4(b) is nearly independent of temperature, even near zero bias voltage, where G shows the anomaly at low temperatures.

According to the calculations of Bratkovsky [62] and Zhang *et al.* [63], the bias voltage dependence of JMR arises from the influence of the applied electric field on the barrier shape. Increasing V_{dc} increases the overall conductance and, hence, decreases
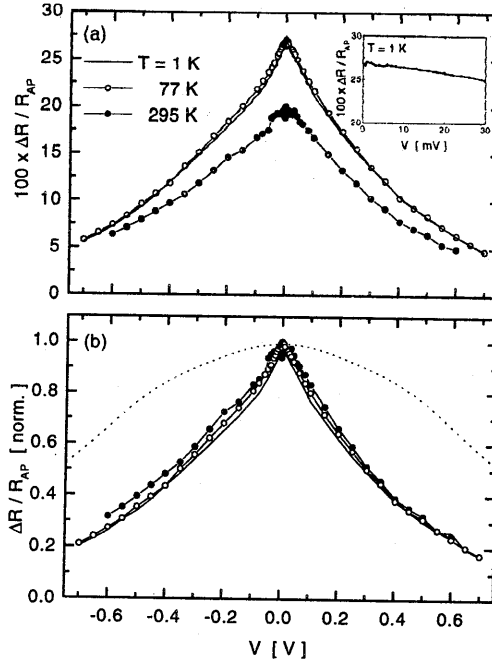
Figure 4.4: JMR vs bias voltage at three temperatures for the same junction as in Fig. 4.1. Data shown are (a) the actual percentages and (b) normalized at zero bias voltage. The inset shows the JMR in the low bias voltage region displaying near constancy of JMR. The dashed line in (b) is the theoretically expected variation for a Fe/Al$_2$O$_3$/Fe junction with a 3 eV barrier height (from Fig. 1 in Ref. [62]).

the JMR ratio. The dashed line in Fig. 4.4(b) is according to Bratkovsky (from Fig. 1 in Ref. [62]). The calculated JMR falls much slower than the experiment, especially at low bias voltage. A bigger decrease in the JMR vs V_{dc} was observed for MgO barriers whose barrier height was in the range of 1 eV (as in the calculation of Zhang *et al.* [63]). Thus, it is important for applications to have a high tunnel barrier.

We propose that part of the large decrease in JMR can be attributed to the excitation of magnons, thereby randomizing the tunneling electron spins and increasing the total conductance. (The energy dependence of the spin polarization due to band structure effects may also reduce the JMR at high bias.) The peaks at 17 and 100 mV in the IETS spectra support this interpretation. In fact, there was little dependence of JMR on V_{dc} below about 15 mV, as shown by the data at 1 K [see inset in Fig. 4.4(a)]. This suggests a possible gap of this order in the magnon spectra.

For a FM$_1$-I-FM$_2$ tunnel junction, Julliere's model [15], based on Stearns's theory [57], gives JMR= $2P_1P_2/(1 + P_1P_2)$, where P_1 and P_2 are the tunneling electron spin-polarizations measured by tunneling with a superconductor counter electrode as a spin detector [58]. These latter measurements, performed at 0.4 K and near the Fermi level, yielded $P_{Co} = 35\%$ and $P_{Ni_{80}Fe_{20}} = 45\%$. These give an expected JMR of 27.2%

for a $Co/Al_2O_3/Ni_{80}Fe_{20}$ junction, in perfect agreement with the measured values at 77 and 1 K. However, at 295 K, a JMR of only 20.2% is observed.

From spin wave theory [71] and experimental observations [72–75], on clean surfaces in systems such as $FeNiB_{0.5}$, $Ni_{80}Fe_{20}$, and Fe, it is known that the interface magnetization $[M_i(T)]$ follows a Bloch $T^{3/2}$ temperature dependence: $M_i(T) = M_i(0)[1 - \alpha_i T^{3/2}]$. Values of α_i up to twice or more the bulk value have been reported, depending on the interface cleanliness. In the above ferromagnets, about 15% (or higher for a contaminated interface) decrease in M_i has been observed as T increases from 77 to 300 K, with only $\sim$ 2% or less change below 77 K. Also, the spin polarization $P(T)$ has been shown to be proportional to M_i.

Tunneling electrons come from the top one to two monolayers of the FM and, hence, should reflect interface properties. This has been shown in a series of spin polarized tunneling experiments involving ultrathin FM films near the barrier and a superconducting spin detector [58]. The polarization of these tunneling electrons is, thus, expected to follow the temperature dependence of the interface magnetization. Assuming the polarization to follow a $T^{3/2}$ dependence and Julliere's model, and choosing values for α_i such that it reproduces the ratio of the experimental conductance difference (between parallel and antiparallel configuration) at 77 and 295 K, the JMR ratio at room temperature can be evaluated. This yields an estimate for the JMR value at room temperature of 22.8%, which is in fair agreement with our experimental value of 20.2%. Below 77 K, both M_s and JMR do not change significantly. The lower value of JMR at higher T can thus be attributed to the temperature dependence of the interface magnetization of the FM films. A more detailed discussion of the temperature dependence of the JMR can be found in Chapter 6.

The data published for $NiFeB_{0.5}$ and thin films of $Ni_{80}Fe_{20}$, with even a small amount of interface contamination [72–75], show a stronger temperature dependence and reduced magnitude of M_s (with T_C below room temperature for $Ni_{80}Fe_{20}$). This might explain the irreproducible, low, or absent JMR at room temperature in many of the reports in the literature, whereas cooling these junctions down to low temperatures sometimes restores the JMR to nearly its expected value [59,76].

In addition to P, the factors that influence the JMR value are the following: (i) the FM/I interface cleanliness, (ii) the barrier quality, and (iii) well defined and separated H_c of the FM electrodes. It is nontrivial to completely oxidize the barrier Al film without oxidizing the FM interface of the bottom FM and also achieve a clean FM/I interface, to reach the full JMR value. Oxidation of the interface near the barrier can affect the JMR by spin scattering due to the strong paramagnetic nature of the magnetic transition metal oxides at higher temperatures. At low temperatures, in the antiferromagnetically ordered state of these oxides, the spin scattering is negligible [77], thus showing a finite JMR in many cases, see also Chapter 8. Also, impurities in the barrier are detrimental to the JMR [62,78].

4.4 Conclusions

In conclusion, detailed tunneling studies as a function of temperature and bias voltage in well-characterized, good junctions reveal some of the fundamental phenomena in FM-I-FM tunnel junctions. The temperature dependence of JMR has been attributed to the temperature dependence of the interface magnetization of the FM electrodes, also explaining the failure to observe JMR at room temperature in many earlier reports. The dc bias dependence of JMR does not agree with recent theories, especially in the low bias voltage region where magnetic excitations play a role, as shown by the inelastic tunneling spectra.

Chapter 5

Current Distribution Effects in Magnetoresistive Tunnel Junctions

Abstract:[*]

The influence of an inhomogeneous current density on the (magneto)resistance of a ferromagnet-insulator-ferromagnet tunnel junction in the cross-strip geometry is analyzed using a finite element approach. The four-probe resistance is smaller than the actual resistance for electrode resistances (in the junction area) comparable to or higher than the junction resistance. Even negative four-probe resistances can be obtained. The apparent resistance change due to the junction magnetoresistive effect also decreases, but always remains positive. This results in unrealistically large apparent magnetoresistance ratios which can even approach infinity, which explains some recent experiments.

5.1   Introduction

Tunnel junctions consisting of two ferromagnetic layers separated by a thin insulating layer show large magnetoresistive effects when the magnetizations of the ferromagnetic layers change their relative orientation from parallel to antiparallel in an applied magnetic field [16,17,79]. This result has attracted considerable attention due to its potential applicability in low power magnetic field sensors or nonvolatile memory devices. The largest magnetoresistive effects have been observed in low resistance junctions (compared to the lead resistance in the same area). Low resistances can in some cases be explained by a large surface area (i.e., scaling effect) or by a low tunnel resistivity (i.e., barrier property). Moodera *et al.* [79] observed that by reducing the barrier resistivity the magnetoresistance ratio, defined as the resistance change divided by the resistance in a reference state, increased to significantly higher values for otherwise identical junctions. This was qualitatively attributed to the measuring geometry artifact described here. Similarly, Kumagai *et al.* [80,81] observed that for microfabricated junctions the magnetoresistance ratio is smaller than for similar macroscopic junctions [17].

Most results up to now are obtained with the tunnel junctions in the cross-strip geometry, shown schematically in Fig. 5.1. Two (ferromagnetic) electrodes are configured perpendicular to each other and are separated by an insulating layer; the intersection defines the junction area. The four-probe resistance is measured by sending a current using one of the facing contacts on each electrode and measuring the voltage difference between the other two. Resistance measurements in similar geometries [82–84] are known to cause problems due to inhomogeneous current distribution effects when the electrode resistances (in the same area) become comparable to the perpendicular resistance. The four-probe resistance appears to be lower than expected, and even negative resistances have been found. Qualitatively explanations have been proposed [82–85] based on one dimensional (1D) analytical models taking into account the electrode resistances. However, to the best of our knowledge no analytical solutions exist for the current distribution in the cross-strip geometry. Also the effect on magnetoresistive properties is not accounted for in previous models. Therefore, we performed finite element calculations taking into account the whole geometry.

5.2   Modeling

In order to calculate the four-probe resistance, we model the junction by two perpendicular stripes extending some distance outside the junction area (see Fig. 5.1). Perpendicular current flow within the electrodes is neglected. The current distribution within the bottom electrode is governed by Ohm's law:

$$\mathbf{J}_b = -\rho_b^{-1}\,\nabla V_b, \tag{5.1}$$

where $\mathbf{J}_b$ is the local in-plane current density, ρ_b the resistivity, and V_b the local voltage in the bottom electrode. From current conservation we find:

$$d_b\,\nabla \cdot \mathbf{J}_b + j_{\text{tun}} = 0, \tag{5.2}$$
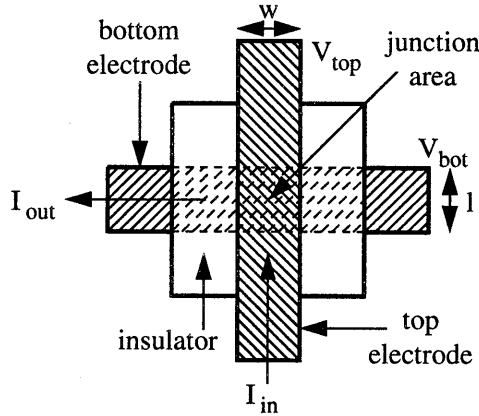
Figure 5.1: Schematic of the cross-strip geometry. The junction area is defined as the intersection of the two perpendicular electrodes (hatched), which are separated by a thin insulating layer.

where d_b is the thickness of the bottom electrode, and j_{tun} is the local tunnel current density. Similar equations hold for the top electrode. The tunnel current is modelled as:

$$j_{tun} = \rho_j^{-1}\left(V_b - V_t\right),\qquad(5.3)$$

where ρ_j is the tunnel resistivity in Ωm^2, which in general depends on the voltage difference between top and bottom electrode. In the present case, we restrict the calculations to the linear (low voltage) regime, although the inclusion of nonlinear effects is straightforward.

By substituting these equations we find two coupled equations for the voltage distributions in the top and bottom electrodes:

$$\frac{\partial^2 V_{b(t)}}{\partial x^2} + \frac{\partial^2 V_{b(t)}}{\partial y^2} = \frac{R_{\square,b(t)}}{\rho_j}\left(V_{b(t)} - V_{t(b)}\right),\qquad(5.4)$$

where $R_{\square,b(t)} = \rho_{b(t)}/d_{b(t)}$ is the square resistance of the bottom (top) electrode. The only free parameter in this equation is the ratio between the square resistance of the electrodes and the tunnel resistivity. This parameter can be written as:

$$\frac{\rho_j}{R_{\square,b(t)}} = l_{typ}^2 = \frac{R_j}{R_{b(t)}}w^2(l^2),\qquad(5.5)$$

where l_{typ} is the typical length scale of the current distribution, R_j and $R_{b(t)}$ are the expected resistances of the junction and the electrodes (within the junction area), respectively, for a junction area with length l and width w. When the typical length scale $l_{typ} < l$, w or, alternatively, when the junction resistance $R_j < R_{b(t)}$, the current density distribution will become inhomogeneous.
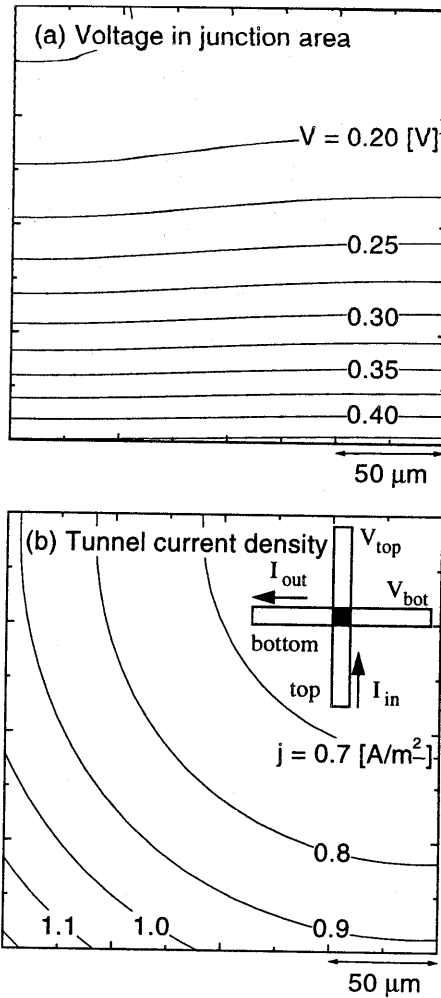
Figure 5.2: (a) The calculated voltage distribution in the top electrode for a junction with $l_{typ}(= l, w) = 200~\mu$m ($R_j = R_{b(t)} = 20~\Omega$). (b) The tunnel current density distribution shows an increased current density in the corner where the current leads meet. Only the junction area is shown.

A finite element approach is used to solve Eq. (5.4). As boundary conditions a voltage of ± 1 V at the end of each of the current leads is used. An example of the calculated potential and tunnel current density distributions within the junction area are shown in Fig. 5.2. Both leads have a square resistance of $R_\square = 20~\Omega$, the junction area is a square with 200 μm sides, and the tunnel resistivity ρ_j is chosen such that the actual junction resistance equals the resistance of the electrodes. The voltage distribution for the bottom electrode is not shown for this symmetric junction. As can be seen the
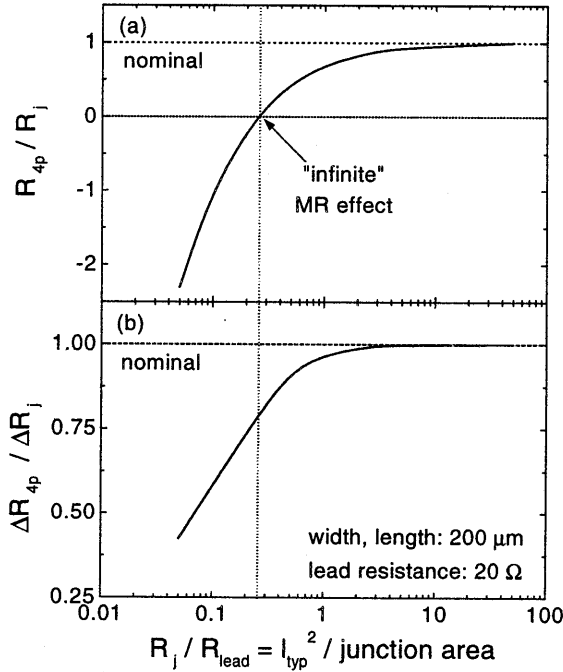
Figure 5.3: The calculated (a) scaled four-probe resistance R_{4p}/R_j and (b) scaled resistance change $\Delta R_{4p}/\Delta R_j$ for a junction with $l, w = 200~\mu$m, $R_{b(t)} = 20~\Omega$, with varying ρ_j.

in-plane voltage drop within the junction area is significant and as a result the tunnel current is largest in the corner where both current leads meet (i.e., the current takes the shortest path). Since the voltages are measured at the other sides, the apparent junction resistance is smaller than the actual junction resistance.

The four-probe resistance R_{4p} can be calculated similar to the experiment by dividing the voltage difference in the voltage leads by the total tunnel current. In Fig. 5.3 R_{4p} and ΔR_{4p} due to a small magnetoresistive change in the tunnel resistivity are shown for varying ρ_j. Both quantities are scaled to the actual values for the junction resistance R_j and junction resistance change ΔR_j. As shown in Fig. 5.3(a), a considerable reduction of the scaled four-probe resistance occurs for $R_j < R_{b(t)}$ or, alternatively, for $l_{typ} < l, w$. Also the scaled four-probe resistance change shows a reduction, as shown in Fig. 5.3(b). However, its value always remains positive. This can be understood when this quantity is viewed as a (scaled) derivative with respect to R_j of the four-probe resistance, which shows a monotonic behavior. Combined, these effects lead to an infinite apparent magnetoresistance ratio at the point where the apparent junction resistance in the reference state approaches zero.

5.3   Discussion and Conclusions

Using the approach described above, the experiments reported in Refs. [17] and [79] have been reinterpreted by modeling the four-probe resistances in the parallel and antiparallel states, using only the tunnel resistivity as a parameter. For the $10 \ \Omega$ junction in Fig. 2(a) of Ref. [79], a corrected magnetoresistance ratio of 19% is found (relative to the high resistance state) instead of the 30% obtained from the measurement. The corrected value is consistent with the values obtained for high resistance junctions [16, 79, 86]. For the junction with the negative resistance of Fig. 2(c) of Ref. [79] a corrected value of 15% is found, compared to the observed value of over a thousand percent (relative to the high resistance state). Also for this junction the corrected value is more in line with the results obtained for higher resistance junctions [16, 79, 86].

Similarly, for the data presented in Fig. 1 of Ref. [17] for a $1 \ mm^2$ area tunnel junction with a $7 \ m\Omega$ resistance we find a corrected magnetoresistance ratio of 1.2%, much reduced from the measured 18% (relative to the low resistance state). Recently, new measurements have been presented by this group on microfabricated tunnel junctions (where $l_{typ} > l, w$) with magnetoresistance ratios of a few tenths of a percent [80, 81]. Also in this case the corrected value is more in line with the data for junctions without the inhomogeneous current distribution effect (in this case by reducing the area).

In conclusion, we would like to state that care should be taken when comparing experimentally obtained data on magnetoresistive tunnel junctions. The measurements for low resistance junctions should be corrected for inhomogeneous current distribution effects. It should be noted that the apparent enhancement of the magnetoresistance ratio does not lead to increased application potential, since the actual resistance change (and hence the signal) is reduced. The inhomogeneous current distribution effects occur for junctions with resistances of the electrodes (in the junction area) comparable or higher than the junction resistance or, similarly, when the typical length scale of the effect becomes smaller than the junction dimensions. Problems can be avoided by increasing the tunnel resistivity, decreasing the junction dimensions, or lowering the electrode resistances by adding well conducting layers.

Chapter 6

Temperature Dependence of Tunnel Magnetoresistance

6.1 Introduction

Most theoretical explanations to date of the magnetoresistance of magnetic tunnel junctions are based on model calculations performed for zero temperature and in the limit of zero bias voltage. Under these conditions, only elastic conduction processes need to be included, in which both the energy and the spin of the conduction electrons are conserved. The conductance can then be calculated by summation of the individual conductance contributions of all incident electrons. Because only elastic tunneling contributions are considered, each incoming electron state has a single corresponding transmitted electron state. Also only the electrons with energies at the Fermi level will contribute to the tunnel current, since only for those electrons empty states are available in the counter electrode to tunnel into. Thus, the number of available states for each incident electron to tunnel into is restricted, while also the number of electrons contributing to the conduction is limited.

At elevated temperatures or at non-zero bias voltages, however, these assumptions may not be completely valid. The obvious effect of the increase of the temperature will be a change in the occupation of the electron states in the energy range of a few kT around the Fermi level, which is determined by Boltzmann statistics. The obvious effect of a non-zero bias voltage is a change of the form of the barrier and a change of the kinetic energy of the transmitted electron compared to that of the incident electron. These obvious effects have been modeled within the framework of the elastic tunnel theory in the sixties [47, 48].

In addition to the above-mentioned Fermi-distribution effect on the temperature dependence of the JMR, there is another effect, related to the decrease of the magnetization of the electrodes. As proposed by Moodera et al. [87] and Shang et al. [88], this leads to a decrease of the effective tunneling electron spin polarization of the electrodes, as defined in Eq. (3.4), and hence to a reduction of the JMR ratio.

Thirdly, at finite temperatures inelastic tunneling processes become possible, for which the initial and final energy of the tunneling electrons are not equal. The energy difference is released by excitation of phonons (lattice vibrations) and/or magnons (spin-waves), or gained by their absorption. As phonon excitations conserve spin, the resulting additional conductance will not have a large influence on the junction magnetoresistance. Magnon excitation or absorption, on the other hand, leads to spin-flip and thereby reduces the JMR. As a result of the additional degree of freedom offered by the excess energy, the number of final states available for electrons to tunnel into increases. These inelastic conductance contributions can visualized by spectroscopic measurement of the tunnel conductance, called Inelastic Electron Tunneling Spectroscopy (IETS), as will be described in more detail in Chapter 7.

In this Chapter, two recent models are presented within which these effects on the temperature dependence of the (magneto)-resistance of tunnel junctions are described. Both will be compared to experimental data. In Section 6.2, a phenomenical model is presented is based on spin-wave excitations in the electrode, desturbing the alignment of the magnetizations [87, 88]. A method is described to separate the effect of temperature into a magnetic and a nonmagnetic contribution, which is equally applicable to nonmagnetic junctions. The model presented in Section 6.3 uses a Transfer Hamiltonian calculation of the inelastic tunnel conductance contribution resulting from the absorption or emission of spin-waves during the tunnel process at elevated temperatures [89]. This model makes predictions of both the bias voltage as well as the temperature dependence of the magnetoresistance, but since it is based on spin-wave excitations, is not applicable to nonmagnetic tunnel junctions.

Special for the case of magnetic tunnel junctions in comparison to nonmagnetic tunnel junctions is that apart from the evolution of the conductance as a function of temperature, additional information can be obtained from the magnetoresistance effect.

Note that the presented list of candidates for the explanation of the temperature dependence is not complete. Of the other candidates, the temperature dependence of the dielectric constant of the barrier material is briefly mentioned. The value of the dielectric constant determines the amount of mirror charges created in an insulator when it is in direct contact with a metal. These mirror charges influence the potential energy landscape of the tunnel barrier, which in turn is important for the junction magnetoresistance.

6.2   Spin-wave excitations in the electrodes

For a typical junction, the temperature dependence is first analysed following a model proposed by Moodera et al. [87] and in more detail by Shang et al. [88]. The conductance G of a tunnel junction is assumed to consist of two independent conduction channels: a contribution G_d due to direct tunneling and a contribution G_i due to indirect tunneling (for instance, tunneling via defect states in the oxide layer). The latter contribution is assumed to be phonon-assisted (inelastic), and is therefore absent at $T = 0$ K. It is assumed that *only* the direct contribution depends on the angle θ between

the magnetic moments of the two electrodes [51]. Thus, the conductance is written as:

$$G(\theta) = G_e(\theta) + G_i, \qquad (6.1)$$

with

$$G_d(\theta) = G_T \times (1 + P_1 P_2 \cos\theta), \qquad (6.2)$$

where $P_{1,2}$ is the effective tunneling electron spin-polarization and the prefactor G_T is the average direct elastic conductance for parallel and antiparallel alignment of the electrode magnetizations. All the variables in Eqs. (6.1) and (6.2) depend on temperature and are discussed separately below.

Firstly, the well documented temperature dependence of the average direct elastic tunneling conductance G_T is discussed. The electrons responsible for the tunnel current originate from an energy interval of the order of kT/e wide, centered around the Fermi-level. At elevated temperatures, the width of this interval increases, and thus electrons levels at higher energy become occupied. Due to the exponential dependence of the tunnel probability on energy, these "hot" electrons contribute more to the tunnel current. The relative increase of the tunnel conductance with increasing temperature has been calculated by Simmons [47]:

$$\frac{G_T(T)}{G_0} = \frac{CT}{\sin CT}, \qquad (6.3)$$

where $G_0 = G_T(0)$ is the conductance at zero temperature and the constant C is given by $C = 1.387 \times 10^{-4} d/\overline{\phi}^{1/2}$, with the barrier width d in Å and the average barrier height $\overline{\phi}$ in eV. For typical barrier parameters ($\overline{\phi} = 2.0\,\text{eV}$ and $d = 15\,\text{Å}$) G_T increases by 3.3% between 0 K and room temperature. This is much less than the ordinarily experimental observed 20-25% (also for non-magnetic junctions). Therefore, even for non-magnetic tunnel junctions, other (inelastic) conductance contributions need to be considered. However, at sufficiently low temperatures, the inelastic tunnel contributions are small and only the elastic contribution prevails. Thus, the barrier parameters obtained from fits to I-V measurements at low temperatures can be used to predict $G_T(T)$ at elevated temperatures.

The second factor in the right hand side of Eq. (6.2) depends on temperature via the product $P_1 P_2 \cos\theta$. Pierce *et al.* [72] have found that the polarization of secondary electrons in a photo-excitation experiment follows the temperature dependence of the interface magnetization M_i. Furthermore, the temperature dependence of the (bulk) magnetization can be understood by considering magnon (also called spin-wave) excitations at elevated temperatures, see for instance Chapter 15 in [90] or Chapter 33 in [91]. The predicted dependence (in the temperature regime of interest) is the Bloch $T^{3/2}$ law, i.e., $M_{i,b}(T) = M_{i,b}(0)[1 - \alpha_{i,b}T^{3/2}]$. This dependence has also been found to hold for surfaces [71–73, 92, 93], although the proportionality constant $\alpha_{i,b}$, describing the magnitude of the decrease of magnetization, is usually larger by a factor of two or more for the interface (i) of a thin film compared to the bulk (b) value, i.e., $\alpha_i \geq 2\alpha_b$.

The difference is caused by a change in the number and strength of the magnetic exchange interactions for atoms near an interface. Using these results, Shang *et al.* [88] proceed by writing the polarization of the tunnel electrons as:

$$P(T) = P(0) \left[1 - \alpha_i T^{3/2} \right], \tag{6.4}$$

where the value $P(0)$ can be measured at low temperatures using the Spin Polarized Tunneling experiment (see Chapter 10). Using Eq. (6.4), the product can be rewritten as:

$$P_1(T) P_2(T) \cos\theta = P_1(0) P_2(0) \left[1 - \alpha_{i,1} T^{3/2} \right] \left[1 - \alpha_{i,2} T^{3/2} \right] \cos\theta \tag{6.5}$$

For a more general interpretation of the factor $P_1 P_2 \cos\theta$, the original definition needs to be considered. The $\cos\theta$ results from a spinor transformation introduced by Slonczewski [51] to account for the change of the spin quantization axis for electrons transfering between two layers with non-colinear magnetic moments. Thus, the product can be written as:

$$P_1 P_2 \cos\theta = \frac{P_1 \, \boldsymbol{M}_{i,1} \cdot P_2 \, \boldsymbol{M}_{i,2}}{| \, \boldsymbol{M}_{i,1} | \, | \, \boldsymbol{M}_{i,2} |}, \tag{6.6}$$

where $P_{1,2}$ are constant scalar parameters, independent of temperature, as long as short range ferromagnetic order exists. $\boldsymbol{M}_{i,1}$ and $\boldsymbol{M}_{i,2}$ fluctuate as a results of thermal excitations. At elevated temperatures, due to magnon excitations, the dot product in Eq. (6.6) needs to be replaced by the average $\langle \boldsymbol{M}_{i,1} \cdot \boldsymbol{M}_{i,2} \rangle \propto \langle \cos\theta \rangle$. Due to the randomness introduced by thermally excited spin-waves, the extremal values of the dot product are not obtained over the whole interface area of the sample at the same time (this is what also causes the global magnetic (interface) moment to decrease, while all individual moments remain the same). When the magnon excitations are independent for the two magnetic layers, the extremal values for $\langle \cos\theta \rangle$ are (for $\langle \phi \rangle = 0$ or π):

$$\langle \cos\theta \rangle_{\mathrm{P,AP}} = \pm \frac{\langle \boldsymbol{M}_{i,1} \rangle}{| \, \boldsymbol{M}_{i,1} |} \frac{\langle \boldsymbol{M}_{i,2} \rangle}{| \, \boldsymbol{M}_{i,2} |} = \left[1 - \alpha_{i,1} T^{3/2} \right] \left[1 - \alpha_{i,2} T^{3/2} \right], \tag{6.7}$$

which is mathematically equivalent to Shang *et al.* [88]. However, in a situation where interface spin-waves are coupled across the barrier, a lower reduction would be predicted.

Independently, but along similar lines of reasoning MacDonald *et al.* [94] proposed the concept of shadow-bands. Shadow bands are the mingling of the majority and minority spin-densities of states due to magnetic disorder and effectively reduce the polarization the same way as proposed by Shang *et al.* [88].

The third contribution to the temperature dependence is the spin-independent indirect (inelastic) conductance G_i in Eq. (6.1). This contribution is assumed to be thermally activated and therefore negligible at low temperatures; this assumption makes it possible to separate the direct and indirect contributions using the experimental data,
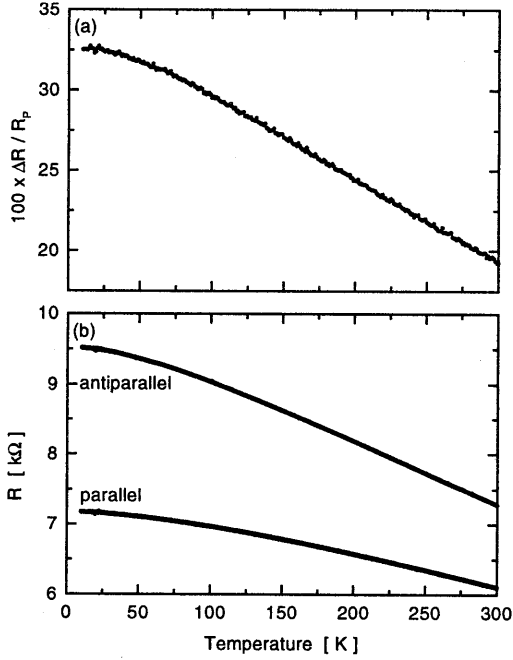
Figure 6.1: (a) Resistance and (b) magnetoresistance for a $Co/Al_2O_3/Ni_{80}Fe_{20}$ junction as a function of temperature. The symbols are the measured values, the solid lines are the result of the analysis as discussed in the text. For the temperature dependence of $G_T(T)$ use is made of Eq. (6.3) with barrier parameters $\phi = 3.4$ eV and $s = 0.94$ nm.

using:

$$G_P(T) - G_{AP}(T) = 2G_T(T)P_1P_2\left[1 - \alpha_{i,1}T^{3/2}\right]\left[1 - \alpha_{i,2}T^{3/2}\right]$$

$$= 2G_T(T)P_1P_2\left[1 - \left(\alpha_{i,1} + \alpha_{i,2}\right)T^{3/2} + \alpha_{i,1}\alpha_{i,2}T^3\right] \quad (6.8)$$

$$G_P(T) + G_{AP}(T) = 2\left[G_T(T) + G_i(T)\right], \quad (6.9)$$

where P and AP denote magnetization configurations in which $\langle\cos\theta\rangle = 1$ and -1, respectively. As G_i is thermally induced, $G_i(T = 0) = 0$, thus $G_T(0)$ can be determined from Eq. (6.9) and low temperature data. At elevated temperatures, $G_T(T)$ can be obtained using Eq. (6.3) and the barrier parameters found from fits to the low temperature J-V data. The indirect conductance $G_i(T)$ is subsequently obtained using Eq. (6.9) and subtracting the extrapolated values for $G_T(T)$. Also from the low temperature data the product $P_1(0)P_2(0)$ is obtained using Eq. (6.8) and the value $G_T(0)$. The values for $\alpha_{i,1}$ and $\alpha_{i,2}$ are obtained from a fit of the experimental data to Eq. (6.8).

In Fig. 6.1 the temperature dependence of the resistance and magnetoresistance is shown for a $Co/Al_2O_3/Ni_{80}Fe_{20}$ junction. The magnetoresistance $\Delta R/R(P)$ decreases from 33% at $T = 10$ K to 19% at room temperature, a reduction of 40%. The corresponding reduction of the resistance is 15% (23%) for parallel (antiparallel) aligned
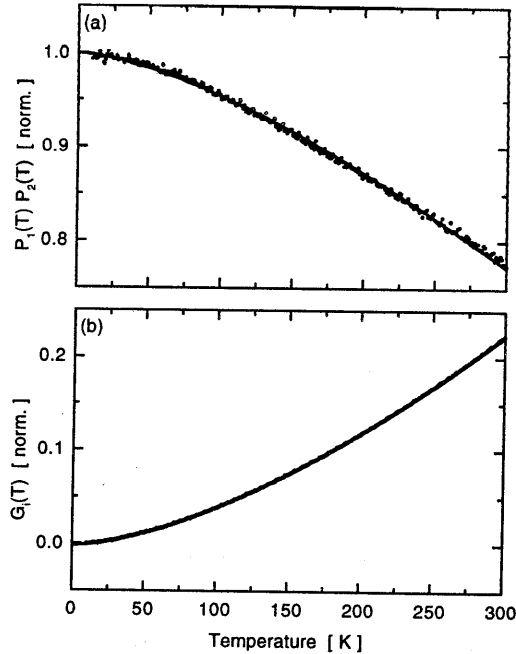
Figure 6.2: Analysis of the resistance and magnetoresistance data of Fig. 6.1. (a) Product $P_1(T)P_2(T) = \Delta G(T)/\Delta G(0) \times G_T(0)/G_T(T)$ and (b) normalized inelastic tunnel conductance $G_i(T) = [\langle G(T)\rangle - G_T(T)]/G_T(0)$. The symbols are the derived from the measured data, the solid lines are the result of the analysis as discussed in the text. For the temperature dependence of $G_T(T)$ use is made of Eq. (6.3) with barrier parameters $\phi = 3.4\,\text{eV}$ and $s = 0.94\,\text{nm}$.

magnetizations. These numbers are typical for "good" tunnel junctions, i.e., having a magnetoresistance at room temperature in excess of about 10%.

The data have been analysed using the model developed above, the result of which is shown in the figure as the solid lines. In all fits, the temperature dependence of the elastic tunnel contribution G_T is assumed to follow Eq. (6.3) using average barrier parameters obtained by fitting the low temperature current-voltage characteristics for both parallel and antiparallel aligned magnetizations. As can be seen, the model describes the data perfectly. The individual temperature dependent contributions to the conductance are shown in Fig. 6.2. In Fig. 6.2(a) the normalized conductance difference $\Delta G(T)/G_T(T) = 2P_1(T)P_2(T)$ is shown. As can be seen from the figure, the product of the polarizations decreases in the full temperature range by about 22%. In the absence of an indirect tunnel contribution, this drop may be related to a reduction of the magnetoresistance using Eq. (6.2). This results in an expected magnetoresistance at room temperature of 25%, significantly higher than the experimentally found 18%.

By fitting the data in Fig. 6.2(a) to Eq. (6.8) the parameters $\alpha_{i,1}$ and $\alpha_{i,2}$ in Eq. (6.4) have been obtained. Because the dependence of the model on the individual param-
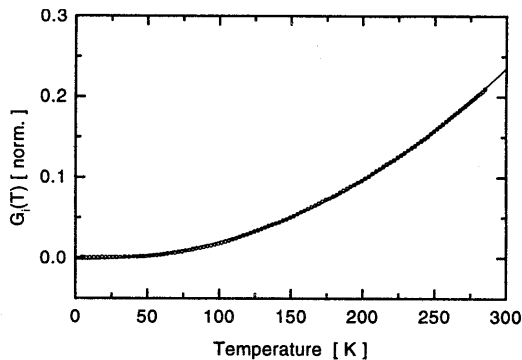
Figure 6.3: Analysis of the temperature dependence of the inelastic part of the conductance of an Al-Al$_2$O$_3$-Al reference junction. The normalized inelastic tunnel conductance $G_i(T) = [\langle G(T) \rangle - G_T(T)]/G_T(0)$. The symbols are the derived from the measured data, the solid lines are the result of the analysis as discussed in the text. For the temperature dependence of $G_T(T)$ use is made of Eq. (6.3) with barrier parameters $\phi = 2.1$ eV and $s = 1.42$ nm.

eters α_i is weak, only the sum $\alpha_{i,1} + \alpha_{i,2} \approx 4.66 \times 10^{-5}$ K$^{-3/2}$ could be obtained, which consistent with the values reported for similar junctions by Shang *et al.* cite-Shang:prb98. Note, however, that a significant difference in the α_i parameters for Co and Ni$_{80}$Fe$_{20}$ electrodes is to be expected, based on the difference in Curie temperatures ($T_C = 1360$ K for Co, $T_C = 850$ K for Ni$_{80}$Fe$_{20}$). The obtained values are in the same range as have been reported for interface and bulk magnetization [93].

In Fig. 6.2(b) the indirect part of the tunnel conductance has been shown, as obtained using Eq. (6.9). The amount of indirect conduction at room temperature is about 22% of the direct tunnel contribution at low temperatures. Since the indirect conduction within this model is independent of the magnetic configuration, the additional conductance results in an extra decrease of the magnetoresistance at room temperature on top of the reduction discussed above.

The data can be fitted well using a power-law dependence of the conductance $G_i \propto T^\gamma$, where for this sample $\gamma = 1.56 \pm 0.01$. The possible origins of the observed power-law behavior are several, but most proposed mechanisms are related to conduction processes involving indirect tunneling paths via impurities or defects in the barrier [88]. Impurities in the barrier may be introduced during the fabrication process in a number of different ways. Firstly, during the deposition of the barrier material (in this case Al) impurities can be introduced depending on the purity of the target materials and the background pressure, and for sputtered layers also of the sputter gas. A second possibility arises during the process of plasma oxidation, which is assumed to involve diffusion processes of metal ions (not necessarily only Al) towards the vacuum interface and/or oxygen ions (and possibly other negative ions) into the barrier. Recent progress by several groups in the characterization of the thus produced barrier by TEM and other techniques seems to support the idea that the formed barrier is mostly amor-

phous, see for instance Fig. 3.5), and it would therefore not be surprising if this would be an intrinsic source of defect states. Also, during the deposition of the top electrode, impurities may be introduced in the barrier due injection of highly energetic particles. Even when the fabrication process is completed, impurities may still be introduced by intermixing at the interfaces due to diffusion processes.

The indirect contribution is not special to the case of magnetic tunnel junctions, since the mechanisms discussed for the inclusion of impurities also apply to the case of nonmagnetic junctions. In Fig. 6.3 the results of the temperature dependence of a nonmagnetic junction is analysed using the same model. Also in this case, the indirect contribution at room temperature amounts about 21% to the total conductivity. The exponent, however, is larger, in this case $\gamma = 2.21 \pm 0.01$. Glazman and Matveev [95] presented a theoretical model in which that the value of the exponent γ for a tunnel process involving multiple impurity sites depends on the number of sites. If the number of impurities in a conduction path is N, and the $N-1$ hops between two impurities involve inelastic processes to compensate for the difference in energy levels (the hop from the electrodes to the first and last impurity is assumed elastic as a result of the continuum of available states in the electrodes), the exponent $\gamma(N) = N - [2/(N+1)]$. Thus, for a larger number of sites, the temperature dependence is stronger. This theoretical prediction has proved valuable in the case of amorphous barrier of Si and Ge, where the behavior of the resistance as a function of temperature can be interpreted as a shift of the dominant conduction mechanism to less abundant conduction paths involving an increasing number of defects [96–98]. In the present case the whole temperature regime is fitted using a single exponent, with an effective value in between the value predicted for one [$\gamma(N = 2) = 1.33$] and two [$\gamma(N = 3) = 2.50$] inelastic hops.

6.3   Spin-wave emission or absorption during tunneling

A second theory on the dependence of the JMR on the temperature has been developed by Zhang et al. [89]. It also provides an explanation for the dependence of the JMR on the applied bias voltage, which will be included here for completeness. In this theory, thermal or bias voltage assisted spin-wave emission or absorption by the tunneling electrons during the tunnel process is considered. This is an inelastic process whereby the tunneling electron loses or gains energy. The energy difference is available due to the application of a bias voltage, which raises the potential energy of one of the electrodes, or due to elevated temperatures, where energy levels are occupied in accordance with the Fermi-distribution. When an electron emits a spin-wave during the tunnel process, the spin of the electron flips. Therefore, the role of the spin-direction in the receiving electrode is reversed. As a result, the JMR contribution for this process is opposite in sign compared to direct tunneling, and the JMR always decreases.

Zhang et al. [89] have derived expressions for the extra conductance contribution in the limiting cases of low bias voltage or low temperatures. In the derivation, a two dimensional (2D) parabolic spin-wave dispersion relation is assumed, with a low energy cutoff resulting from the finite size of the magnetic grains, magnetic anisotropy, or the limited interaction area of a tunneling electron [99]. In both cases, a single addi-

tional term can describe the excess conductances [their Eqs. (8-10)[1]]. The conductance $G = J/V$ at zero voltage and zero temperature is denoted $G_{\gamma,0}$, where $\gamma = (P, AP)$ determines the alignment of the magnitization directions of the electrodes. The added components for the bias voltage and temperature dependence are denoted $\Delta G_{\gamma,V}$ and $\Delta G_{\gamma,T}$, respectively. For two identical electrodes, the conductance can be written as:

$$G_\gamma(V)_{T=0} = G_{\gamma,0} + \Delta G_{\gamma,V}(V) \qquad (6.10)$$

$$G_\gamma(T)_{V=0} = G_{\gamma,0} + \Delta G_{\gamma,T}(T) \qquad (6.11)$$

where

$$G_{\gamma,0} = \frac{4\pi e^2}{\hbar} \left[\left| T^d \right|^2 + 2S^2 \left| T^J \right|^2 \right] \xi_\gamma \qquad (6.12)$$

$$\Delta G_{\gamma,V}(V) = \frac{4\pi e^2}{\hbar} \left| T^J \right|^2 \nu(V)\xi_{-\gamma} \qquad (6.13)$$

$$\Delta G_{\gamma,T}(T) = \frac{4\pi e^2}{\hbar} \frac{2SkT}{E_m} \left| T^J \right|^2 \tau(T)\xi_{-\gamma} \qquad (6.14)$$

and

$$\xi_\gamma = \begin{cases} \rho_M^2 + \rho_m^2 & \text{when } \gamma = P \\ 2\rho_m\rho_M & \text{when } \gamma = AP \end{cases} \qquad (6.15)$$

$$\nu(V) = \begin{cases} SeV/E_m & \text{for } eV < E_m \\ S(2 - E_m/eV) & \text{for } eV > E_m \end{cases} \qquad (6.16)$$

$$\tau(T) = -\ln\left[1 - \exp(-E_c/kT) \right] \qquad \text{for } kT > E_c \qquad (6.17)$$

where T^d and T^J are the transfer matrices for direct (as a result of the overlap of the wave-functions inside the barrier) and spin-dependent (as a result of the overlap of the wave-functions at the interfaces) tunneling, respectively, and are assumed independent of energy and spin. In the analysis below we assume that the spin quantum number $S = 3/2$. The factors $\rho_{M,m}$ describe the spin density of tunneling electrons for the majority (M) and minority (m) electrons, respectively. For the direct elastic tunneling contribution $G_{\gamma,0}$ the Julliere result [15, 50, 51] is recovered. Both inelastic contributions have the same dependence on ξ as the direct elastic contribution, except that the parallel and antiparallel alignments have been exchanged (i.e., they contribute negatively to the JMR). The bias voltage and temperature dependences are described by the functions $\nu(V)$ and $\tau(T)$, respectively, which do *not* depend on the alignment of the magnetic moments of the electrodes.

Two critical energy scales are introduced, both related to the magnetic properties of the electrodes. The bias voltage dependence scales with the energy E_m, which is

---

[1]A factor $\left| T^J \right|^2$ has incorrectly been omitted by Zhang *et al.* [89, 100] from their Eq. (10), here correctly presented in Eq. (6.14).
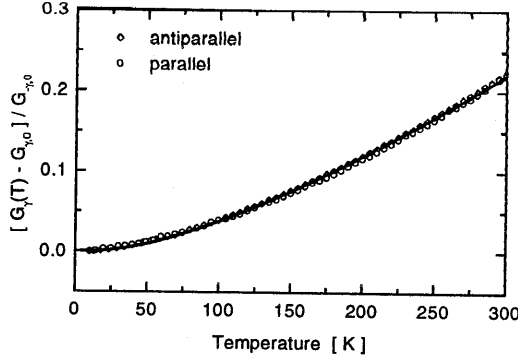
Figure 6.4: Comparison of the temperature dependence of the temperature induced conduction increase according to Eq. (6.19). The symbols are the derived from the measured data ($\circ$ for $\gamma = $ P, $\diamond$ for $\gamma = $ AP). The solid line is a fit to the data, as discussed in the text. A correction has been made for the temperature dependence of $G_{\gamma,o}(T)$, using Eq. (6.3) with barrier parameters $\phi = 3.4$ eV and $s = 0.94$ nm.

related to the Curie temperature T_C by $E_m = 3kT_C/(S+1)$. For bias voltages below this energy scale, $\Delta G_{\gamma,v}$ increases linearly with bias voltage, and more slowly for higher bias voltages. The temperature dependence depends on E_m, and also weekly on the lower wavelength cutoff energy E_c of the spin-wave spectrum.

Due to the assumption of constant $\left|T^d\right|^2$ and $\left|T^J\right|^2$ at non-zero bias voltage, the derived equations are limited to voltages where the conductance (in the absence of inelastic scattering) is constant, or the I-V curve is linear. The number of independent parameters can be reduced by normalizing Eqs. (6.10) and (6.11) using:

$$\frac{G_\gamma(V)_{T=0} - G_{\gamma,0}}{G_{-\gamma,0}} = \frac{\left|T^J\right|^2}{\left|T^d\right|^2 + 2S\left|T^J\right|^2} \, \nu(V), \qquad (6.18)$$

$$\frac{G_\gamma(T)_{V=0} - G_{\gamma,0}}{G_{-\gamma,0}} = \frac{2SkT}{E_m} \frac{\left|T^J\right|^2}{\left|T^d\right|^2 + 2S\left|T^J\right|^2} \, \tau(T). \qquad (6.19)$$

An advantage of this normalizing scheme is that the effect of some of the underlying assumptions divide out, which makes the result more general. It also shows the principal dependencies on both $\nu(V)$ and $\tau(T)$. Note that both right hand sides are independent of alignment of the electrode magnetization directions. Thus, it should be possible to normalize the data of both parallel and antiparallel alignment onto the same curve.

Fig. 6.4 shows the same experimental data as used in the previous Section. Again, the data have been corrected for the temperature dependence of the direct elastic tunnel contribution $G_{\gamma,0}$ using Eq. (6.3). Note that the two experimental curves almost perfectly coincide over the whole temperature range, showing that an analysis based on Eq. (6.19) is indeed possible.

The fit, using the fitting function $f(T) = AkT/e\,\tau(T)$, is in perfect agreement with

the experimental data. The value for $A = 4.28 \pm 0.04$ V^{-1} corresponds to a ratio of $\left|T^d\right|^2 / \left|T^J\right|^2$ ranging from 2 to 5, when E_m is varied between 90 meV (corresponding to $T_C(\text{Fe}_{80}\text{Ni}_{20}) = 850$ K) and 140 meV (corresponding to $T_C(\text{Co}) = 1360$ K). These values are significantly lower than the corresponding value of 17 obtained by Zhang *et al.* [89], from an analysis of the bias voltage dependence of the JMR. They argued that $\left|T^d\right|^2$ is expected to be one or two orders of magnitude larger than $\left|T^J\right|^2$. As already mentioned in Section 6.2, the Curie temperature at the interface may be reduced from the bulk value, and therefore E_m might be overestimated in the present case. However, in order to obtain the same ratio as Zhang *et al.*, a value of $E_m \approx 35$ meV ($T_C \approx 400$ K) would be necessary, which seem unrealistically low. For the spin-wave cutoff energy, a value of $E_c = 2.80 \pm 0.07$ meV is obtained, close to but slightly lower than the value of 4 meV obtained by Zhang *et al.* [89]. Unfortunately, the bias voltage dependence has not been measured with enough accuracy to facilitate a full comparison with the theory.

It should be mentioned that the theory as proposed by Zhang *et al.* contains only two parameters which can not be determined from independent measurements, the ratio $\left|T^d\right|^2 / \left|T^J\right|^2$ and E_c, the last of which has only a weak influence on the results. The theory contains both the voltage and temperature dependence, which makes this theory more generally applicable than the theory used in Section 6.2.

6.4   Conclusion

In conclusion, two models have been discussed which both can equally well account for the experimental data on the temperature dependence of the junction magnetoresistance, using realistic parameters. The model presented in Section 6.2 describes the temperature dependence in terms of the effects of spin-wave excitations in the electrodes and an additional spin independent, temperature dependent conductance. The effect of the spin-waves considered is a decrease of the alignment of the magnetizations at elevated temperatures and how this influences the *elastic* tunnel contribution. The model presented in Section 6.3, on the other hand, describes the temperature dependence in terms of an *inelastic* spin-dependent conductance contribution, resulting from the emission or absorption of spin-wave excitations during the tunnel process. Both of these models predict that the magnetoresistance reduction scales with the exchange stiffness at the interface between the magnetic electrode and the barrier. Thus, more optimal magnetic tunnel junctions may be produced by preparing magnetic interfaces with a higher Curie temperature.

An additional ingredient of the model dependence as described in Section 6.2 is a thermally assisted tunneling processes which do not depend on the magnetic configuration. This mechanism is also present in nonmagnetic junctions and causes an additional reduction of the magnetoresistance for magnetic tunnel junctions. When the interpretation is correct that the additional inelastic conductance is a consequence of thermally assisted tunneling through impurity or defect states, reducing the relative amount of this contribution might be found in improving preparation conditions of the barrier material, or in reducing the barrier thickness. We note that the quest for lower tunnel resistances

will anyhow lead to more interest in junctions with a reduced barrier thickness. Since the elastic tunnel conduction depends more strongly on the barrier layer thickness than impurity assisted conductance, already this effect will lead to a higher JMR ratio.

Chapter 7

Characterization of Magnetic Tunnel Junctions Using IETS

Abstract:*

In this Chapter inelastic electron tunneling spectroscopy measurements are presented on tunnel junctions containing both magnetic and nonmagnetic electrodes. Magnon excitations have been found near zero voltage; phonons are observed between 30 and 110 mV. Therefore, a model description of the transport properties of magnetic tunnel junctions at elevated temperatures or non-zero bias voltage should include both ineleastic contributions.

7.1   Introduction

Tunnel junctions containing two ferromagnetic electrodes separated by an insulator show a sizable junction magnetoresistance (JMR) effect depending on the relative orientation of the electrode magnetizations [16]. The magnitude of the JMR at zero temperature and zero voltage is determined by the polarization of the tunneling electrons and can be understood by Julliere's model [15, 50, 51]. However, the decrease of the JMR at elevated temperatures and non-zero bias voltage is not yet understood. It has been suggested that impurity, phonon, and magnon assisted tunneling processes contribute to the decreasing JMR [62, 89, 101]. We have performed a detailed study on the temperature dependence of the transport properties of tunnel junctions [87, 88], with the goal to provide an experimental basis for an improved model description. In this paper inelastic electron tunneling spectroscopy (IETS) [68] is used to show that inelastic phonon and magnon assisted contributions to the tunnel current are significant.

The junctions used in this study have been fabricated using shadow evaporation onto glass substrates, similar to the the method described in Ref. [16]. This results in a cross-strip geometry junction with an area of $\sim 200 \times 300 \ \mu m^2$. The tunnel barriers are formed as a native oxide or nitride on 10-nm-thick thermally evaporated Al strips using an *in-situ* O_2 or N_2 dc glow discharge. The 20-nm-thick counter electrodes were e-gun evaporated Co, or thermally evaporated $Ni_{80}Fe_{20}$, Cu, Al, or Au strips. The resistance of the studied junctions was of the order of a few $k\Omega$.

7.2   Results

In Figs. 7.1 and 7.2 the dynamic conductance ($G = dI/dV$) and the inelastic electron tunneling spectra, i.e., the derivative of the dynamic conductance versus voltage (dG/dV), of some of the tunnel junctions are shown. The results for the Al_2O_3 (Fig. 7.1) and AlN (Fig. 7.2) barriers are very similar. In Figs. 7.1(a) and 7.2(a) one of the electrodes is magnetic, while in Figs. 7.1(b) and 7.2(b) both electrodes are nonmagnetic. In all cases no fine-structure is observed in the IETS measurements at high voltages, where contributions from water and carbon contaminations would show up [68]. This indicates that the barrier preparation process is very clean.

A peak around $V = 115$ mV dominates the IETS measurements, which has been identified as an Al-O stretching mode for the Al_2O_3 barrier [68] and as a TO phonon mode for the AlN barrier [102]. This large inelastic peak shows up as a clearly visible knee in the G-V curves, which becomes even better resolved when the sample is cooled to $T = 1.1$ K (not shown). Closer examination of the IETS measurements reveals that the peak around 115 mV has a low voltage shoulder extending to about 30 mV [68, 102]. This is best seen in Figs. 7.1(b) and 7.2(b), where a third order polynomial fit through the high voltage data indicates the elastic tunnel contribution.

Near zero voltage an anomaly is observed in the G-V curves for the junctions in which the top electrode is magnetic [Fig. 7.1(a) and 7.2(a)], while the anomaly is absent when the top electrode is nonmagnetic [Fig. 7.1(b) and 7.2(b)]. In the IETS measurements, this anomaly results in a large feature for which the sharpness is limited by
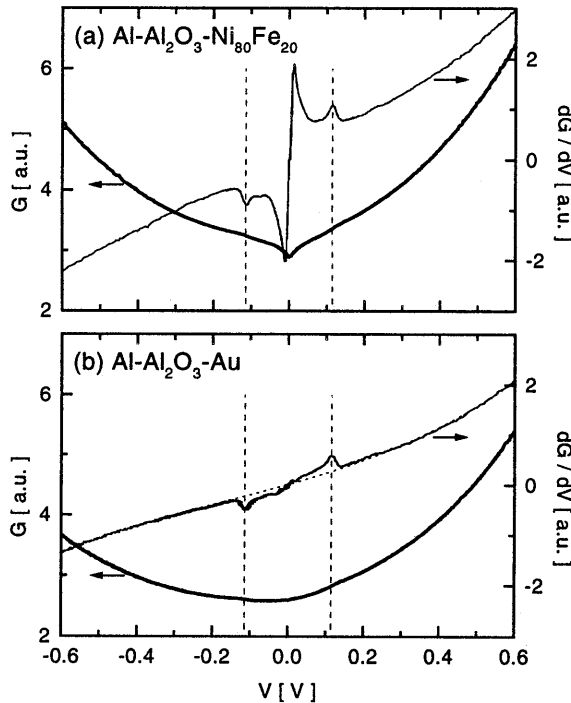
Figure 7.1: Conductance and IETS measurements at $T = 4.2$ K of (a) an Al-Al_2O_3-$Ni_{80}Fe_{20}$ junction (Co showed similar results) and (b) an Al-Al_2O_3-Au junction (Cu and Al showed similar results). The ac voltage excitation was ~ 1 mV$_{p-p}$ for the G-V and ~ 10 mV$_{p-p}$ for the IETS measurements. The vertical dashed lines indicate 115 mV. The dotted line in (b) illustrates the elastic part of the IETS measurement.

the modulation voltage only. Since the anomaly is only observed in the presence of a magnetic electrode, this feature is tentatively ascribed to magnon excitations. The temperature dependence of the peak around 115 mV in the IETS measurements also seems to indicate a magnon contribution at that voltage, similar to an earlier observation of magnons in NiO by Tsui *et al.* [70, 87].

7.3   Discussion

The dip at zero voltage in the G-V curves for the junctions with magnetic electrodes is significant and indicates that the inelastic magnon contribution to the tunnel current can not be neglected in the description of the transport properties of magnetic tunnel junctions. In this Chapter, the energy needed for magnons excitation was available as a result of an applied bias voltage. However, also at elevated temperatures enough
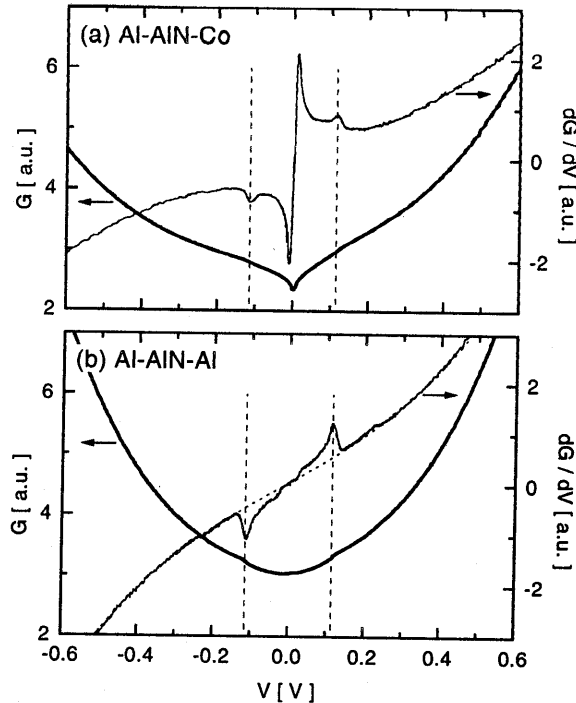
Figure 7.2: Conductance and IETS measurements at $T = 4.2$ K of (a) an Al-AlN-Co junction ($Ni_{80}Fe_{20}$ showed similar results) and (b) an Al-AlN-Al junction (Au and Cu showed similar results). The ac voltage excitation was ~ 1 mV_{p-p} for the G-V and ~ 10 mV_{p-p} for the IETS measurements. The vertical dashed lines indicate 115 mV. The dotted line in (b) illustrates the elastic part of the IETS measurement.

(thermal) energy is available to excite magnons (room temperature corresponds to an energy of 25 meV). Thus, the magnons will be excited both in the electrodes and during the tunnel process. Both these effects will influence the tunnel current at elevated temperatures, even at zero bias voltage. Indeed, we found in Chapter 6 that using mainly magnon excitations, either in the electrodes [87, 88] (Section 6.2) or during the tunnel process [103] (Section 6.3), the decreasing JMR of magnetic tunnel junctions at elevated temperatures can be explained.

Likewise, the occurence of the knee in the G-V curves illustrates that also the inelastic phonon contribution to the tunnel current can not be neglected. However, since the energy for phonon excitations corresponds to temperatures well above room temperature, the effect of the phonons shows up mainly in the voltage dependence and will not influence the temperature dependence much.

In conclusion, we performed IETS measurements on tunnel junctions containing both magnetic and non-magnetic electrodes. No indications of carbon or hydrogen

contaminations have been found, indicating that the barrier preparation process is very clean. A significant contribution to the tunnel current is observed for inelastic magnon and phonon excitations. Therefore we believe that both magnon and phonon contributions must be included in an improved description of the temperature and voltage dependence of the magnetoresistance of magnetic tunnel junctions.

Chapter 8

Influence of Oxidation Time on the Properties of Magnetic Tunnel Junctions

Abstract:[*]

The influence of the glow discharge oxidation time on the magneto-transport properties of cryogenically evaporated $Co-Al_2O_3-Ni_{80}Fe_{20}$ magnetic tunnel junctions has been studied. Initially, the starting metallic Al layer is found to progressively oxidize. However, already before the Al oxidation is completed, degradation of the barrier properties are observed. It is suggested that this is related to the premature formation of CoO underneath or Al-Co-O within the barrier.

8.1   Introduction

Magnetic tunnel junctions (MTJs) are presently being intensively researched for their large junction magnetoresistance (JMR) effect, which may potentially be applied in magnetic sensing or storage devices [16–20, 56, 104]. Although large JMR values have been reported, the fabrication process itself is still far from standard. Quite often poor JMR values have been found, while the other junction properties seemed to be fairly good. In this Chapter a comprehensive study is presented on the influence of oxidation time on the temperature dependent (magneto)-transport properties of Co–Al_2O_3–$Ni_{80}Fe_{20}$ MTJs fabricated by evaporation of the bottom electrode and of the Al on a substrate at cryogenic temperatures and glow-discharge oxidation. It will be shown that the experimental results can be explained from the progressive barrier oxidation and the subsequent properties of the interface formed between the bottom electrode and the barrier.

8.2   Experimental

The junctions used for this study have been prepared *in-situ* by evaporation through metallic shadow masks, resulting in a crossed strip junction geometry with a junction area of approximately 6×10^{-4} cm^2 [16]. The junctions consist of glass / 1-nm-Si / 8-nm-Co / d_{Al}-Al (oxidized for t_{ox} seconds) / 8-nm-$Ni_{80}Fe_{20}$ / 2-nm-AlO_x. The Si adhesion layer, the Co bottom electrode, and the metallic Al layer have been evaporated on a substrate at cryogenic temperatures to reduce surface roughness. The oxidation took place at room temperature using a dc-glow-discharge method in an O_2 pressure of $9 - 10 \times 10^{-3}$ Pa. After the room temperature evaporation of the top electrode the whole substrate was covered with a protective Al layer to prevent further oxidation in air. In both magnetic layers the magnetic easy axis was induced during growth by the application of a magnetic field. In order to compare the results, 72 junctions were fabricated in each run, containing three Al layer thicknesses ($d_{Al} = 1.0$, 1.2, and 1.4 nm) and four different oxidation times (t_{ox} ranging between 30 and 490 seconds). For these types of junctions the optimum oxidation time had previously been established; it varies slowly with Al layer thickness around 110 seconds [66]. Therefore we expected for the junctions oxidized for shorter duration to have leftover Al, while the longest oxidation times should lead to oxidation of the bottom electrode. All the results presented in this Chapter are for barriers formed from a 1.2-nm-thick metallic Al layer; the results for the other two thicknesses showed similar behavior.

8.3   Results and discussion

In Fig. 8.1 the low-temperature current-voltage characteristics of a subset of the junctions have been displayed. The shape of the curves is clearly different for the $t_{ox} = 30$ and 150 sec junctions as compared to the $t_{ox} = 360$ sec junction. The latter shows more curvature at lower voltages, indicating a lower barrier height. Also, the resistance
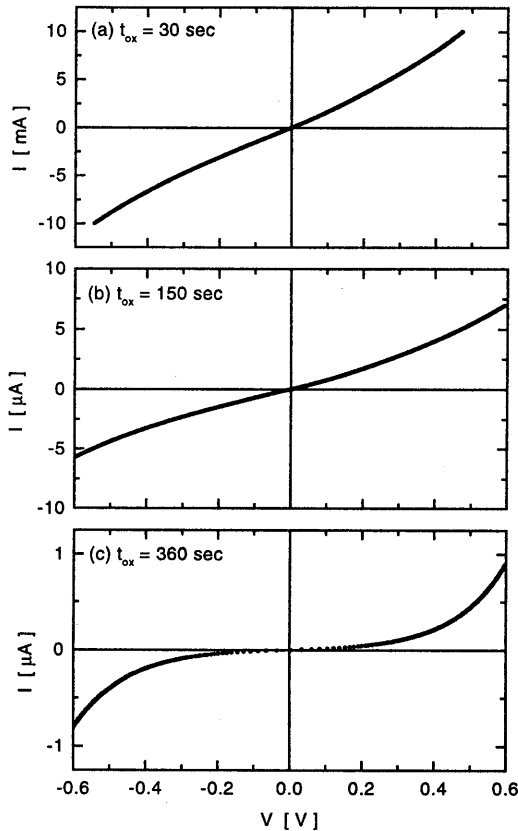
Figure 8.1: Current-voltage characteristics at $T = 10$ K (parallel alignment) for barriers oxidized for (a) $t_{ox} = 30$, (b) 150, and (c) 360 sec. Note the different scale in (a).

[at zero-voltage and when the magnetic moments of the electrodes are aligned parallel, $R_p = (dI/dV|_{V=0})^{-1}$] shows a five orders of magnitude increase with increasing oxidation time, from $R_p = 68$ Ω to 8.0 MΩ for $t_{ox} = 30$ and 360 sec, respectively.

The current-voltage characteristics obtained at $T = 10$ K and at room temperature were analyzed by fitting the data to the symmetric barrier model of Simmons [47], resulting in model parameter values for ϕ and w which are the barrier height and barrier width, respectively, see Fig. 8.2 [105]. The data taken at $T = 10$ K show two regimes. For short oxidation times ($t_{ox} \le 250$ sec), the barrier height is roughly constant and the barrier width increases linearly in time. This reflects the gradual transformation of Al into Al_2O_3, which surprisingly starts with a 1.2 nm offset. The offset most probably results from quasi-instantaneous thermal oxidation in an oxygen atmosphere before the glow-discharge is started (at most one minute). At $t_{ox} = 250$ sec, all Al seems to be oxidized, resulting in an Al_2O_3 barrier thickness of $w = 1.9$ nm, which is about 20% higher than expected, based on the 30% difference in density, for the 1.2-nm-thick Al
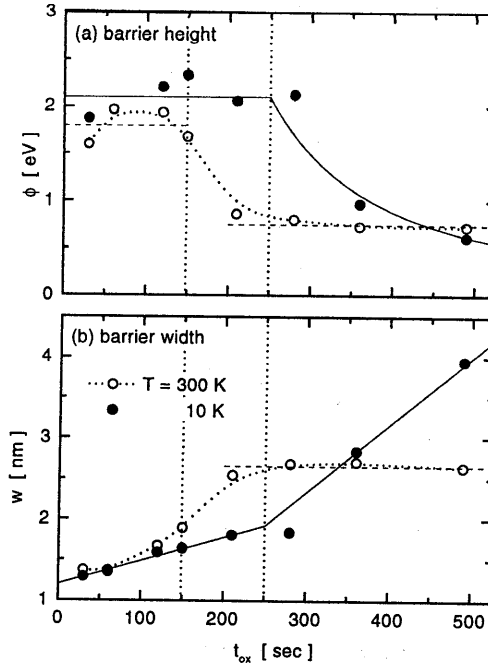
Figure 8.2: (a) Barrier height ϕ and (b) barrier width w dependence on the oxidation time t_{ox} obtained by fitting current-voltage characteristics ($|V| \leq 0.4$ V, parallel alignment) to Simmons's tunnel formula (Ref. [47]) at (o) room temperature and (•) 10 K. The dashed lines are guides to the eye, the solid lines are explained in the text.

starting layer. For longer oxidation times ($t_{ox} \geq 250$ sec) w still increases linearly in time as the Co bottom electrode starts to oxidize. However, the slope differs, and ϕ decreases steadily.

These results can be understood within the WKB approximation used in Simmons's model [47] in which the tunnel current is dominated by the integral $\int \phi^{1/2}(x)dx$. For a composite barrier, if it is assumed that the total barrier width $w_{total} = w_{Al_2O_3} + w_{CoO}$ increases linearly with oxidation time [as suggested by Fig. 8.2(b)] and the barrier height for Al$_2$O$_3$ and CoO are constants, this leads to an effective barrier height

$$\phi_{eff}^{1/2} w_{total} = \phi_{Al_2O_3}^{1/2} w_{Al_2O_3} + \phi_{CoO}^{1/2} w_{CoO}, \tag{8.1}$$

which is not inconsistent with our data as indicated by the solid line in Fig. 8.2(a) [using $\phi_{Al_2O_3} = 2.1$ eV, $\phi_{CoO} = 25$ meV (corresponding to the thermal energy at room temperature), and $w_{Al_2O_3}$ and w_{CoO} as indicated by the solid line in Fig. 8.2(b)].

The data taken at room temperature present a completely different trend. For oxidation times $t_{ox} \leq 150$ sec, the barrier width hardly changes from the low temperature values and the height is reduced by only a few tenths of an eV. This decrease is most likely the effect of additional thermally activated leakage currents on the fit, which is
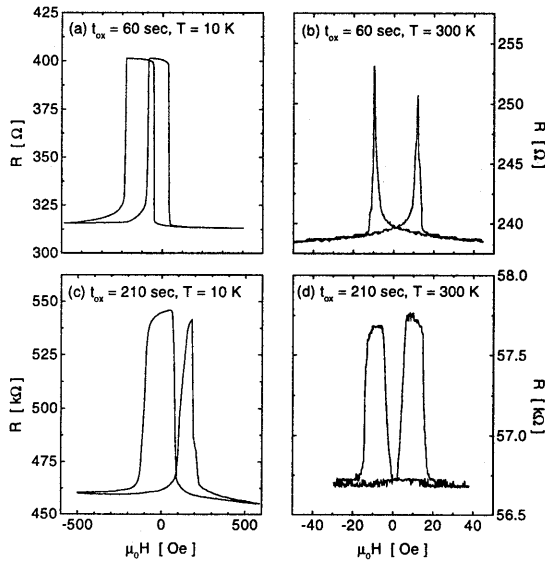
Figure 8.3: Room temperature and 10 K magnetoresistance curves for junctions oxidized for (a,b) $t_{ox} = 60$ and (c,d) 210 sec. Note the different scales.

based on elastic tunneling only. For a regular junction the estimated leakage current contributes 15-20% to the total current at room temperature [87, 88]. For oxidation times $t_{ox} \geq 150$ sec, however, the fitting parameters deviate significantly from their low temperature values, settling to values independent of oxidation time for $t_{ox} \geq 200$ sec.

By comparing the two data sets one finds, quite surprisingly, that the transition at room temperature occurs for significantly shorter oxidation times ($t_{ox} \approx 150$ sec) than the transition at $T = 10$ K ($t_{ox} \approx 250$ sec). This observation seems to imply that Co is being incorporated within (as impurities) or underneath (as CoO) the barrier before Al has been completely oxidized. The thus formed barrier seems to support a thermally activated electron transport mechanism, which dominates at elevated temperatures over the regular elastic tunneling. Therefore, even though the electron transport at low temperatures can be satisfactorily described by elastic tunneling through a composite barrier, this is clearly not possible at room temperature. Supporting evidence for this interpretation is found in all experiments described below.

In Fig. 8.3 the low temperature and room temperature magnetoresistance curves are shown for a subset of the junctions. The room-temperature magnetoresistance curves for the 30 and 60 seconds oxidized junctions [see Fig. 8.3(a)] show peaks for both field directions due to the overlap of the coercive fields of both magnetic electrodes. This means that the magnetoresistance ratios obtained for these junctions are not fully representative of the intrinsic behavior, since a full anti-parallel alignment is not obtained. For the longer oxidized junctions, however, a clear plateau is found in the room temperature magnetoresistance curves, see Fig. 8.3(c). The details of the magnetic behavior have been studied by MOKE and SQUID and will be presented separately [106].
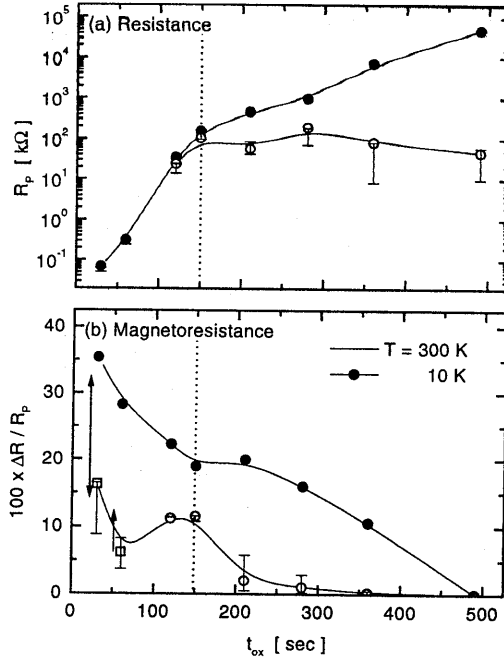
Figure 8.4: (a) Resistance (R_p, parallel alignment) and (b) magnetoresistance (JMR) dependence on oxidation time t_{ox} at (○, □) room temperature and (•) 10 K (□ indicates peaked magnetoresistance curves for which the full MR ratio is larger than the value indicated, see Fig. 8.3). The error bars represent the spread in the observed values (6 per datapoint) at room temperature, the junctions represented by a symbol are examined more extensively. The lines are guides to the eye.

The resistance of all measured junctions in the parallel alignment is shown in Fig. 8.4(a). At room temperature, the resistance increases almost exponentially with oxidation time until saturation is reached around 150 seconds. For the short oxidation times ($t_{ox} < 150$ sec), the resistance increase at 10 K is comparable to the 15-20% found for regular junctions [87, 88]. For the longer oxidized samples ($t_{ox} > 150$ sec), however, this increase is much higher, the difference increasing with oxidation time. This observation reveals again that for the junctions at room temperature a thermally activated conduction mechanism dominates over the tunneling contribution.

Fig. 8.4(b) shows the magnetoresistance for all junctions. For all initial Al thicknesses we find a general behavior of decreasing magnetoresistance with increasing oxidation time, with a false plateau between the critical oxidation times as found above. Although it is tempting to relate this to progressive degradation of the barrier properties, we like to emphasize that model calculations generally show a decreasing magnetoresistance with increasing barrier width [107]. However, the extra strong decrease of the magnetoresistance at room temperature for oxidation times longer than 150 seconds is very likely due to the presence of Co in the barrier. CoO is paramagnetic
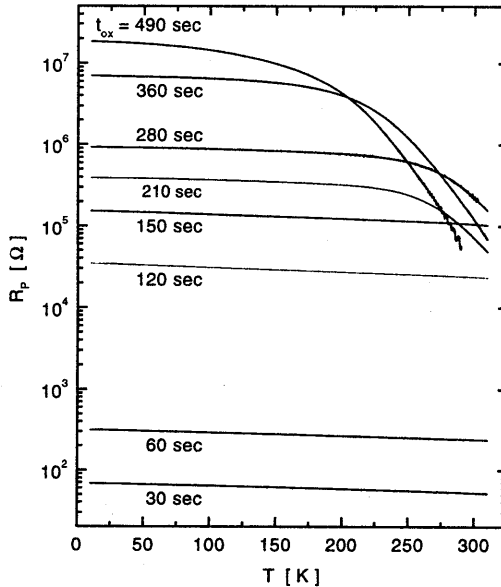
Figure 8.5: Temperature dependence of the resistance (parallel alignment) for different oxidation times t_{ox}.

at room temperature and its loose spins act as an efficient spin-mixer. Upon cooling (which was performed in a large magnetic field) through the blocking temperature of CoO ($T_{b,CoO} \approx 280$ K), an antiferromagnetic ordering takes place. In the ordered state of CoO the magnetic moments are fixed into a stiff co-linear alignment in which spin-mixing is reduced. Consequently, the magnetoresistance reappears, as observed in the data taken at 10 K. Another possible cause could be a lower effective spin polarization for the dominating activated conduction mechanism at room temperature (like for impurity assisted tunneling [108]). Parenthetically we note that the resistances of the 30 seconds oxidized junctions are comparable to the sheet resistance of the electrodes (~ 30 Ω) and is, therefore, influenced by the geometrical enhancement effect [79, 83, 109] (in this case an estimated relative increase of about 15%).

Perhaps the most compelling evidence for the progressive degradation of the barrier is the clearly visible additional conductance at elevated temperatures for the longer oxidized junctions, as shown by the temperature dependence of the resistance in Fig. 8.5. For junctions oxidized for shorter duration ($t_{ox} \leq 150$ sec) the conductance is dominated by tunneling in the whole temperature range, resulting in the normal weak temperature dependence [87, 88]. For longer oxidation times, however, an additional conduction mechanism contributes in the temperature range covered by the present experiments. This contribution is clearly thermally activated and increasing with increasing oxidation time. Note the decreasing resistance around room temperature for increasing oxidation time. The higher conductance suggests a degradation of the Al_2O_3 barrier, possibly due to progressive diffusion of Co ions into the Al_2O_3 barrier during pro-
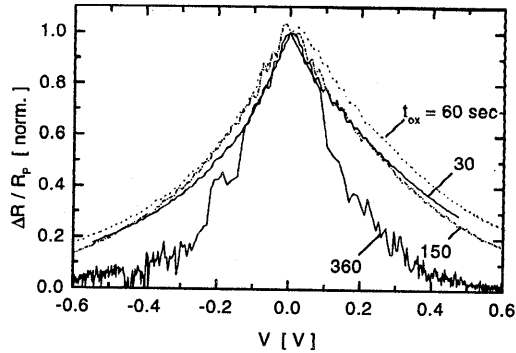
Figure 8.6: Bias voltage dependence of the magnetoresistance at $T = 10$ K for different oxidation times t_{ox}.

longed oxidation. Considering the different onset temperatures for different oxidation times, it should be clear that caution should be exercised when data at only a single temperature are available.

As a final result, Fig. 8.6 shows the bias voltage dependence at $T = 10$ K for junctions with different oxidation times. Although the general shape of the curves is similar for all junctions, both the asymmetry and the voltage V_{half} at which the magnetoresistance is reduced to half the zero voltage value depend on the oxidation time. The maximum V_{half} is found for $t_{ox} = 60$ sec. For voltages with the Co electrode positive, V_{half} amounts to 0.328 mV, whereas $V_{half} = 0.230$ mV for negative bias. Also the asymmetry in V_{half} is largest for this junction.

8.4   Conclusions

In conclusion, we find that initially the barrier formation behaves as expected, showing a linear increase in barrier thickness with oxidation time (exponential increase in resistance). However, already before all Al has reacted, effects related to the oxidation of the underlying electrode are observed. In our case of a Co bottom electrode, this leads to the formation of CoO underneath or diffusion of Co into the barrier. Both mechanisms lead to loose magnetic Co moments within the barrier at room temperature, which act as efficient spin-mixers and host a thermally activated transport mechanism, reducing both the resistance and magnetoresistance at room temperature. At low temperatures, the Co magnetic moments are frozen and the thermally activated conduction disappears. This causes a dramatic increase of the resistance and the reappearance of magnetoresistance.

Chapter 9

Observation of Quantum Well States in Magnetic Tunnel Junctions

Abstract:[*]

Magnetic tunnel junctions with a nonmagnetic interface layer have been studied for their magnetotransport behavior. The initial effect of the added layer is to reduction the magnetoresistance effect. Also, the bias voltage dependence of the magnetoresistance becomes increasingly more asymmetric. The dependence of the magnetoresistance both on the thickness of the interface layer as well as on the bias voltage can be interpreted as signatures of the development of quantum well states.

9.1   Introduction

Ever since the first spin polarized tunneling (SPT) experiments were performed [49], this technique has richly contributed to the understanding of thin-film superconductivity and the behavior of magnetic films down to the sub-monolayer regime [58]. The latest development is the observation of spin dependent tunneling between two ferromagnetic (FM) electrodes [15–17,87]. The large junction magnetoresistance (JMR) in these latter structures has attracted much interest due to the possible application of these FM-I-FM trilayer structures (where I is the insulating tunnel barrier) as sensors and nonvolatile memory elements. From a fundamental viewpoint JMR offers the exciting possibility of studying conduction electron spin polarizations of various FM materials, at ambient conditions, and their temperature dependence [87,88], without the need for a superconducting detector and liquid helium temperatures as required by the earlier experiments.

In this Chapter, the spin polarized tunneling phenomenon in the presence of an ultra-thin layer of a nonmagnetic metal (NM) at the FM-I interface in FM-I-FM tunnel junctions is carefully explored. OUr experimental studies show in some cases a negative JMR effect and an unexpected bias voltage dependence. Recent theoretical calculations by Vedyayev *et al.* [110] and Zhang *et al.* [111] have predicted oscillations of the JMR in FM-NM-I-NM-FM systems as a function of the thickness of NM metal. In these calculations, the authors show that the interface layer behaves as a quantum well, leading to the formation of quantum well states (QWS) when a resonance condition is fullfilled. The occurence of a QWS at the Fermi energy results in an increase of the JMR. Moreover, for an asymmetric structure, such as FM-NM-I-FM, the sign of the JMR effect is predicted to oscillate as a function of the NM metal layer thickness. The above calculations were performed for the condition of low bias voltage. We have carried out experiments in search for these quantum effects and have extended the calculations to include the bias voltage dependence.

9.2   Preparation

Ferromagnetic tunnel junctions were prepared by thermal evaporation through shadow masks, as described in previous publications [16]. Onto liquid nitrogen cooled glass substrates, Co bottom electrode strips were prepared, half of which were covered by six different thicknesses of Au before the 1.4-nm-thick barrier Al film was deposited. After forming the oxide barrier at room temperature by glow discharge oxidation of the Al film, the top electrode of $Ni_{80}Fe_{20}$ film was deposited. Half of the resulting junctions were $Co/Au/Al_2O_3/Ni_{80}Fe_{20}$ whereas the other half were $Co/Al_2O_3/Ni_{80}Fe_{20}$ control samples. The Au thickness ranged from 0.1 to 1.2 nm, with 6 junctions for each Au thickness. Co and $Ni_{80}Fe_{20}$ films were grown in an applied magnetic field H to obtain well defined and sufficiently different coercive fields such that clear parallel and antiparallel magnetization states of the tunnel junctions resulted. Between the 1 mm wide top and bottom electrodes, an 8-nm-thick Al_2O_3 layer was deposited to cover the sides of the strips, leaving only a small junction area. (This procedure helped in the stability of the junctions and sustained bias voltages up to $|V_{dc}| \geq 2$ V, even at room
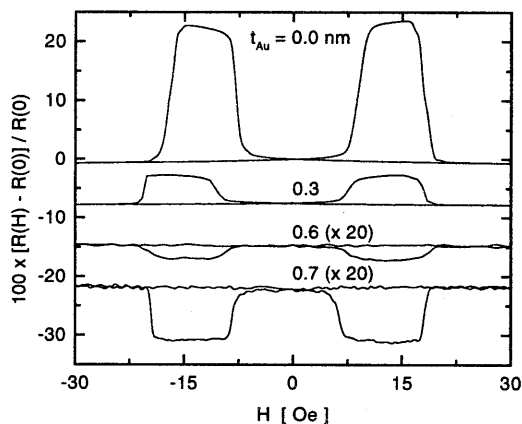
Figure 9.1: Magnetoresistance at zero bias voltage and 77 K of control junction and junctions with 0.3, 0.6, and 0.7-nm-thick Au interface layers. The curves are offset for clarity. The curves for 0.6 and 0.7 nm thickness have been magnified by a factor of 20.

temperature). Junction resistances (R_J) were below 25 kΩ and measured in a four terminal geometry using an LR-700 ac resistance bridge as well as by dc techniques. The latter method was used to obtain the bias voltage dependence of tunnel current, conductance, and JMR (defined as the percentage change in R_J in an applied field with respect to its peak resistance value). The measurements were carried out at 295 and 77 K.

9.3 Results

In Fig. 9.1, the junction resistance is plotted as a function of the applied magnetic field for a control junction and for junctions with an 0.3, 0.6, and 0.7-nm-thick Au interface layer. Large JMR is seen for the control junction as expected. However, with 0.3 nm Au over Co, a considerable drop in JMR is observed, showing only 4.9% JMR as compared to 18.9% with no Au. But with both 0.6 and 0.7 nm Au, a dramatic change is observed; the JMR becomes negative. This is the first case where a negative JMR has been seen in magnetic tunnel junctions. The dip occurs at exactly the same field range as the peak for zero or low Au coverage. This effect is stable and reproducible even after storing the sample for fifteen months in ambient conditions.

The above inverse JMR effect is observed at 295 and 77 K for Au coverage of 0.6–0.8 nm, both by ac as well as low dc bias voltage. Beyond about 0.9 nm Au, the JMR is immeasurably small (JMR < 0.01%) and remains so up to 1.2 nm Au, the highest Au thickness studied. The JMR as a function of Au thickness is shown in Fig. 9.2. The big drop in JMR as a function of the metal thickness in the range shown here, was also observed for other elements including Cu, Cr, Pd, and Ag. However, one of the junctions with 0.4 nm Cu at the interface also showed a negative JMR of 1.7%.
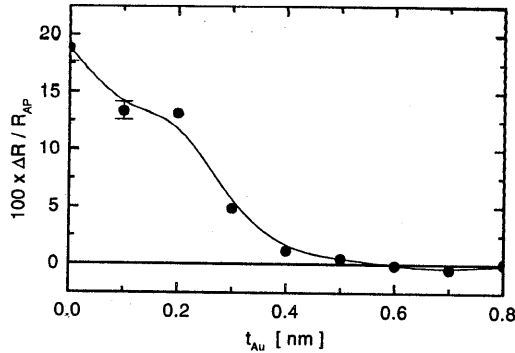
Figure 9.2: Dependence of magnetoresistance at zero bias voltage and 77 K on the thickness of Au interface layer.

Otherwise, only positive JMR or no JMR for larger thicknesses of Cu were seen.

In general, as reported before [87, 112, 113], for a FM-I-FM junction the JMR decreases monotonically as a function of bias voltage (see $t_{Au} = 0.0$ nm data in Fig. 9.3). For the present control junctions, the JMR decreased to a few percent at $|V_{dc}| \sim 0.7$ V and in some cases the junctions withstood $|V_{dc}| \geq 1.8$ V bias, still showing a measurable JMR. Asymmetry in the bias dependence of the JMR was always observed, as well as in the I-V data, as is generally the case for unequal electrode materials. These I-V measurements yielded average barrier heights above 2.5 eV and thicknesses in the range of 1.1–1.3 nm for the junctions, by fitting to Brinkman's formula [48].

The bias voltage dependencies of the JMR for various junctions with increasing Au at the interface are also shown in Fig. 9.3. An assymetrically decreasing JMR with bias voltage is found for Au thickness up to 0.4 nm, see Fig. 9.3(a). But for Au coverage of 0.5 nm and beyond, the bias voltage dependence is dramatically different; the JMR changes sign and the shape changes, see Fig. 9.3(b). For instance, with 0.5 nm Au, the JMR slightly increases initially before showing a decrease with positive bias (Co film positive), whereas for the reverse bias it is negative showing nearly a constant JMR beyond about -0.3 V. For 0.6 and 0.7 nm Au, the JMR is negative even at $V = 0$ V. With positive bias it becomes less negative and changes sign again between 0.2 and 0.4 V for the these two thicknesses. There is a broad peak in the JMR between 0.5 and 0.7 V and it crosses the axis once again at higher voltages. With reverse bias, the JMR continues to be negative, with a broad dip between -0.2 and -0.4 V. The position of the peak or dip is independent of the temperature between 295 and 77 K, even though the magnitude of the JMR changes. A very small ($< 0.05\%$) negative JMR was observed for 0.8 nm Au.

9.4   Discussion

There are a number of phenomena related with the Co/Au interface which might infuence the magnetoresistance. A first possible explanation, Moodera *et al.* [114], using a superconducting Al film as a spin detector, has reported direct measurements of the
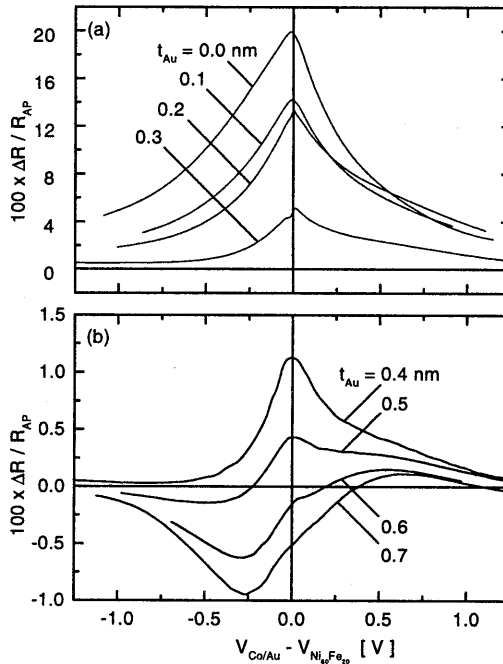
Figure 9.3: Dependence of magnetoresistance on bias voltage for increasing thicknesses of the Au interface layer at $T = 77$ K. (a) Measurements for $t_{NM} \leq 0.3$ nm; (b) $t_{NM} \geq 0.4$ nm.

tunneling electron spin polarization for $Fe/Au/Al_2O_3/Al$ junctions. The polarization showed a steep decrease with Au coverage, from a value of 44% without Au to $\sim$3% for about 0.4 nm of Au, and continued to drop with further increase of Au thickness. A similar reduction of the Co polarization with 0.4 nm added Au is not inconsistent with the present experiments in the Au thickness range of 0–0.4 nm. However, the polarization results can not explain the negative magnetoresistance and distinctive bias voltage dependence of the present results. As similar behavior is found for several elements, also band structure effects (beyond the effect due to the formation of quantum well states as discussed below) do not seem the main explanation.

In the remainder of this Chapter, we will show that quantum well states can qualitatively explain the features of the observed effects. Results from numerical calculations are presented, based on a model first proposed by Slonczewski [51], including recent extensions [63, 65]. Within the model, the transmission probabilities for electrons are calculated by solving the Schrödinger equation for free, non-interacting electrons in a potential energy landscape as defined in Fig. 9.4. Translation invariance is assumed within the plane of the junction. Within the constraints of the model assumptions, the tunnel current (at finite bias voltage) or conductance (at zero bias) is calculated exactly.

The configuration used in the calculations, see Fig. 9.4, consists of two identical magnetic layers (FM_1 and FM_2), the barrier layer (I), and a nonmagnetic metal (NM)
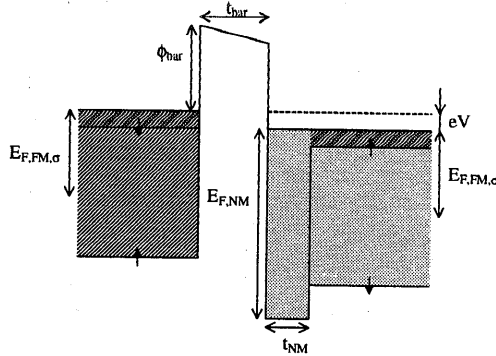
Figure 9.4: The potential energy landscape of the tunnel junctions with an additional nonmagnetic metallic layer on one side of the barrier in the antiparallel state. The sign of the bias voltage is defined with the right electrode being positive.
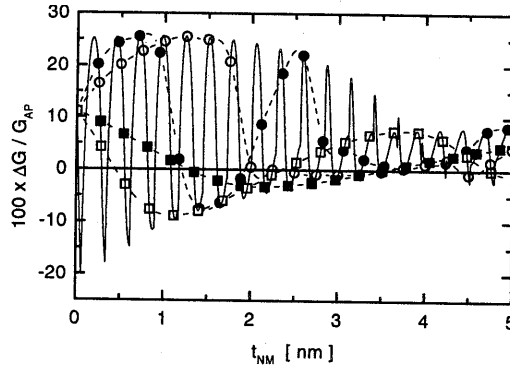
Figure 9.5: Calculated magnetoresistance at zero bias voltage for several hypothetical nonmagnetic metal layer thickness t_{NM}, using $E_{F,FMi} = 2.62 \pm 1.96$ eV, $E_{F,NM} = 5.51$ eV, $\phi_{bar} = 2.5$ eV, and $t_{bar} = 1.5$ nm. The continuous variation (solid line) is intersected at integer monolayers for several monolayer thicknesses $t_{ML,NM}$ (dashed lines). The monolayer thicknesses are (●) $t_{ML,NM} = 0.2355$ nm (representing Au<111>), (○) 0.25 nm, (■) 0.27 nm, and (□) 0.28 nm, respectively.

located between I and FM_2. For both ferromagnetic layers the Fermi energy is chosen to correspond with that of the well-known spin-split free-electron-like itinerant d-electron bands of Fe [57], i.e., $E_{F,FMi} = 2.62 + (-)1.96$ eV for the majority (minority) spin electrons. A typical symmetric barrier height and barrier width are chosen, $\phi_{bar} = 2.5$ eV and $t_{bar} = 1.5$ nm, respectively. The electronic parameters of the nonmagnetic metal of thickness t_{NM} are chosen to correspond to those of Au [90], i.e., $E_{F,NM} = 5.51$ eV. All electrons are assumed to have free electron mass and the calculations are performed for zero temperature. In analogy with the experiments, the sign of the bias voltage is defined as that of the FM_2/NM electrode with the FM_1 electrode as common.

In Fig. 9.5 the calculated magnetoresistance is shown for increasing thickness of the nonmagnetic metal layer up to $t_{NM} = 5.0$ nm. A number of qualitative observations can be made which do not depend on the details of the chosen parameters [110, 111]. The magnetoresistance oscillates between positive and negative values. The rapid oscillations correspond to QWS which develop when the round trip phase accumulation equals 2π. The period of this oscillation is $\pi/k_{F,NM}$ (in this case 0.261 nm), with $k_{F,NM}$ the wave number at the Fermi level inside the nonmagnetic metal layer. The envelope of the short period oscillations approaches a non-zero value (different from the value without nonmagnetic metal layer) in a damped oscillatory way for thicknesses $t_{NM} > 50$ nm. The persistence of the oscillations up to very large thicknesses results from the strong forward filtering effect of the barrier (only perpendicularly incident electrons contribute to the conductance). It should be noted that both Vedyayev *et al.* [110] and Zhang *et al.* [103] showed that breaking of phase coherence in a thick interface layer results in quenching of the JMR.

Since the thickness of the nonmagnetic metal layer can in the experiment not vary continuously, but only in steps of full monolayers, Fig. 9.5 also shows intersections for several fixed monolayer thicknesses. This aliasing effect [115] results in oscillations with a much longer period. For a monolayer thickness of 0.2355 nm, corresponding to the perpendicular bulk lattice parameter of Au<111>, the magnetoresistance initially increases. However, with a suitable choice of the ratio between the monolayer thickness and the Fermi wavelength of the NM metal, which within certain limits may be realized in thin films, the model calculations can reproduce the experimentally observed initial fast decrease of the magnetoresistance in a surprisingly quantitative way.

In Fig. 9.6 the calculated bias voltage dependence is shown for two monolayer thicknesses. A fast drop of the magnetoresistance is obtained with increasing nonmagnetic metal layer thickness. Without the nonmagnetic metal layer at the interface, the bias voltage dependence is symmetric around zero voltage and similar to previous model calculations [61, 63, 89, 108, 116, 117]. When the nonmagnetic metal layer increases in thickness, an asymmetry develops which describes several of the key features observed in the experimental data, such as the (multiple) zero crossings. Even the voltage scale at which the features occur is reproduced surpisingly well. However, most remarkably, the sign of the applied voltage seems to be mirrored, which is still not understood. A possible experimental explanation for the reversed sign is the formation of an Al_2-Au compound, called "purple plague," during the deposition. When, during the oxidation of this compound, the Au remains on top of the formed oxide, as a kind of surfactant, the actual measuring geometry would be reversed.

9.5   Conclusions

In conclusion, we have shown that the addition of a nonmagnetic interface layer causes a sharp reduction of the junction magnetoresistance, which can even become negative, and an unusual bias voltage dependence. Apart from the sign of the applied voltage, surprising good quantitative agreement could be obtained in simple model calculations, using realistic parameters. This study shows that the properties of magnetic tunnel junc-
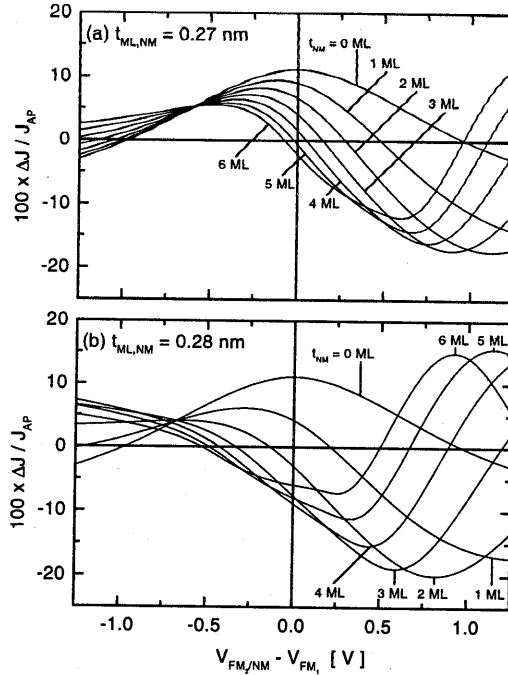
Figure 9.6: Calculated bias voltage dependence of the magnetoresistance at several fixed nonmagnetic metal layer thicknesses, using the same parameters as in Fig. 9.5, for (a) $t_{ML,NM} = 0.27$ nm, and (b) 0.28 nm.

tions are not solely determined by the properties of the interfaces between the insulator and the electrodes. In a next stage, electrodes may be engineered such that a stronger spin filtering is obtained, for example by using a FM/NM/FM trilayer electrode, with a suitably chosen thickness of the normal metal.

Chapter 10

Tunneling Electron Spin-Polarization of Transition Metal Alloys

Abstract:

For a range of $Ni_{1-x}Fe_x$ and $Co_{1-x}Fe_x$ alloys, the tunneling electron spin-polarization has been determined using a superconducting Al film as a spin sensitive detector in a tunnel experiment. The junctions used in this study have been prepared *in-situ*, using a glow-discharge fabrication process for the barrier layer. An improvement of the polarization has been observed for all alloys compared to previous reports on H_2O vapor oxidized junctions. This increase has been attributed to the difference in preparation conditions. The polarizations obtained using different barrier materials revealed little difference between Al_2O_3 and AlN, while MgO barriers showed lower values. Using these new polarization values, the predicted magnetoresistance within the Julliere model for magnetic tunnel junctions still exceeds present experimental reports.

10.1   Introduction

Recently, the magnetoresistance of magnetic tunnel junctions (MTJs), consisting of two ferromagnetic (FM) layers separated by a thin insulating (I) layer, has attracted much attention [16, 17]. Within the simple Julliere model [15, 50, 51], the magnitude of the magnetoresistance in this type of junction is determined solely by the product of the tunneling electron spin polarizations P, which is a characteristic property of the ferromagnetic electrode and the electrode/barrier interface. This polarization can be determined from a Spin Polarized Tunneling (SPT) experiment using a S/I/FM tunneling junction [49, 58], wherein Al is the most extensively used superconductor (S). In the present study the polarization of a range of $Ni_{1-x}Fe_x$ alloys, and of a few $Co_{1-x}Fe_x$ alloys has been determined for *in-situ* glow discharge formed Al_2O_3, AlN and MgO barrier layers. For the often used alloy permalloy, $Ni_{80}Fe_{20}$, the observed polarization is much higher than previously reported values [118] for *ex-situ* water vapor oxidized junctions. The improved values are the result of improved barrier and interface preparation conditions.

10.2   Experimental

The junctions were fabricated *in-situ* by thermal evaporation through metal shadow masks onto glass substrates. As a base electrode a 4.0–4.2-nm-thick Al long strip is evaporated on a cryogenically cooled substrate, which, for samples with an MgO barrier, is subsequently covered by a 1.2–1.6-nm-thick Mg layer. After warming the substrate to room temperature, an Al_2O_3, MgO, or AlN insulating layer was formed in a dc glow discharge in an oxygen or nitrogen atmosphere. The last step consisted of evaporation of a 20 to 25-nm-thick FM cross strip, where the FM was either $Ni_{1-x}Fe_x$ or $Co_{1-x}Fe_x$. The thickness of the layers was monitored using a quartz crystal oscillator. In one run, 72 junctions of 6×10^{-4} cm^2 area were prepared with resistances ranging from hundreds of ohms (AlN) to few kilohms (Al_2O_3 and MgO).

For each FM-I combination a number of junctions was cooled to $\sim$0.4 K using a standard triple bath crystat (N_2, pumped ^{4}He, and pumped ^{3}He). The T_c of the Al strip was obtained from resistance measurements on the Al long strip during the cooling of the junctions, and ranged between $T_c = 2.2$ K and 3 K (T gauged from pressure in ^{4}He bath). A magnetic field was applied in the film plane, which was achieved by rocking the sample. The film could be aligned very precisely by minimizing the zero voltage conductance in an applied magnetic field. During the measurements, a magnetic field in the range between 3 and 5 T was applied.

10.3   The Spin Polarized Tunneling experiment

In a Spin Polarized Tunneling experiment use is made of the Zeeman splitting in an applied magnetic field of the quasiparticle density of states (DOS) near the Fermi energy of a superconducting electrode [119]. For an ideal BCS superconductor, the BCS-DOS

ρ_{BCS} at zero applied magnetic is given by:

$$\frac{\rho_{BCS}(E)}{\rho_{NM}(E)} = \begin{cases} \frac{E}{(E^2-\Delta^2)^{1/2}} & \text{for } |E| > \Delta, \\ 0 & \text{for } |E| < \Delta, \end{cases} \qquad (10.1)$$

where E is measured from the Fermi-level, $\rho_{NM}(E)$ is the DOS of the electrode in the normal metallic state, and Δ is the superconducting energygap. In the absence of an applied magnetic field the energygap at zero Kelvin (Δ_0) is related to the critical temperature $T_{c,0}$ by $\Delta_0 = 1.764 k T_{c,0}/e$. As the temperature increases, the energy gap reduced, and, in general, both Δ and T_c depend on the applied magnetic field. The BCS-DOS has two distinct and sharp peaks for energies $E = \pm\Delta$. In a strong applied magnetic field H, resulting in a magnetic induction $B = \mu_0 H$, the peaks in the BCS-DOS will Zeeman-split by an amount equal to $E_Z = \pm g\mu_B B$, see Fig. 10.1(a). The two peaks for the spin-up electrons are shifted to lower energies, while the two peaks corresponding to the spin-down electrons are shifted to higher energies. Thus, the density of states of a BCS superconductor in an applied magnetic field has has peaks at the positions $E = \pm\Delta \pm E_Z$.

The tunnel current density $J(V)$ and the differential tunnel conductance $G(V) = dJ/dV$ in a tunnel junction can for low bias voltages be approximated by:

$$J(V) \propto |T|^2 \rho_{NM} \int_{-\infty}^{\infty} dE\, \rho_{BCS}(E)\, [f(E - eV) - f(E)], \qquad (10.2)$$

$$G(V) \propto |T|^2 \rho_{NM} \int_{-\infty}^{\infty} dE\, \rho_{BCS}(E) \left[-e\frac{df(E - eV)}{dE} \right], \qquad (10.3)$$

where $f(E)$ is the Fermi-distribution function. The tunneling matrix element $|T|^2$ and ρ_{NM} are assumed to be constant in the considered energy range. The second factor in the integrand of Eq. (10.3) is a strongly peaked function at $E = eV$, as can be seen in Fig. 10.1(b). Therefore, at each bias voltage, the dynamic conductance G is mainly determined by the BCS-DOS at the corresponding energy $\rho_{BCS}(eV)$. As a result, the peaks in the BCS-DOS translate in corresponding peaks in the dynamic conductance $G(V)$.

For a nonmagnetic counter electrode, the same prefactor $|T|^2 \rho_{NM}$ is independent of spin, and the resulting dynamic conductance curve $G(V)$ is symmetric. However, for a ferromagnetic material, both the tunneling matrix element $|T|^2$ as the DOS ρ_{FM} depend on the electron spin. A tunneling electron spin polarization can be defined as:

$$P = \frac{|T_\uparrow|^2 \rho_{FM,\uparrow} - |T_\downarrow|^2 \rho_{FM,\downarrow}}{|T_\uparrow|^2 \rho_{FM,\uparrow} + |T_\downarrow|^2 \rho_{FM,\downarrow}}. \qquad (10.4)$$

A non-zero polarization results in an asymmetry in the dynamic conductance curves, as shown in Fig. 10.1(c) for a model ferromagnetic material with $P = 67\%$. It is easy to show [58] that the polarization P can be obtained by measuring the four conductances σ_i indicated in Fig. 10.1(c), using the formula:

$$P = \frac{\delta_\downarrow - \delta_\uparrow}{\delta_\downarrow + \delta_\uparrow} \qquad (10.5)$$
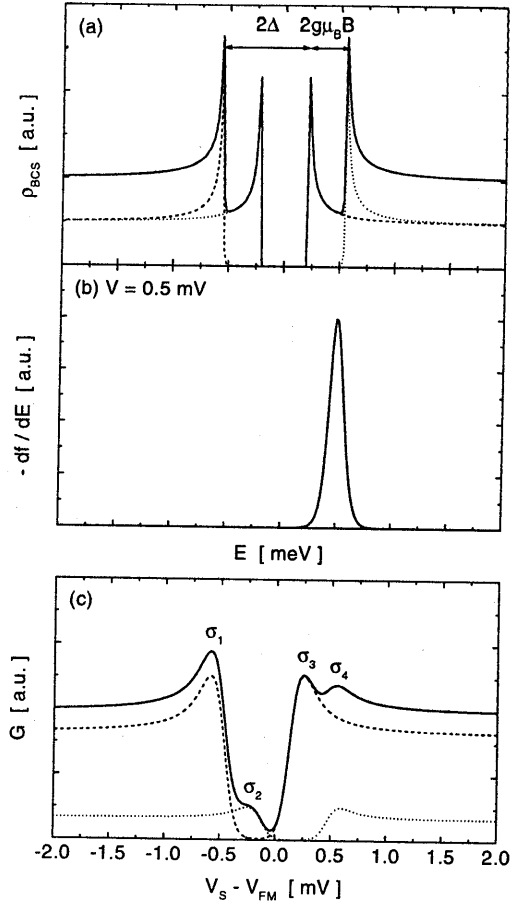
Figure 10.1: Model calculations showing the individual components of the dynamic conductance $G(V)$ curve for a hypothetical ferromagnetic material with a tunneling electron spin polarization $P = 67\%$ and an applied magnetic field $H = 2400$ kA/m, corresponding to a magnetic induction $B = 3$ T. (a) The density of states $\rho_{BCS}(E)$ for an ideal BCS superconductor (no spin-orbit interaction) with a critical temperature $T_{c,0} = 2.5$ K. (b) The derivative $df(E - eV)/dV(E)$ of the Fermi distribution function for $V = 0.5$ V and a temperature $T = 0.5$ K. (c) The full differential conductance curve $G(V)$ according to Eq. (10.3). The dashed (dotted) lines show the individual spin-up (down) contributions to the total (solid line). The conductances σ_i ($i = 1$–4) have been used to obtain the polarization values.
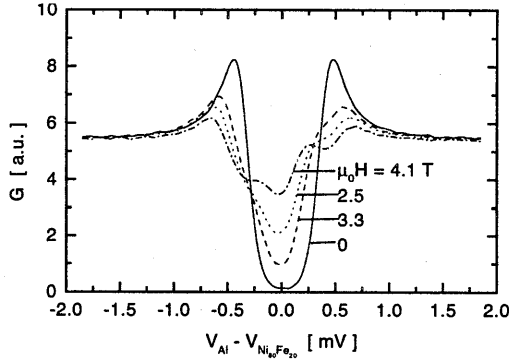
Figure 10.2: Normalized conductance curves obtained for an Al/MgO/$Ni_{80}Fe_{20}$ tunnel junction. The curves are for increasing applied magnetic field of 0.0, 2.5, 3.3, and 4.1 T.

with

$$\delta_\downarrow = \sigma_4 - \sigma_2 \qquad (10.6)$$

$$\delta_\uparrow = \sigma_1 - \sigma_3 \qquad (10.7)$$

All the experimental data presented in next Section have been analysed using Eq. (10.5).

When material used as a superconductor in the experiment does not behave as an ideal BCS-superconductor, deviations from Eq. (10.5) are expected. For instance, the effects of spin-orbit interaction, orbital depairing, and Fermi liquid effects have been reported [58, 119, 120]. For Al_2O_3 based junctions it has been found that these effects cause a relative reduction of about 8% of the measured conduction electron spin polarization [118]. For AlN and MgO barriers comparative data is not yet available. Therefore, all the values for the polarizations reported in the next Section have been corrected for the 8% relative reduction found for Al_2O_3.

10.4 Results and discussion

Fig. 10.2 shows several experimental dynamic conductance curves for an Al–MgO–$Ni_{80}Fe_{20}$ tunnel junction. For the higher magnetic fields, the four peaks in the dynamic conductance curve can be distinguished. For most of the MgO barriers, and several of the AlN barriers, it was observed that the apparent splitting of the conductance peaks was sometimes smaller than expected from the Zeeman splitting. This indicates that the effects of non-ideal BCS-superconductivity in the Al electrodes underneath these two types of barriers are perhaps more pronounced, as a result of the different preparation conditions (nitrogen instead of oxygen, Mg instead of Al, different thickness of the remaining Al electrode after barrier formation).

All obtained results have been summarized in Table 10.1. In general, the observed conduction electron spin polarization reduces only by a small amount for AlN barriers

Table 10.1: Polarization of Ni, Fe, Co, and some $Ni_{1-x}Fe_x$ and $Co_{1-x}Fe_x$ alloys obtained with *in-situ* glow discharge formed Al_2O_3, AlN, and MgO barriers. The results have reduced by 8% in order to correct for the non-ideal BCS-like charateristics of the Al superconductor, as explained in the text. All materials have been thermally evaporated by e-gun, unless otherwise indicated. The parameter x was determined by XRF analysis of 20-nm-thick evaporated films.

	$P(Al_2O_3)$ [%]	$P(AlN)$ [%]	$P(MgO)$ [%]
Ni	27	23	
$Ni_{86}Fe_{14}$	33	43	34
$Ni_{78}Fe_{22}$[a]	45		41
$Ni_{74}Fe_{26}$	46		
$Ni_{59}Fe_{41}$	48	35	
$Ni_{47}Fe_{53}$	52		
$Ni_{30}Fe_{70}$	51		
$Ni_{25}Fe_{75}$	40	33	
$Ni_{17}Fe_{83}$	49		
$Ni_{12}Fe_{88}$	50	34	
Ni_4Fe_{96}	45		
Fe	41	39	
$Co_{50}Fe_{50}$	51	50	33
$Co_{84}Fe_{16}$	49	46	
Co	45	35	46

[a]evaporated from W-boat

compared to Al_2O_3 barriers. The samples (mostly for MgO barriers) showing also a reduced Zeeman splitting, also showed large reductions of the polarization (these data have not been included in the table). Whether this was an intrinsic effect of the barrier material is uncertain, but it is more likely the result of an unoptimized barrier preparation process. One of the possible extrinsic causes is an increased spin scattering at the interface between the superconductor and the insulator. For a clean Al-Al_2O_3 and Al-AlN interface this is expected bo be lower than for the Al-MgO interface, where some residual Mg might still be present after the oxidation step. Also, as a consequence of the MgO barrier being formed from additionally deposited Mg, the thickness of the Al layer in the MgO junctions is larger than for the corresponding Al_2O_3 or AlN junctions. Also the AlN barriers are slightly thinner than Al_2O_3 barriers, as indicated by the lower resistance. One effect of a changing thiockness of the superconductor is via orbital depairing, which scales with the square of the Al layer thickness [119]. Orbital depairing couples the two spin directions and thereby smudges the BCS-like features. This results in a larger correction factor and, therefore, a lower polarization. As a consequence, when thinner Al starting layers were used for the AlN barriers, the polarization values became comparable to those found for Al_2O_3.

Fig. 10.3 shows a comparison of the present experimental data for the $Ni_{1-x}Fe_x$ data with Al_2O_3 barriers with similar data from Paraskevopoulos *et al.* [118]. For all the $Ni_{1-x}Fe_x/Al_2O_3$ junctions the presently obtained polarizations are higher than previously reported for *ex-situ* water vapor formed Al_2O_3 barriers [118]. A similar im-
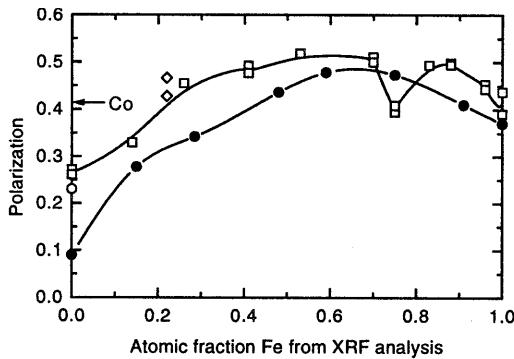
Figure 10.3: Overview of the polarization results for $Ni_{1-x}Fe_x$ alloys. Various results are plotted: (•) results of Refs. [58, 118] using *ex-situ* H_2O-vapor formed barriers, (○) result of Ni with *in-situ* O_2 glow discharge formed barrier [121], and present results with (□) e-gun evaporated and (◇) W-boat evaporated alloys. The result for Co is indicated with an arrow. The lines are guides to the eye.

provement was found for Ni by Moodera *et al.* [121] and is attributable to improved barrier preparation and a cleaner FM-I interface. It also appears that the effect of the surface cleanliness is more important for the Ni rich alloys. Also, the previously reported correspondence between the value of the polarization and the value of the saturation magnetic moment [118] could not be reproduced, as the present experiments show only a week dependence on composition, except for the Ni rich alloys. This week dependence has been confirmed by independent Andreev reflection experiments [122–124] performed by Soulen *et al.* [125] on samples prepared in the same evaporation system.

Note the lower polarization value of the $Ni_{25}Fe_{75}$ alloy in Fig. 10.3, compared to the values of the surrounding alloys. Although it might be an experimental artifact, the composition is in the range of compositions for which a transformation from bcc crystal structure for Fe richer to fcc crystal structure for Ni richer alloys has been reported. Calculations, by for instance Williams *et al.* [126], suggest that at the transition the magnetic moment of the alloy may be reduced, or even disappear.

10.5   Conclusions

In conclusion, the polarization values obtained for $Ni_{1-x}Fe_x$ alloys using an *in-situ* glow discharge oxidized barrier preparation method are larger than previously reported values obtained using *ex-situ* water vapor oxidized barriers and vary only slightly on alloy composition. The difference can be attributed to the progress in preparation conditions, resulting in cleaner barrier-electrode interfaces. For Ni-rich alloys, the polarization is lower than for Fe-rich alloys, which seems to indicate that Ni is more susceptible to interface cleanliness. The obtained results for the Al_2O_3 and AlN barriers are similar, while for most MgO samples the polarization was suppressed, most likely as a result of non-ideal sample structure. The previously reported relation between the saturation

magnetic moment and the polarization could not be reproduced.

Chapter 11

Discussion and Outlook

In this Chapter the results obtained in Part II will be briefly summarized, compared to literature results, and future experiments will be suggested. The reader should bear in mind, however, that many of the ideas put forward in this thesis are the result of a limited set of experiments, most of them electron transport measurements. Therefore, further experiments are called for, often involving characterization techniques suitable to study one specific aspect. Furthermore, it should be noted that the work presented in this thesis is complemented by the work in many other groups. It is surprising to note that, despite all the new, more detailed, and in many ways improved experimental observations and model calculations, the clear and simple picture presented by Julliere [15] in 1975 is still holding.

11.1 About the preparation

The key to the present success of magnetic tunnel junctions is the advance in preparation methods. We have shown that junction magnetoresistance devices can be reproducibly prepared by thermal evaporation onto cooled substrates using shadow mask technology, in combination with glow-discharge oxidation to prepare an Al_2O_3 barrier. However, different approaches on almost every aspect of the preparation technique have now been reported in the literature, many resulting in tunnel junctions with reasonably good properties.

For the deposition of the starting materials, numerous other groups have used sputter deposition at room temperature as their method of deposition, as this is the preferred preparation method for industrial applications. The differences between sputter deposition and evaporation are related to the details of the deposition process, like, for instance, the kinetic energy of the deposited atoms, the growth rate, and the surface mobility. Both techniques seem to give comparable, but not identical results. For instance, by comparing the IETS experiments presented in Chapter 7 with similar measurements on sputter deposited junctions [127], it follows that while during deposition of the top electrode using sputtering magnetic atoms diffuse or penetrate into the barrier, where

they give rise to magnetic impurity states, the corresponding IETS peaks are absent for the evaporated junctions. In addition to both vacuum deposition techniques, it is worth mentioning that Doudin *et al.* [128] have reported the first results on Ni–NiO–Co tunnel devices prepared by electrodeposition. Even though in general this preparation method is less flexible, some specific advantages make it an interesting alternative approach. For instance, by growing tunnel junctions directly in the pores of ceramic filters, small area junctions can be prepared without the need for additional microfabrication.

Also for the barrier preparation various techniques have been successfully employed. Most abundantly used, in several variations, is the glow-discharge oxidation method also used in this thesis. However, the various glow-discharge geometries in use differ in details, such that a process of tedious and extensive testing is required before satisfactory results can be obtained, and comparison of the experimental parameters is virtually useless. Despite the optimization needed for each glow-discharge geometry, such as the applied dc or ac voltages, the oxygen pressure, and the duration of oxidation, the oxidation process itself seems rather robust and seems fairly easy to implement. For tunnel junctions of lateral dimensions in the range of a few to several hundred μm, the glow-discharge oxidation method is ideal, in the sense that the obtained junction resistance is in an experimentally easily accessible regime, i.e., high enough (i.e., the junction resistances larger than the square resistance of the electrodes) to avoid the contact resistance problems as discussed in Chapter 5, and low enough for the most commonly available equipment. Junctions in the envisioned applications, however, will have dimensions in the submicron regime. For these applications, the conductance per unit area of the present glow-discharge oxidized junctions is too low, even for the thinnest barriers and a very mild oxidation. Problems arise in terms of the shot noise (equivalent to Johnson noise for $eV < kT$), and the unavoidable delay time resulting from the product of the resistance of the junction and the sum of the capacitance of the tunnel junction an the stray capacitance of the contact leads and electronics.

Various oxidation processes have been reported which result in higher conducatance per unit area. In most of the alternative processes, a metallic Al layer is thermally oxidized in an oxygen environment, which usually takes a much longer time (hours to weeks) compared to glow-discharge oxidation (seconds to minutes). Various approaches have been suggested to increase to oxidation rate, among others, using ozone instead of oxygen or using UV-light to dissociate oxygen molecules, both creating more chemically active oxygen. Another alternative uses a multistep process, in which the barrier layer is built-up in several sequences of deposition of a thin Al layer and thermal oxidation [20, 129]. Reactive deposition of the barrier material, i.e., depositing the barrier material in a background oxygen pressure, can be viewed upon as the ultimate multistep process. Due to the intentionally high conductance of these tunnel junctions, reliable transport measurements on these junctions can only be performed on microfabricated junctions or by using superconducting contacts at low temperatures (this is a mild version of a similar problem presented by the measurement of the magnetoresistance of metallic multilayers in the current-perpendicular-to-plane geometry [130]).

By depositing the bottom electrode and the metallic Al barrier material onto cryogenically cooled substrates, the surface roughness and diffusion processes were reduced. Using this approach, a homogeneous coverage of the bottom electrode is ob-

tained, resulting later in the preparation of a closed barrier layer without metallic pin-holes. This is important, since the tunnel conductance depends exponentially on the barrier layer thickness, resulting in large local conductance variations for rough barriers. From the good reproducibility of the resistance of nominally identical devices prepared in one process, we conclude that the use of a cooled substrate leads to relatively small lateral variations in the barrier thickness, and that we may consider our junction homogeneous in this sense. This conclusion is not only valid for the lateral dimensions of the *in-situ* fabricated junctions presented in this thesis (order 200 μm). The area scaling of the resistance of *ex-situ* microfabricated junctions, starting from the same stack [131], indicates that this conclusion can be extended to lengthscales down to about 4 μm. Other groups, see for instance [19, 132], using e-beam lithography and sputtered deposited tunnel junctions stacks, have shown that the areal scaling of the resistance continues down to lateral dimensions of the order of 0.1 μm.

The statistics of the conductance variations as a result of barrier thickness variations was predicted by Bardou [133] and was experimentally tested by Watanabe *et al.* [134] for a SiO_2 layer and by Da Costa *et al.* [135] for a CoO layer. The latter experiments seem to indicate that below 0.1 μm dimensions the area scaling will break down, although this will depend critically on the preparation conditions. Another consequence of roughness is related to dielectric breakdown of the junction, i.e., irreversible failures occur at lower voltages for rougher barriers, see for instance [55, 136, 137]. There are also indications that the amplitude of the $1/f$ noise in magnetic tunnel junctions is solely determined by the amount of "hot spots," without any magnetic contribution (this in contrast to the results for metallic magnetic systems as presented in Part I), see for instance [138, 139].

The details of the preparation process, and the influence of the various parameters on the result, has not yet been thoroughly understood. Specifically, more effort needs to be focussed on studies of the barrier formation process itself, since very little is known for these thin layers. Several groups have initiated research on this subject, using either *in-situ* or *ex-situ* surface sensitive and element specific spectroscopic characterization techniques like XPS, Auger, and RBS. Images taken with high resolution transmission electron microscopes show that of the various barrier materials studied so far, some result in an amorphous layer, while others form a crystalline layer. See for instance [140]. Although these characterization measurements are just starting, already a wealth of additional information has become available. A more detailed discussion about these techniques can be found in [55].

11.2   Discussion of the Results

As the most important conclusion of Part II of this thesis, the results of Chapters 4, 6, 8, and 9 all indicate that the interface region surrounding the insulating barrier is of extreme importance for the magneto-transport properties of magnetic tunnel junctions. In Chapter 8 and 9, this influence is observed even at low temperatures, and can be satisfactory understood in terms of model predictions taking into account elastic tunneling processes only. The most dramatic effect is found for tunnel junctions

with an additional nonmagnetic Au interface layer, as presented in Chapter 9, which showed a negative magnetoresistance for Au layer thicknesses of 0.6 and 0.7 nm. For the same junctions, also an extreme asymmetry of the bias voltage dependence was observed, including several sign reversals. These experiments can be interpreted in terms of quantum well states, i.e., for certain voltages or layer thicknesses tunneling electrons at the Fermi level of one of the spin channels fullfil a resonance condition in the nonmagnetic layer, which results in an increase of the tunnel conduction. This, in turn, changes the magneto-transport properties. The subject of nonmagnetic interface layers is hotly debated during conferences, both experimentally as theoretically, although little has been published yet. There are marked differences between the results obtained for sputtering compared to evaporated junctions, for which no accepted explanation is given. This will become an active area of research in the immediate future, also as a result of the possible technological advantages of such an interface layer, for instance as a oxidation barrier or to reduced magnetic orange peel coupling.

For the temperature dependence of the junction magnetoresistance, as discussed in the Chapters 4, 6, and 8, however, models based on elastic tunneling alone are insuffucient to explain the observations. In addition to elastic tunneling, inelastic tunneling, upon which spin-waves are excited or absorbed in the magnetic interface layer, plays an important role. A large portion of the experimentally observed temperature dependence of the magnetoresistance (at zero applied bias voltage and in the temperature range between zero Kelvin and room temperature) can be explained on the basis of this effect, as discussed in Chapter 6. Low energy spin-wave states are available and can mediate inelastic tunneling processes at non-zero bias voltages, as has clearly been demonstrated in Chapter 7, or at elevated temperatures. In addition, at elevated temperatures spin-waves also influence the magnetization and/or the magnetic configuration of the electrodes. Both the inelastic spin-wave conductance contribution (with a magnetoresistance contribution of the opposite sign) and the distorted magnetic configuration (via a non-ideal magnetization alignment) lead to an additional reduction of the magnetoresistance at elevated temperatures. In this respect, it would be of fundamental interest to perform detailed temperature and voltage dependent measurements on magnetic tunnel junctions using a low Curie temperature material like Gd, in combination with a properly oxidized Al_2O_3 barrier. Both effects are predicted to be less effective for thermally more stable magnetic interface layers, which may be achieved by increasing the Curie temperature of the material, or by introducing magnetic anisotropy. On the other hand, from the IETS experiments presented in Chapter 7, it was found that the energy needed for *phonon* excitation corresponds to temperatures above room temperature. Thus, the opening of new conductance channels due to inelastic electron-phonon scattering processes may be safely neglected when considering the temperature dependence of the tunnel conductance (at zero bias voltage).

Just as in the case of the temperature dependence, part of the reduced junction magnetoresistance at applied bias voltages, especially the sharp initial decrease at low applied voltages, can not be understood within models including elastic tunneling only, as has been shown in Chapter 4. Model calculations, see for instance [89, 108], argue that again spin-waves are relevant for the additional decrease. Therefore, also the bias voltage dependence will improve when more stable magnetic interface layers are used.

Indirect evidence for this prediction can be found from the experiments described in Chapter 8, where it was found that for overly oxidized tunnel junctions the bias voltage dependence is much steeper, in addition to a dramatic temperature dependence. The temperature dependence has been interpreted as resulting from an interface layer of CoO, which is an antiferromagnet with an ordering temperature just below room temperature. When the junction is warmed through this ordering temperature, the magnetoresistance is found to disappear, apparently as a result of the loose spin-structure of the paramagnetic CoO. The bias voltage dependence has not been modeled. However, the weaker magnetic exchange interactions in the CoO as compared to Co may be part of the explanation.

It should be noticed that for many of the early experiments, the barrier layer consisted of the native oxides of NiO, CoO, or GdO_x. All these substances are antiferromagnetic, with relatively low ordening temperatures. This may explain, in analogy with the experiments of the overly oxidized junctions in Chapter 8, why a sizable magnetoresistance was sometimes obtained at low temperatures, while at room temperature no effect was measureable. Only with the introduction of Al_2O_2 barriers by Moodera *et al.* [16] and Miyazaki *et al.* [17], large magnetoresistance effects at room temperature were observed.

11.3   Novel Materials

According to Eq. (3.4), the magnetoresistance is determined by the tunneling electron spin polarization, which has a specific value for each electrode material, potentially in combination with a specific barrier material. In Chapter 10 results of direct measurements of this polarization value have been presented for a number of metallic transition metal alloys. From the initial model calculations of Slonczewski [51], it is known that this polarization value is not solely determined by the bulk properties of the ferromagnet, but indeed also contains a factor containing the matching of electrode and barrier wave-functions at the interface. However, from the presented experiments using three different barrier materials, no positive observation of such a dependency can be claimed, as plausible experimental artifacts might also account for the observed differences. The highest observed polarization (at 0.5 K) was about 50% for a range of alloy compositions containing Fe and either Co or Ni. For two electrodes with a polarization of 50%, a magnetoresistance ratio $\Delta R/R_{AP} = 67\%$, or $\Delta R/R_P = 40\%$, is predicted. This value is higher than any reliable value reported so far for a junction based on magnetic $3d$ transition metal materials or their alloys. However, in view of the constant increase of the reported values of the magnetoresistance and the increasing polarizations as a result of cleaner preparation conditions, even higher magnetoresistance ratios seem possible.

On the other hand, the transition metals and their alloys do not have the highest known polarizations. Several classes of halfmetallic ferromagnets (HMF) exist, i.e., materials which conduct electrons of only one spin direction [141–143]. The most well known class of HMFs are the Heussler alloy compounds, of which NiMnSb is the prototypical example. Recently, tunnel junctions containing NiMnSb as one of the electrodes have been successfully prepared [144, 145]. The results, however, indicate that

the material used is not halfmetallic, plausibly as a consequence of a non-stoichiometric electrode-barier interface.

A second hotly persued class of HMFs is the group of CMR materials, more specifically the mixed valence manganese perovskites. Calculations have predicted, and photoemission experiments have shown [146], that many CMR compounds behave as HMFs in their low temperature, ferromagnetic phase. The cause is the hopping conduction mechanism, whereby a localized electron of one specific spin hops between Mn^{3+} and Mn^{4+} ions [147]. Large magnetoresistance ratios have been obtained using these compounds in epitaxial all oxide tunnel junctions. See for instance [148] for a review of these experiments. The drawback of these materials is the low Curie temperature, which is around room temperature. Therefore, large magnetoresistance effects have only been obtained at low temperature and are not expected to be raised to room temperature. Another mixed valence compound, the inverse spinel magnetite, or Fe_3O_4, is also expected to be halfmetallic, but with a Curie temperature of 860 K. This property makes this compound favorable over the manganese perovskite compounds as an electrode material, and has been tried by several groups, see for instance Li et al. [149], including our own. In fact, the perspective for magnetic tunnel junctions offered by the half-metallic characted of this compound was the initial motivation for performing the study that has led to this thesis. However, no large magnetoresistance values have been observed to date, most likely due to problems with the interface.

For the metallic junctions, most groups are presently optimizing the electrode composition, for instance by adding high Curie temperature interface layers. However, in view of the predicted dependence of the polarization on an interface matching term [51], improvements might also be gained from the use of other barrier materials. The barrier material of choice is almost exclusively Al_2O_3. Only few other nonmagnetic barrier materials, among others AlN, HfO_2, and MgO, have been tried, and hardly any optimization has been performed for these materials. Especially for AlN, junctions with large magnetoresistance ratios have been prepared, with high conductances per unit area. The process to prepare AlN is similar to that of Al_2O_3, but with the additional advantage of a slower growth rate, hence more control and possibly better homogeneity. A positive side effect is that overly nitridized barriers will not form paramagnetic materials like CoO or NiO, which have been shown to be detrimental to the junction performance.

A completely different approach can be taken using organic barrier materials. Self Assembled Monolayers using molecules of defined length may prove to be an ideal barrier material, at least from the point of view of roughness and barrier homogeneity. A first attempt has been reported by Ando et al. [150], which showed that many preparational problems have yet to be overcome. Whether the properties of these barrier materials is comparable to those of solid state barriers remains to be investigated.

Bibliography

[1] P. F. Carcia, A. D. Meinhaldt, and A. Suna, Appl. Phys. Lett. **47**, 178 (1985).

[2] P. Grünberg, R. Schreiber, Y. Pang, M. B. Brodsky, and H. Sowers, Phys. Rev. Lett. **57**, 2442 (1986).

[3] M. N. Baibich, J. M. Broto, A. Fert, F. Nguyen Van Dau, F. Petroff, P. Etienne, G. Cruezet, A. Friederich, and J. Chazelas, Phys. Rev. Lett. **61**, 2472 (1988).

[4] G. Binasch, P. Grünberg, F. Saurenbach, and W. Zinn, Phys. Rev. B **39**, 4828 (1989).

[5] W. Thomson, Proc. Roy. Soc. **8**, 546 (1857).

[6] T. R. McGuire and R. I. Potter, IEEE Trans. Magn. **MAG–11**, 1018 (1975).

[7] J. P. Heremans, Mat. Res. Soc. Symp. Proc. **475**, 63 (1997).

[8] G. H. Jonker and J. H. van Santen, Physica **16**, 337 (1950).

[9] R. von Helmont *et al.*, Phys. Rev. Lett. **71**, 2332 (1993).

[10] K. Chahara, T. Ohno, M. Kasai, and Y. Kozono, Appl. Phys. Lett. **63**, 1990 (1993).

[11] S. Jin, T. H. Tiefel, M. McCormack, R. A. Fastnach, R. Ramesh, and L. H. Chien, Science **264**, 413 (1994).

[12] Y. Shimakawa, Y. Kubo, and T. Manako, Nature **379**, 53 (1996).

[13] M. A. Subramanian, B. H. Toby, A. P. Ramirez, W. J. Marshall, A. W. Sleight, and G. H. Kwei, Science **273**, 81 (1996).

[14] A. P. Ramirez and M. A. Subramanian, Science **277**, 546 (1997).

[15] M. Julliere, Phys. Lett. **54A**, 225 (1975).

[16] J. S. Moodera, L. R. Kinder, T. M. Wong, and R. Meservey, Phys. Rev. Lett. **74**, 3273 (1995).

[17] T. Miyazaki and N. Tezuka, J. Magn. Magn. Mater. **139**, L231 (1995).

[18] M. Sato and K. Kobayashi, Jpn. J. Appl. Phys. **36**, L200 (1997).

[19] W. J. Gallagher, S. S. P. Parkin, Y. Lu, X. P. Bian, A. Marley, K. P. Roche, R. A. Altman, S. A. Rishton, C. Jahnes, T. M. Shaw, and G. Xiao, J. Appl. Phys. **81**, 3741 (1997).

[20] H. Tsuge and T. Mitsuzuka, Appl. Phys. Lett. **71**, 3296 (1997).

[21] B. Dieny, V. S. Speriosu, S. S. P. Parkin, B. A. Gurney, D. R. Wilhoit, and D. Mauri, Phys. Rev. B **43**, 1297 (1991).

[22] T. G. S. M. Rijks, W. J. M. de Jonge, W. Folkerts, J. C. S. Kools, and R. Coehoorn, Appl. Phys. Lett. **65**, 916 (1994).

[23] P. Ripka, Sensors and Actuators A **41–42**, 394 (1994).

[24] C. Tsang, J. Appl. Phys. **55**, 2226 (1984).

[25] K. E. Kuijk, W. J. van Gestel, and F. W. Gorter, IEEE Trans. Magn. **MAG-11**, 1215 (1975).

[26] F. N. Hooge, T. G. M. Kleinpenning, and L. K. J. Vandamme, Rep. Prog. Phys. **44**, 31 (1981).

[27] P. Dutta and P. M. Horn, Rev. Mod. Phys. **53**, 497 (1981).

[28] M. B. Weissman, Rev. Mod. Phys. **60**, 537 (1988).

[29] H. T. Hardner, M. B. Weissman, M. B. Salomon, and S. S. P. Parkin, Phys. Rev. B **48**, 16156 (1993).

[30] H. T. Hardner, S. S. P. Parkin, M. B. Weissman, M. B. Salomon, and E. Kita, J. Appl. Phys. **75**, 6531 (1994).

[31] H. T. Hardner, M. B. Weissman, and S. S. P. Parkin, Appl. Phys. Lett. **67**, 1938 (1995).

[32] H. T. Hardner, M. B. Weissman, B. Miller, R. Loloee, and S. S. P. Parkin, J. Appl. Phys. **79**, 7751 (1996).

[33] L. S. Kirschenbaum, C. T. Rogers, S. E. Russek, and S. C. Sanders, IEEE Trans. Magn. **31**, 3943 (1995).

[34] M. A. M. Gijs, J. B. Giesbers, J. W. van Est, J. Briare, L. K. J. Vandamme, and P. Beliën, J. Appl. Phys. **80**, 2539 (1996).

[35] M. A. M. Gijs, J. B. Giesbers, P. Beliën, J. W. van Est, and L. K. J. Vandamme, J. Magn. Magn. Mater. **165**, 360 (1997).

[36] J. C. S. Kools, J. J. M. Ruigrok, B. Postma, M. C. de Nooijer, and W. Folkerts, IEEE Trans. Magn. **33**, 4513 (1997).

[37] J. McCord, A. Hubert, J. C. S. Kools, and M. C. de Nooijer, IEEE Trans. Magn. **32**, 4803 (1996).

[38] F. N. Hooge, Phys. Lett. **29A**, 139 (1969).

[39] K. Fuchs, Proc. Cambridge Philos. Soc. **34**, 100 (1938).

[40] E. H. Sondheimer, Adv. Phys. **1**, 1 (1952).

[41] T. G. S. M. Rijks, R. F. O. Reneerkens, R. Coehoorn, and W. J. M. de Jonge (unpublished).

[42] M. F. Gillies, J. N. Chapman, and J. C. S. Kools, J. Appl. Phys. **78**, 5554 (1995).

[43] R. V. Chamberlain, J. Appl. Phys. **76**, 6401 (1994).

[44] R. V. Chamberlain and M. R. Scheinfein, Science **260**, 1098 (1993).

[45] T. G. S. M. Rijks, R. Coehoorn, J. T. F. Daemen, and W. J. M. de Jonge, J. Appl. Phys. **76**, 1092 (1994).

[46] H. Hoffmann, IEEE Trans. Magn. **MAG-4**, 32 (1968).

[47] J. G. Simmons, J. Appl. Phys. **34**, 1793 (1963).

[48] W. F. Brinkman, R. C. Dynes, and J. M. Rowell, J. Appl. Phys. **41**, 1915 (1970).

[49] P. M. Tedrow and R. Meservey, Phys. Rev. Lett. **26**, 192 (1971).

[50] S. Maekawa and U. Gäfvert, IEEE Trans. Magn. **MAG–18**, 707 (1982).

[51] J. C. Slonczewski, Phys. Rev. B **39**, 6995 (1989).

[52] I. Giaever and K. Megerle, Phys. Rev. **122**, 1101 (1961).

[53] S. Shapiro, Phys. Rev. Lett. **11**, 80 (1963).

[54] J. L. Miles and P. H. Smith, J. Elec. Soc. **110**, 1240 (1963).

[55] W. Oepts, Ph.D. thesis, Eindhoven University of Technology, Department of Physics, Eindhoven, The Netherlands, 1999.

[56] J. M. Daughton, J. Appl. Phys. **81**, 3758 (1997).

[57] M. B. Stearns, J. Magn. Magn. Mater. **5**, 167 (1977).

[58] R. Meservey and P. M. Tedrow, Phys. Rep **238**, 173 (1994).

[59] T. Miyazaki, T. Yaoi, and S. Ishio, J. Magn. Magn. Mater. **98**, L7 (1991).

[60] J. Inoue and S. Maekawa, Phys. Rev. B **53**, R11927 (1996).

[61] S. T. Chui, Phys. Rev. B **55**, 5600 (1997).

[62] A. M. Bratkovsky, Phys. Rev. B **56**, 2344 (1997).

[63] X. Zhang, B.-Z. Li, G. Sun, and F.-C. Pu, Phys. Rev. B **56**, 5484 (1997).

[64] J. Mathon, Phys. Rev. B **56**, 11810 (1997).

[65] J. M. MacLaren, X. G. Zhang, and W. H. Buttler, Phys. Rev. B **56**, 11827 (1997).

[66] J. S. Moodera, E. F. Gallagher, K. Robinson, and J. Nowak, Appl. Phys. Lett. **70**, 3050 (1997).

[67] K. Knorr and J. D. Leslie, Sol. State Comm. **12**, 615 (1973).

[68] E. L. Wolf, in *Principles of Electron Tunneling Spectroscopy*, Vol. 71 of *International Series of Monographs on Physics*, edited by R. J. Elliot, J. A. Krumhansl, W. Marshall, and D. H. Wilkinson (Oxford University Press, New York, 1985).

[69] J. A. Applebaum, Phys. Rev. **154**, 633 (1967).

[70] D. C. Tsui, R. E. Dietz, and L. R. Walker, Phys. Rev. Lett. **27**, 1729 (1971).

[71] D. L. Mills and A. A. Maradudin, J. Phys. Chem. Solids **28**, 1855 (1967); J. Mathon and S. B. Ahmad, Phys. Rev. B **37**, 660 (1988).

[72] D. T. Pierce, R. J. Celotta, J. Unguris, and H. C. Siegman, Phys. Rev. B **26**, 2566 (1982).

[73] D. Mauri, D. Scholl, H.C. Siegmann, and E. Kay, Phys. Rev. Lett. **61**, 758 (1988).

[74] E. Kay, Mater. Res. Soc. Symp. Proc. **151**, 77 (1989).

[75] G. Rossi, F. Sirotti, and G. Panaccione, Mater. Res. Soc. Symp. Proc. **384**, 447 (1995).

[76] C. L. Platt, B. Dieny, and A. E. Berkowitz, Appl. Phys. Lett. **69**, 2291 (1996).

[77] J. S. Moodera, R. Meservey, and X. Hao, Phys. Rev. Lett. **70**, 853 (1993).

[78] R. Jansen and J. S. Moodera, J. Appl. Phys. **83**, 6682 (1998).

[79] J. S. Moodera, L. R. Kinder, J. Nowak, P. LeClair, and R. Meservey, Appl. Phys. Lett. **69**, 708 (1996).

[80] S. Kumagai, T. Yaoi, and T. Miyazaki, J. Magn. Magn. Mater. **166**, 71 (1997).

[81] T. Miyazaki, S. Kumagai, and T. Yaoi, J. Appl. Phys. **81**, 3753 (1997).

[82] I. Giaever, *Tunneling Phenomena in Solids*, edited by Burnstein (1967), p 27.

[83] R. J. Pedersen and J. Vernon, F. L., Appl. Phys. Lett. **10**, 29 (1967).

[84] S. K. J. Lenczowski, R. J. M. van de Veerdonk, M. A. M. Gijs, J. B. Giesbers, and H. H. J. M. Janssen, J. Appl. Phys. **75**, 5154 (1994).

[85] M. A. M. Gijs and R. M. Wolf and Th. van Rooy and A. M. Gerrit and M. E. Bijlsma and A. Gilabert, Sol. State Comm. **80**, 727 (1991).

[86] J. S. Moodera *et al.*, unpublished results.

[87] J. S. Moodera, J. Nowak, and R. J. M. van de Veerdonk, Phys. Rev. Lett. **80**, 2941 (1998).

[88] C. H. Shang, J. Nowak, R. Jansen, and J. S. Moodera, Phys. Rev. B **58**, R2917 (1998).

[89] S. Zhang, P. M. Levy, A. C. Marley, and S. S. P. Parkin, Phys. Rev. Lett. **79**, 3744 (1997).

[90] C. Kittel, *Introduction to Solid State Physics*, sixth ed. (John Wiley & Sons, New York, U.S.A., 1986).

[91] N. W. Ashcroft and N. D. Mermin, *Solid State Physics*, international edition ed. (Saunders College, Philadelphia, U.S.A., 1976).

[92] J. Mathon and S. B. Ahmad, Phys. Rev. B **37**, 660 (1988).

[93] D. Scholl, M. Donath, D. Mauri, E. Kay, J. Mathon, R. B. Muniz, and H. C. Siegman, Phys. Rev. B **43**, 13309 (1991).

[94] A. H. MacDonald, T. Jungwirth, and M. Kasner, Phys. Rev. Lett. **81**, 705 (1998).

[95] L. I. Glazman and K. A. Matveev, Zh. Eksp. Teor. Fiz. **94**, 332 (1988) [Sov. Phys. Semicond. **22**, 401 (1988)].

[96] R. Meservey, P. M. Tedrow, and J. S. Brooks, J. Appl. Phys. **53**, 1563 (1982).

[97] G. A. Gibson and R. Meservey, J. Appl. Phys. **58**, 1584 (1985).

[98] Y. Xu, D. Ephron, and M. R. Beasley, Phys. Rev. B **52**, 2843 (1995).

[99] F. Guinea, Phys. Rev. B **58**, R9212 (1998).

[100] S. Zhang, private communication.

[101] J. Inoue and S. Maekawa, unpublished results.

[102] O. I. Shklyarevskii, I. K. Yanson, and V. D. Zaporozhskii, Sol. State Comm. **14**, 327 (1974).

[103] S. Zhang and P. M. Levy, Phys. Rev. Lett. **81**, 5660 (1998).

[104] J. Nassar, M. Hehn, A. Vaurès, F. Petroff, and A. Fert, Appl. Phys. Lett. **73**, 698 (1998).

[105] The parameters values depend on the fitting range, but the trends are always the same. The asymmetric barrier model of Brinkman [W. F. Brinkman, R. C. Dynes, and J. M. Rowell, J. Appl. Phys. **41**, 1915 (1970)] yielded slightly better fits, although we do not show the results here.

[106] A. A. Smits, C. J. P. M. van Nuenen, R. J. M. van de Veerdonk, J. S. Moodera, H. J. M. Swagten, and W. J. M. de Jonge, unpublished results.

[107] M. van Kampen, R. J. M. van de Veerdonk, and A. A. Smits, unpublished results.

[108] A. M. Bratkovsky, Appl. Phys. Lett. **72**, 2334 (1998).

[109] R. J. M. van de Veerdonk, J. Nowak, R. Meservey, J. S. Moodera, and W. J. M. de Jonge, Appl. Phys. Lett. **71**, 2839 (1997).

[110] A. Vedyayev, N. Ryzhanova, C. Lacroix, L. Giacomoni, and B. Dieny, Europhys. Lett. **39**, 219 (1997).

[111] W.-S. Zhang, B.-Z. Li, X. Zhang, and Y. Li, J. Appl. Phys. **83**, 5332 (1998).

[112] Y. Lu, X. W. Li, G. Xiao, R. A. Altman, W. J. Gallagher, A. Marley, K. Roche, and S. Parkin, J. Appl. Phys. **83**, 6515 (1998).

[113] J. J. Sun, R. C. Sousa, T. T. P. Galvão, V. Soares, T. S. Plaskett, and P. P. Freitas, J. Appl. Phys. **83**, 6694 (1998).

[114] J. S. Moodera, M. E. Taylor, and R. Meservey, Phys. Rev. B **40**, R11980 (1989).

[115] In magnetic metallic multilayers a comparable aliasing scheme has been introduced, see for instance R. Coehoorn, Phys. Rev. B **44**, 9331 (1991).

[116] J. Zhang and R. M. White, J. Appl. Phys. **83**, 6512 (1998).

[117] X. Wang, J. Appl. Phys. **83**, 6518 (1998).

[118] D. Paraskevopoulos, R. Meservey, and P. M. Tedrow, Phys. Rev. B **16**, 4907 (1977).

[119] P. Fulde, Adv. Phys. **22**, 667 (1973).

[120] J. A. X. Alexander, T. P. Orlando, D. Rainer, and P. M. Tedrow, Phys. Rev. B **31**, 5811 (1985).

[121] J. S. Moodera, R. Meservey, and P. M. Tedrow, Appl. Phys. Lett. **41**, 488 (1982).

[122] M. J. M. de Jong and C. W. J. Beenakker, Phys. Rev. Lett. **74**, 1657 (1995).

[123] R. J. Soulen, Jr, J. M. Byers, M. S. Osofsky, B. Nadgorny, T. Ambrose, S. F. Cheng, P. R. Broussard, C. T. Tanaka, J. Nowak, J. S. Moodera, A. Barry, and J. M. D. Coey, Science **282**, 85 (1998).

[124] S. K. Upadhyay, A. Palanisami, R. N. Louie, and R. A. Buhrman, Phys. Rev. Lett. **81**, 3247 (1998).

[125] R. J. Soulen, Jr., B. Nadgorny, M. S. Osofsky, I. Mazin, T. Ambrose, S. F. Cheng, E. F. Skelton, S. Qadri, J. Byers, G. Laprade, R. J. M. van de Veerdonk, and J. S. Moodera, unpublished results.

[126] A. R. Williams, V. L. Moruzzi, C. D. Gelatt, Jr., and J. Kübler, J. Magn. Magn. Mat. **31–34**, 88 (1983).

[127] Y. Ando, J. Murai, and T. Miyazaki, J. Magn. Magn. Mater. (1998), to be published.

[128] B. Doudin, G. Redmond, S. E. Gilbert, and J. -Ph. Ansermet, Phys. Rev. Lett. **79**, 933 (1997).

[129] H. Tsuge, T. Mitsuzuka, A. Kamijo, and K. Matsuda, Mat. Res. Soc. Symp. Proc. (1998), to be published.

[130] M. A. M. Gijs and G. E. W. Bauer, Adv. Phys. **46**, 285 (1997).

[131] H. Boeve, R. J. M. van de Veerdonk, J. De Boeck, J. S. Moodera, and G. Borghs, J. Appl. Phys. **83**, 6700 (1998).

[132] S. A. Rishton, Y. Lu, R. A. Altman, A. C. Marley, X. P. Bian, C. Jahnes, R. Viswanathan, G. Xiao, W. J. Gallagher, and S. S. P. Parkin, Microelec. Eng. **35**, 249 (1997).

[133] F. Bardou, Europhys. Lett. **39**, 239 (1997).

[134] H. Watanabe, K. Fujita, and M. Ichikawa, Appl. Phys. Lett. **72**, 1987 (1998).

[135] V. Da Costa, F. Bardou, C. Béal, Y. Henry, J. P. Bucher, and K. Ounadjela, J. Appl. Phys. **83**, 6703 (1998).

[136] W. Oepts, H. J. Verhagen, W. J. M. de Jonge, and R. Coehoorn, Appl. Phys. Lett. **73**, 2363 (1998).

[137] W. Oepts, H. J. Verhagen, D. B. Mooij, V. Zieren, R. Coehoorn, and W. J. M. de Jonge, J. Magn. Magn. Mater. (1998), to be published.

[138] E. R. Nowak, M. B. Weissman, and S. S. P. Parkin, Appl. Phys. Lett. (1998), to be published.

[139] E. R. Nowak, R. D. Merithew, M. B. Weissman, I. Bloom, and S. S. P. Parkin, J. Appl. Phys. **84**, 6195 (1998).

[140] D. J. Smith, M. R. McCartney, C. L. Platt, and A. E. Berkowitz, J. Appl. Phys. **83**, 5154 (1998).

[141] R. A. de Groot, F. M. Müller, P. G. van Engen, and K. H. A. Buschow, Phys. Rev. Lett. **50**, 2024 (1983).

[142] R. A. de Groot, Physica B **172**, 45 (1991).

[143] V. Y. Irkhin and M. I. Katsnel'son, Phys. Uspekhi **37**, 659 (1994).

[144] C. T. Tanaka, J. Nowak, and J. S. Moodera, J. Appl. Phys. **81**, 5515 (1997).

[145] C. T. Tanaka, J. Nowak, and J. S. Moodera, unpublished results.

[146] J. H. Park, E. Vescovo, H. J. Kim, C. Kwon, R. Ramesh, and T. Venkatesan, Nature **392**, 794 (1998).

[147] C. Zener, Phys. Rev. B **82**, 403 (1951).

[148] J. Z. Sun, Phil. Trans. Roy. Soc. London A **356**, 1693 (1998).

[149] X. W. Li, A. Gupta, G. Xiao, W. Qian, and V. P. Dravid, Appl. Phys. Lett. **73**, 3282 (1998).

[150] Y. Ando, J. Murai, T. Miyashita, and T. Miyazaki, Thin Solid Films **331**, 158 (1998).

Summary

The work described in this thesis concerns experiments and modeling of spin-polarized electron transport processes in magnetic layered structures, and has been divided in two separate parts, each with a distinctly different scope. The first part focusses on the characterization and understanding of electronic noise, in particular magnetism induced $1/f$ noise. For this study use is made of two types of magnetic model systems, both designed for magnetic sensing applications. In the second part, on the other hand, focus is on one system, called a tunnel junction. We present results of investigations using various methods of their electrical transport properties.

The electronic noise measurements discussed in the first part of this thesis have been performed in the frequency range between 1 Hz and 100 kHz. The noise has been measured as a function of an applied magnetic field in the plane of two types of microfabricated thin film magnetic structures of which the properties are optimized for application in magnetic tape recording. The geometry of these devices contains an active area in the form of a 10-μm-wide stripe of varying length. The first type of devices consists of a single magnetic film, and displays anisotropic magnetoresistance, i.e., the resistance depends on the relative orientation of the magnetic moment and the sense current. The more complicated built-up of the second type of devices is called a spin-valve, in which two magnetic layers are separated by a nonmagnetic one. These devices display the giant magnetoresistance effect, i.e., the resistance depends on the relative orientation of both magnetic moments.

In both device types the magnetic moment of the sense layer is a single magnetic domain and rotates coherently under the application of a magnetic field perpendicular to the stripe direction. During this rotation, electronic noise measurements were performed at fixed magnetic field and fixed sense current. The frequency resolved noise spectrum is obtained as the Fourier transform of the output-voltage versus time trace and consists of two independent contributions. A well understood magnetic field independent Johnson noise contribution was found for the highest frequencies. For the lowest frequencies, a $1/f$ noise contribution was obtained, with a nonmagnetic background, comparable in size to that for other metals, and a magnetic field dependent excess contribution. Using a simple Stoner–Wohlfart model to describe the free energy of the magnetic sense layer, it was found that the excess magnetic field dependent contribution to the $1/f$ noise can be well modeled as resulting from thermal fluctuations of the magnetization direction of the sense layer. These magnetic fluctuations translate to electric fluctuations as a result of the magnetoresistance effect.

The tunnel junctions studied in second part of this thesis consist of two metallic electrodes separated by a thin (order 1 nm) insulating barrier. An electron can surpass the barrier in a tunneling event. The rate of tunneling events depends (in a simplified picture) on the product of the densities of electron states at the Fermi level of the two electrodes. For ferromagnets, the densities of majority and minority spin electron states are unequal, which results in the junction magnetoresistance, or tunnel magnetoresistance effect. This effect depends on the relative orientation of the magnetic moments in the same way as the giant magnetoresistance effect, but with a much larger amplitude for applicable device geometries. The obtainable amplitude can be fairly well predicted from the product of the tunneling electron spin-polarizations. This parameter has been measured for a range of magnetic $3d$ transition metal alloys containing Ni, Fe, and Co, using the peaked structure of the Zeeman spin-split density of states of a superconducting Al film as a spin-sensitive detector. The presently obtained polarization values are higher than previously reported results due to the cleaner fabrication process. The polarization depends slightly on the alloy composition, with a maximum of ~50% for the alloys $Ni_{50}Fe_{50}$ and $Co_{50}Fe_{50}$. The Ni rich alloys showed a lower polarization value as compared to MBE grown samples, indicating a higher sensitivity of Ni for contamination or oxidation. Junctions containing Al_2O_3, AlN, and MgO barriers did not reveal a significant dependence of the polarization on the barrier composition.

Although the junction magnetoresistance effect has been discovered as early as 1975, difficulties of technological nature for a long time resulted in small, and difficult to reproduce effects, which were only observed at temperatures well below room temperature. Only recently the reliable two-step fabrication technology called glow discharge oxidation has been introduced, which is also used in this thesis. The magnetic tunnel junctions fabricated using this technology show large magnetoresistive effects also at room temperature. The process is performed in ultra high vacuum, where first a thin metallic Al layer is deposited on top of the bottom electrode, which is subsequently transformed in an insulating Al_2O_3 layer using reactive oxygen formed in a glow discharge between two metallic electrodes at a high differential voltage. The amount of formed oxide depends, among others, on the duration of this second step. For prolonged oxidation, an oxide forms at the bottom interface which deteriorates the magnetoresistive properties at room temperature. In retrospect, this explains the poor results obtained for magnetic tunnel junctions based on barriers of the native oxides of Ni, Co, and Gd in the period between the initial discovery in 1975 and the first sizeable room temperature results reported for Al_2O_3 barriers in 1995.

In general, the junction magnetoresistance decreases as a function of the applied bias voltage and at elevated temperatures. The decrease is faster than can be predicted from elastic tunneling models. Characterization of the tunnel junctions using current-voltage traces, inelastic electron tunneling spectroscopy, and the temperature dependence of the junction magnetoresistance showed that spin-wave excitations in the electrodes and/or during the tunneling process contribute significantly to the additional decrease of the magnetoresistance. A final, intriguing result is that when a nonmagnetic Au layer is added between the bottom ferromagnet and the barrier, the magnetoresistance changes sign, accompanied with a very asymmetric bias voltage dependence. This is attributed to the occurence of quantum well resonances in the interface layer.

List of publications

- *Perpendicular Giant Magnetoresistance of Microstructured Pillars in Magnetic Multilayers,*
  M. A. M. Gijs, S. K. J. Lenczowski, J. B. Giesbers, R. J. M. van de Veerdonk, M. T. Johnson, and J. B. F. aan de Stegge,
  Phys. Scripta **T55**, 189 (1994).

- *Current Distribution Effects in Microstructures for Perpendicular Magnetoresistance Experiments,*
  S. K. J. Lenczowski, R. J. M. van de Veerdonk, M. A. M. Gijs, J. B. Giesbers, and H. H. J. M. Janssen,
  J. Appl. Phys. **75**, 5154 (1994).

- *Perpendicular Giant Magnetoresistance of Microstructures in Fe/Cr and Co/Cu Multilayers,*
  M. A. M. Gijs, J. B. Giesbers, M. T. Johnson, J. B. F. aan de Stegge, S. K. J. Lenczowski, R. J. M. van de Veerdonk, and W. J. M. de Jonge,
  J. Appl. Phys. **75**, 6709 (1994).

- *Interpretation of the Giant Magnetoresistance Effect in Co/Cu(100) Multilayers with the Quantum Model of Giant Magnetoresistance,*
  S. K. J. Lenczowski, M. A. M. Gijs, J. B. Giesbers, R. J. M. van de Veerdonk, and W. J. M. de Jonge,
  Phys. Rev. B **50**, 9982 (1994).

- *Temperature Dependence of the Spin-dependent Scattering in Co/Cu Multilayers Determined from Perpendicular-Giant-Magnetoresistance Experiments,*
  M. A. M. Gijs, S. K. J. Lenczowski, R. J. M. van de Veerdonk, J. B. Giesbers, M. T. Johnson, and J. B. F. aan de Stegge,
  Phys. Rev. B **50**, 16733 (1994).

- *Perpendicular Giant Magnetoresistance of Co/Cu Multilayers Deposited under an Angle on Grooved Substrates,*
  M. A. M. Gijs, M. T. Johnson, A. Reinders, P. E. Huisman, R. J. M. van de Veerdonk, S. K. J. Lenczowski, and R. M. J. van Gansewinkel,
  Appl. Phys. Lett. **66**, 1839 (1995).

- *Perpendicular Giant Magnetoresistance of Microstructured Pillars in Fe/Cr and Co/Cu Magnetic Multilayers,*
  M. A. M. Gijs, S. K. J. Lenczowski, J. B. Giesbers, R. J. M. van de Veerdonk, M. T. Johnson, and J. B. F. aan de Stegge,
  Mat. Sci. Eng. B **31**, 85 (1995).

- *Determination of Spin-dependent Scattering Parameters of NiFe/Cu and Co/Cu Multilayers,*
  S. K. J. Lenczowski, M. A. M. Gijs, R. J. M. van de Veerdonk, J. B. Giesbers, and W. J. M. de Jonge,
  Mat. Res. Soc. Symp. Proc. **384**, 341 (1995).

- *Pependicular Giant Magnetoresistance Using Microlithography and Substrate Patterning Techniques,*
  M. A. M. Gijs, S. K. J. Lenczowski, J. B. Giesbers, R. J. M. van de Veerdonk, M. T. Johnson, R. M. Jongblut, A. Reinders, and R. M. J. van Gansewinkel,
  J. Magn. Magn. Mat. **151**, 333 (1995).

- *Study of the Verwey Transition of Fe_3O_4 Films and Fe_3O_4 / MgO Multilayers Grown by MBE,*
  R. J. M. van de Veerdonk, M. A. M. Gijs, P. A. A. van der Heijden, R. M. Wolf, and W. J. M. de Jonge,
  Mat. Res. Soc. Symp. Proc. **401**, 455 (1996).

- *Magnetite $Fe_{3-\delta}O_4$: a Stoichiometry and Structure Analysis of MBE Grown Thin Films Using NO_2 as the Oxidising Source,*
  F. C. Voogt, T. Hibma, P. J. M. Smulders, L. Niesen, T. Fujii, P. A. A. van der Heijden, R. J. M. van de Veerdonk, and P. J. van der Zaag,
  J. Phys. IV France **7**, C1-601 (1997).

- *A Study of the Magneto-optical Kerr Spectra of Bulk and Ultrathin Fe_3O_4,*
  P. J. van der Zaag, W. F. J. Fontijn, V. A. M. Brabers, R. J. M. van de Veerdonk, P. A. A. van der Heijden, P. Gaspard, and R. M. Wolf,
  J. Appl. Phys. **79**, 5936 (1996).

- *Current Distribution Effects in Magnetoresistive Tunnel Junctions,*
  R. J. M. van de Veerdonk, J. Nowak, R. Meservey, J. S. Moodera, and W. J. M. de Jonge,
  Appl. Phys. Lett. **71**, 2839 (1997).

- *1/f Noise in Anisotropic and Giant Magnetoresistive Elements,*
  R. J. M. van de Veerdonk, P. J. L. Beliën, K. M. Schep, J. C. S. Kools, M. C. de Nooijer, M. A. M. Gijs, R. Coehoorn, and W. J. M. de Jonge,
  J. Appl. Phys. **82**, 6152 (1997).

- *Interface Magnetism and Spin Wave Scattering in Ferromagnet-Insulator-Ferromagnet Tunnel Junctions,*
  J. S. Moodera, J. Nowak, and R. J. M. van de Veerdonk,
  Phys. Rev. Lett. **80**, 2941 (1998).

- *Area Scaling of Planar Ferromagnetic Tunnel Junctions: From Shadow Evaporation to Lithograhic Microfabrication,*
  H. Boeve, R. J. M. van de Veerdonk, B. Dutta, J. de Boeck, J. S. Moodera, and
  G. Borghs,
  J. Appl. Phys. **83**, 6700 (1998).

- *Characterization of Magnetic Tunnel Junctions Using IETS,*
  R. J. M. van de Veerdonk, J. S. Moodera, and W. J. M. de Jonge,
  J. Magn. Magn. Mat. (to be published).

- *Influence of Oxidation Time on the Properties of Magnetic Tunnel Junctions,*
  R. J. M. van de Veerdonk, J. S. Moodera, H. J. M. Swagten, N. C. W. Kuijpers,
  and W. J. M. de Jonge, (in preparation).

- *Tunneling Electron Spin-Polarization Measured by Tunneling,*
  R. J. M. van de Veerdonk, J. S. Moodera, and W. J. M. de Jonge, (in preparation).

- *Observation of Quantum Well States in Spin Dependent Tunnel Structures,*
  J. S. Moodera, J. Nowak, L. R. Kinder, P. M. Tedrow, R. J. M. van de Veerdonk,
  A. A. Smits, M. van Kampen, H. J. M. Swagten, and W. J. M. de Jonge, (in
  preparation).

- *MOKE Measurements on Tunnel Junctions with Variable Oxidation Time,*
  A. A. Smits, C. J. P. M. van Nuenen, R. J. M. van de Veerdonk, J. S. Moodera,
  H. J. M. Swagten, and W. J. M. de Jonge, (in preparation)

- *The Spin Polarization of Fe_xNi_{1-x},*
  R. J. Soulen, Jr., B. Nadgorny, M. S. Osofsky, I. Mazin, T. Ambrose, S. F. Cheng,
  S. Qadri, J. Byers, G. Laprade, R. J. M. van de Veerdonk, and J. S. Moodera, (in
  preparation)

Samenvatting

Dit proefschrift beschrijft experimenten aan en modellering van spin gepolariseerde elektron transport verschijnselen in gelaagde magnetische structuren en bestaat uit twee gedeelten met eigen karakter. Deel één concentreert zich op het karakteriseren en modelleren van elektrische $1/f$ ruis van magnetische oorsprong. Hiervoor zijn twee soorten magnetische model structuren gebruikt, beiden ontworpen als magneetveld-detector. Deel twee concentreert zich op één systeem, een tunnel junctie, waarvan de elektrische transport eigenschappen werden onderzocht met verschillende methoden.

De elektrische ruis experimenten die in het eerste deel van dit proefschrift worden behandeld, zijn uitgevoerd in het frequentiegebied tussen 1 Hz en 100 kHz. De ruis is bepaald als functie van een aangelegd magneetveld in het vlak van twee soorten microgefabriceerde magnetische dunne film structuren, die zijn geoptimaliseerd voor magnetische bandopname toepassingen. Het ontwerp bestaat uit een 10 μm breed stripvormig actief gedeelte van gevarieerde lengte. De eerste soort structuren bestaat uit een enkele magnetische laag en vertoont het anisotrope magnetoweerstands effect, d.w.z. dat de weerstand afhangt van de relatieve oriëntatie van het magnetische moment en de meetstroom. De complexere opbouw van de tweede soort structuren wordt een spinklep genoemd en bestaat uit twee magnetische lagen die gescheiden worden door een dunne (orde 2 nm) niet-magnetische laag. Deze structuren vertonen het reuzen magnetoweerstands effect, d.w.z. dat de weerstand afhangt van de relatieve oriëntatie van beide magnetische momenten.

De gevoelige laag in beide structuren bestaat uit een enkel magnetisch domein, dat coherent roteerd in een magneetveld in de richting loodrecht op de strip. Ruismetingen zijn tijdens deze rotatie verricht met een constant magneetveld en met een constante meetstroom. Een frequentie opgelost ruisspectrum wordt verkregen door Fourier transformatie van de wisselspanning tegen tijd meeting. Twee onafhankelijke bijdragen worden onderscheiden. Een goed begrepen magneetveld onafhankelijke Johnson ruisbijdrage wordt gevonden voor de hoogste frequenties. Voor lagere frequenties wordt een $1/f$ ruisbijdrage gevonden met een niet-magnetische component van vergelijkbare grootte als in andere metalen, en extra magneetveld afhankelijke component. Met een eenvoudig Stoner–Wohlfart model kan de vrije energie van de magneetveld gevoelige laag worden beschreven. Binnen dit model blijken de thermische richtingsfluctuaties van het gevoelige magnetische moment de extra $1/f$ ruis bijdrage goed te kunnen modelleren, als bedacht wordt dat magnetische fluctuaties zich vertalen in elektrische fluctuaties door het magnetoweerstands effect.

Deel twee van dit proefschrift beschrijft tunnel juncties, bestaande uit twee metallische elektroden, gescheiden door een dunne (orde 1 nm) isolerende barrière. Een elektron kan de barrière doorbreken tijdens een tunnel gebeurtenis. De frequentie daarvan hangt (binnen een versimpeld model) af van het product van de elektronen toestandsdichtheden aan het Fermi niveau van beide elektroden. Voor ferromagneten verschilt deze waarde voor meerderheids- en minderheids-spin elektronen, waardoor het junctie magnetoweerstands, of tunnel magnetoweerstands effect ontstaat. Het magnetische gedrag is gelijk aan dat van het reuzen magnetoweerstands effect, maar het effect is voor toepasbare ontwerpen groter. De bereikbare grootte wordt redelijk voorspeld door het produkt van de spin-polarisaties van de tunnelende elektronen. Deze grootheid is bepaald voor een reeks magnetische $3d$ transitie metaal legeringen bestaande uit Ni, Fe en Co. Hiertoe werd de Zeeman opgesplitste piek-structuur van de elektronen toestandsdichtheid van supergeleidend Al gebruikt als spin-gevoelige detector. De gevonden polarisatiewaarden zijn groter dan eerder gerapporteerd door de schonere preparatie en variëren licht met de samenstelling, met een maximum van $\sim$50% voor de legeringen $Ni_{50}Fe_{50}$ en $Co_{50}Fe_{50}$. Voor Ni-rijke legeringen is de polarizatie lager dan voor MBE gegroeide juncties, wat aangeeft dat Ni gevoelig is voor verontreinigingen of oxidatie. Juncties met Al_2O_3, AlN en MgO barrières vertonen geen significant verband tussen de polarisatie en de barrière samenstelling.

Hoewel het junctie magnetoweerstands effect al in 1975 is ontdekt, leidden technologische problemen nog lang tot kleine, moeilijk te reproduceren effecten, die bovendien alleen bij lage temperaturen werden bereikt. Pas in 1995 werd het reproduceerbare twee-staps fabricage proces geïntroduceerd, plasma oxidatie genaamd, dat ook voor dit proefschrift is gebruikt. De hiermee gemaakte magnetische tunnelstructuren vertonen grote magnetoweerstands effecten, ook bij omgevingstemperatuur. Het proces verloopt in ultra-hoog vacuüm door eerst een metallisch Al laag op een onderelektrode te groeien. Het Al wordt daarna omgezet in Al_2O_3 door reactief zuurstof, wat wordt aangemaakt in een plasma tussen twee metaalplaten met een groot onderling potentiaalverschil. De gevormde hoeveelheid oxide hangt onder meer af van de duur van de tweede processtap. Tijdens een verlengde oxidatiestap oxideert de onderste elektrode, wat de magnetoweerstands-eigenschappen bij omgevingstemperatuur verslechtert. Terugkijkend, verklaart dit mogelijk de mindere resultaten die werden bereikt in de periode tussen 1975 en de eerste substantiële resultaten bij omgevingstemperatuur met Al_2O_3 barrières in 1995. In die periode werden voornamelijk tunnel structuren gebruikt met barrières bestaande uit de natuurlijke oxides van Ni, Co en Gd.

De junctie magnetoweerstand neemt sterker af bij hogere aangelegde spanningen en bij verhoogde temperatuur dan voorspeld door elastische tunnel modellen. Bestudering van tunnel juncties door middel van stroom-spannings karakteristieken, niet-elastische tunnel-elektronen spectroscopie en de temperatuurs afhankelijke junctie magnetoweerstand laten zien dat spin-golf excitaties in de elektroden en/of tijdens een tunnel gebeurtenis substantieel bijdragen aan de extra verlaging van de magnetoweerstand. Als een laaste, verassend resultaat, kan een niet-magnetisch Au laagje dat is toegevoegd tussen de onderste ferromagneet en de barrière de magnetoweerstand van teken doen omkeren, vergezeld gaande van een erg asymmetrische spannings-afhankelijkheid. Dit is toegewezen aan het optreden van quantum resonanties in de Au laag.

Dankwoord/Acknowledgements

Ten slotte wil ik graag de mensen bedanken die het mogelijk hebben gemaakt dat dit proefschrift tot stand is gekomen. Onderzoek doe je niet alleen, maar samen met een groot aantal anderen. Aan de ene kant zorgt dat ervoor dat niet alles verloopt volgens mijn eigen plannen, maar aan de andere kant ontstaan er zo ook verfrissende inzichten waardoor het onderzoek wordt versneld of zich in nieuwe richtingen ontwikkelt.

Een belangrijke bijdrage hebben uiteraard de mensen gehad die financiëel, wetenschappelijk en organisatorisch hun nek hebben uitgestoken om mij de kans te geven om dit onderzoek te starten. Allereerst zijn dat Wim de Jonge van de Technische Universiteit Eindhoven als eerste promotor, Martin Gijs van Philips Research als dagelijkse begeleider, en Henk van Houten van Philips Research als groepsleider van de groep Exploratory Physics. Als gevolg van interne reorganisaties heeft later Reinder Coehoorn de positie van Martin Gijs overgenomen en werd het onderzoek overgeheveld naar de groep Magnetisme, onder leiding van Frans Greidanus. Later werd deze groep tot Storage Technologies hervormd, onder leiding van Wouter Leijbrandt. Ondanks alle reorganisaties, blijken de meeste wetenschappelijke doelen die we ons in het begin hebben gesteld te zijn gehaald, zij het niet op de manier zoals oorspronkelijk was bedacht.

Mijn werk begon binnen het project oxidische materialen, onder leiding van Ronald Wolf, later Jim Gains. Binnen dit project werd gewerkt aan de realisatie van de volledig oxidische tunnel junctie, gebaseerd op het veelbelovende materiaal magnetiet. Ronald Wolf, Jos aan de Stegge, Pascal Bloemen, Johan van Eemeren, en Jim Gains namen de groei van de films met behulp van de oxidische MBE voor hun rekening. Nuttig ook was de interactie met Paul van der Heijden, Lou-Fé Feiner, Jürgen Kohlhepp, Coen Swüste, Mark van Opstal, Gustav Strijkers, en Vic Brabers. Voor de microfabricage kon ik voor hulp en morele ondersteuning terecht bij Ben Giesbers. Veel metingen zijn uitgevoerd door de studenten Vincent Lammers en Koen van den Biggelaar, die hun stage onder mijn leiding hebben uitgevoerd. Als klankbord kon ik rekenen op de "koffieclub WB," waarin met name Martin Gijs, Staszek Lenczowski, Kees Schep en Christian Schönenberger prominent aanwezig waren. Helaas werd de oxidische MBE door de Philips directie gesloten vlak voordat dit onderzoek uitzicht kreeg op goede resultaten, waardoor er uiteindelijk niets in dit proefschrift is opgenomen.

Inmiddels was nieuwe onderzoek gestart onder leiding van Martin Gijs naar de ruis in metallische magnetische systemen. Door het vertrek van Philip Beliën en het wegvallen van de oxidische activiteiten ben ik aan dit onderzoek begonnen, waarbij ik een vliegende start maakte met een grote voorraad experimentele gegevens. Voor dit onder-

zoek werd de groei van de structuren verzorgd door Jacques Kools en Marie-Christine de Nooijer, die ook voor de microfabricage zorgde. De interpretatie van de ruisdata gebeurde wederom via de "koffieclub WB," waarbij nu ook de afstudeerders Jeroen van Est en Joost Briaire voor de nodige discussie zorgden. Voor het schrijven van het artikel was de inbreng van Reinder Coehoorn van onschatbare waarde.

The bulk of the results contained in this thesis is obtained in collaboration with the group of Jagadeesh Moodera at the Francis Bitter Magnet Laboratory of the Massachusetts Institute of Technology, Cambridge, U.S.A. My first contact with Jagadeesh Moodera was a result of my first conference attendence outside Europe, the MRS Fall Meeting in Boston, U.S.A., late 1995. Jagadeesh Moodera had just published his first paper on magnetic tunnel junctions and was considered an authority on tunneling. After this visit we remained in contact, which resulted in a successful collaboration to the benefit of all those involved. I have enjoyed the part-time hospitality of the Lab. and its researchers. Special thanks are for Janusz Nowak, the "super technician" and discussion partner, Ronnie Jansen, for many heated discussions, Chang-He Shang, whoms data fueled these discussions, and Jagadeesh Moodera, who learned me the details of the fabrication process and assisted with the measurements. Paul Tedrow and Robert Meservey are acknowledged for their interest in my work. Simon Foner was always good for a humorous story, and served as a critic during practise presentations. Many helping hands came from students for finding/getting/repairing things, or to do measurements. Special thanks are for the graduate students Clifford Tanaka and Michelle Cortes-Real, the master students Patrick LeClair, Lisa Kinder, and Barry Stevens, and the summer students, of which Lisa Gallagher, Keziah Robinson, and Shira Robinson deserve special credit. I made many friends in Boston, both in and outside the Lab.

Several external groups have characterized our samples with specialized techniques. Among these, I would like to thank Hans Boeve, Jo de Boeck, and coworkers of IMEC, Leuven, Belgium, for their microfabrication efforts, Chengtao Yu and Prof. Hartmut Zabel of the Ruhr-Universität Bochum, Germany, for XRD measurements, Amanda Petford-Long and Xavier Portier of Oxford University, UK, for their HR-TEM pictures, and Robert Soulen, Boris Nadgorny and coworkers of the Naval Research Laboratories, Washington, U.S.A. for Andreev reflection measurements.

Binnen het nieuwe en reeds succesvolle hybride recording project bij Philips Research, onder leiding van Reinder Coehoorn, wordt het onderzoek aan magnetische tunnel juncties voortgezet. De leden van dit project hebben voor mij als klankbord gediend, speciaal collega promovendus Wouter Oepts. Aan de universiteit werd ik in mijn onderzoek aan tunnel juncties geholpen door de afstudeerders Niels Kuipers, Cas van Nuenen en Maarten van Kampen, alsmede door de collega promovendi Bart Smits, Gustav Strijkers en Patrick LeClair. Henk Swagten heeft de nodige teksten kritisch becommentarieerd.

Rest mij nog om de leescommissie bestaande uit Wim de Jonge, Reinder Coehoorn, Martin Gijs en Hidde Brongersma te bedanken voor hun kritische opmerkingen. Kees Schep wil ik speciaal bedanken als kamergenoot en discussie partner tijdens het grootste deel van ons beider promotie. Als laatste wil ik graag mijn ouders en broer bedanken voor de rustige thuishaven die zij vormden tijdens mijn promotie. Zonder al deze mensen, en al die anderen die ik ben vergeten, zou dit proefschrift niet zijn geschreven.

Curriculum vitae

René Johannes Marinus van de Veerdonk

Januari 6, 1971   Born in Eindhoven, The Netherlands

1983–1989   Atheneum B at "Hertog Jan College," Valkenswaard

1989–1993   Applied Physics at Eindhoven University of Technology
Graduate research in the group Physics of Nanostructures of prof.dr.ir. W. J. M. de Jonge
Research carried out at the Philips Research Laboratories, Eindhoven.
Perpendicular and In-Plane Magnetoresistance Measurements on Co/Cu (100) Multilayers

1994–1998   "Assistent in Opleiding" at Eindhoven University of Technology, Department of Applied Physics, in the group Physics of Nanostructures of prof.dr.ir. W. J. M. de Jonge
Ph.D. research carried out at the Philips Research Laboratories, Eindhoven, and at the Francis Bitter Magnet Laboratory, Massachusetts Institute of Technology, Cambridge, Massachusetts, U.S.A.
Spin Polarized Transport in Magnetic Layered Structures; 1/f noise and tunnel junctions

STELLINGEN

behorende bij het proefschrift

Spin polarized transport in magnetic layered structures: $1/f$ noise and tunnel junctions

door René J. M. van de Veerdonk

1. De door magnetisme geïnduceerde elektrische $1/f$ ruis bijdrage in anisotrope en reuzen-magnetoweerstandselementen, kan goed worden beschreven door thermische fluctuaties van de richting van het magnetische moment van de magneetveld gevoelige laag.

   Dit proefschrift, hoofdstuk 2

2. Voor het beschrijven van de verlaging van de tunnel-magnetoweerstand van magnetische tunnelstructuren, die optreedt door het verhogen van de temperatuur of het aanleggen van een elektrische spanning, is het belangrijk om de bijdrage van spin-golven in rekening te brengen.

   Dit proefschrift, hoofdstuk 6

3. Een alleen op elastische tunnelprocessen gebaseerd analyse van stroom–spannings karakteristieken van magnetische tunnelstructuren, gemeten bij omgevingstemperatuur, kan een misleidend beeld geven.

   Dit proefschrift, hoofdstuk 8

4. De snelle afname van de tunnel-magnetoweerstand voor oplopende temperaturen, genormaliseerd op de Curie temperatuur van de elektroden, voor oxidische in vergelijking met metallische elektrode materialen, wordt deels veroorzaakt door het verschil in de vrije weglengte van de geleidingselektronen.

   Zie bijvoorbeeld J. Z. Sun, Phil. Trans. Roy. Soc. London A **356**, 1693 (1998).

5. Omdat de tunnel-magnetoweerstand van een magnetische tunnelstructuur volledig wordt bepaald door de grenslagen met de barrière, kan het magnetische gedrag onafhankelijk van het magneto-elektrische gedrag worden geoptimaliseerd. Dit kan een groot voordeel betekenen in vergelijking met metallische magnetoweerstandsstructuren.

6. De door Prados *et al.** gevonden verhoogde magneto-weerstand in een gekruiste meetgeometrie, kan worden gevonden voor alle magnetische materialen die het anisotrope magnetoweerstandseffect vertonen. De magnetoweerstand kan in een ideale geometrie een arbitrair grote waarde aannemen, maar dat leidt als zodanig niet tot een verbeterde toepasbaarheid.

*C. Prados, D. Garcia, F. Lesmes, J. J. Freijo en A. Hernando, Appl. Phys. Lett. **67**, 718 (1995).

7. De geleiding van een ballistisch puntcontact neemt als functie van contactoppervlak periodiek toe in gehele stappen van de minimale geleidingseenheid e^2/h.* Voor magnetische metalen worden twee verschillende perioden verwacht, één voor ieder spin-kanaal.

*Zie bijvoorbeeld C. W. J. Beenakker en H. van Houten, Solid State Phys. **44** 1, (1991).

8. De tijd die een gebruiker besteed aan het onderhouden en het uitproberen van computer programma's is evenredig met zijn/haar vermeende deskundigheid.

9. Door ontsluitings- en verbindingswegen in een eerder stadium aan te leggen dan nieuwe woonwijken, wordt vertraging voorkomen en het woongenot verhoogd.

10. Het afschilderen van badminton als campingsport doet afbreuk aan de snelheid van het spel en de fysieke eisen die aan een topspeler worden gesteld.

http://mid1.external.hp.com:80/stanb/badfaq.html